NanoBioPhotonic Platforms for Nanotherapy and Nano-Imaging: Polymer-Encapsulated Metal Clusters, Plasmonic Nanosnakes, and Targeting Enhanced Nanosystems

by

Alan McLean

A dissertation submitted in partial fulfillment
of the requirements for the degree of
Doctor of Philosophy
(Chemistry)
in The University of Michigan
2020

Doctoral Committee:

Professor Raoul Kopelman
Professor Zhan Chen
Professor Aaron Frank
Professor Gary Luker

Alan Michael McLean

ammclean@umich.edu

ORCID ID: 0000-0002-7226-7076

DEDICATION

This thesis is dedicated to *mu'elim*, my dear teacher and friend.

كەل دېسەن كەلمەيدۇ ، كەلمە دېسەن كېلىدۇ

ACKNOWLEDGEMENTS

First and foremost, I would like to thank my wife, Yu Yan, and my PhD mentor, Dr. Raoul Kopelman. I met Yu Yan just before beginning my PhD studies, and she has been my pillar of support throughout my entire PhD. Similarly, Dr. Kopelman accepted me into the Kopelman laboratory with open arms. Dr. Kopelman has defended my ideas, allowed me to pursue the research that I find most interesting, and provided lots of opportunities for me to grow as a scientist, both through research and teaching. It has been an absolute privilege to work in the Kopelman laboratory, and I am grateful for this experience every day. I also would like to thank Drs. Wei Qian, Panos Argyrakis, Rongchao Jin, Scott Swanson, Guan (Gary) Xu, Yannis Paulus, Wei Zhang, Damon Hoff, Kai Sun, and Sasha Meshinchi. Dr. Qian has been my mentor since the first day that I joined the Kopelman laboratory, and I feel very proud that we could work on that Au nanochain project together. Working with Dr. Argyrakis has also been wonderful – I am especially excited about our collaboration using Monte Carlo simulations to study nanochains, and I am even more excited for the next chapter of this research. Dr. Rongchao Jin supported my first project in synthesizing $Au_{25}Capt_{18}$ that I utilized for two-photon photodynamic therapy; I am very thankful that Dr. Jin's support made the Au_{25} project possible. Working with Dr. Swanson to characterize new materials for NMR and MRI applications has been thrilling, and I always look forward to listening to Dr. Swanson's NMR wealth of knowledge. Dr. Guan Xu has been very supportive of my applied research and was instrumental in helping me with technical *in vivo* experiments. Similarly, Drs. Yannis Paulus and Wei Zhang have been wonderful collaborators for the choroidal neovascular project. I am very grateful both Dr. Yannis Paulus and Dr. Wei Zhang supported my efforts despite the challenges we encountered; I have learned a great deal about translating

benchtop work to *in vivo* experiments through them. Dr. Damon Hoff was my go-to optics resource, both as manager of the SMART center and for help inside the Kopelman Lab. A very valuable lesson I learned from Dr. Hoff was how to align a 'two-photon' beam through a microscope – this greatly improved the quality of my two-photon microscopy experiments. Dr. Kai Sun, at the University of Michigan Center for Materials Characterization, helped me run high-resolution transmission electron microscopy (TEM) experiments that were imperative for publication. Similarly, Sasha Meshinchi taught me how to perform lower resolution TEM and was an open resource whenever I had questions. I also need to thank the Master's and undergraduate students who I have worked with in research (from beginning to end): Natalie Potter, Rong Duan, Jalal Haidar, Ferris Bayasi, Ruofei Wang, Siying Yu, Rahil Ukani, Tarun Gogineni, Renhui Zhou, Joseph Isaac, Alexander Cooke, Ryan McLean, Ying Huo, Jonathan Scher, and Anna Rapp. It has been an honor to work with and mentor such great students, and I am very proud of the accomplishments from them all. In addition, I am very thankful towards my PhD colleagues, Binyamin Jacobovitz, Jeffrey Folz, Thomas Hopkins, and Chang Lee. I am especially grateful that our relationship was so strong and that I have many great memories and lifelong friendships with them. I would like to thank the University of Michigan Rackham Graduate School for support and sponsorship – especially for holding events like the Karle Symposium which allowed me to present my research and my PhD committee who has evaluated my research, Drs. Raoul Kopelman, Zhan Chen, Aaron Frank, and Gary Luker. Furthermore, I am thankful for all staff I have worked with in teaching: Dr. Raoul Kopelman, Dr. Amy Gottfried, Dr. Mou-Chi Cheng, Dr. Guenther Kellner, Dr. Joseph Ward, and Dr. John Wolfe. I would also like to thank former mentors who were instrumental for me to reach the stairs of the PhD degree: Drs. Theodore Goodson, Oleg Varnavski, Travis Clark, Sunghei Yau, Marc Hershenson, Chong-Yu Ruan, Faran Zhou, Stephen Lipsius and former colleague Brian Pinsky. I would also like to thank my family Yu Yan, Brian McLean, Geri McLean, Shaoming Yan, Hong Guo, Evan McLean, Ryan McLean, and Zeanie Yoon, and friends Dr. Cody Aldaz, Shiba Sundar, Timothy 'Cousin' Orzechowski, Prof. Kicengge,

Ying Ding, and Kannappan Sampath. Lastly, I thank the National Institutes of Health (R01CA186769) and The University of Michigan (M-Cubed Grant Program, Rackham Graduate School), who funded the research during my PhD.

TABLE OF CONTENTS

LIST OF FIGURES

ABSTRACT

Nanoparticle-based technology has reached a threshold where biocompatible NPs with controllable size, morphologies, and functionality are becoming widely fabricated and utilized. This dissertation evaluates new nanobiophotonic platforms for nanotherapy and nanoimaging applications, including polyacrylamide (PAAm)-encapsulated metal clusters, plasmonic nanosnakes, and RGD-targeted fluorescent 8-arm-peg NPs.

We first examine biocompatible polyacrylamide (PAAm)-encapsulated $Au_{25}Capt_{18}$ metal nanoclusters (NCs) for applications in two-photon photodynamic therapy. We demonstrate highly efficacious *in vitro* two-photon PDT for these PAAm-$Au_{25}Capt_{18}$ NPs, exhibiting a tremendous enhancement in 2p-PDT-mediated cell death over one-photon PDT-mediated cell death. Furthermore, we show that as a new two-photon photodynamic agent, the $Au_{25}Capt_{18}$cluster, (a) has a two-photon cross-section 8x larger when compared to 5,10,15,20-Tetrakis(1-methyl-4-pyridinio)porphyrin tetra(p-toluenesulfonate) (TMPYP), the currently most used two-photon photosensitizer, (b) has modest reactive oxygen species (ROS) production (1%) under two-photon excitation, with the potential for this efficiency to be further improved, and (c) when embedded in hydrogel NPs it maintains its unique optical properties while achieving 100% higher tumor uptake and biocompatibility.

Next, we fabricate and characterize highly linear plasmonic nanochains of gold nanospheres, which we call “nanosnakes”. These nanosnakes are self-assembled from bare Au nanosphere monomers with virgin surfaces, produced in DI water by laser ablation (a green, chemical-free synthesis). The nanosnakes have several highly desirable properties for biological imaging, including two plasmonic modes, one fixed mode at 525 nm (monomer mode) and a second highly tunable mode. The secondary

tunable mode ranges from 590 nm to 640 nm, with tunability precision within 1-2 nm. Such tunability towards the infrared is a highly desirable property in plasmonic imaging, due to these photons' deeper tissue penetration as well as due to their much reduced background cell fluorescence. We also show that the nanosnakes possess scattering cross-sections up to 40x higher than the Au nanosphere monomers (approximately 3x higher per chain monomer nanosphere), thus making them better contrast agents for imaging applications. Lastly, we demonstrate that the nanosnakes can be easily conjugated with active targeting moieties, for applications such as targeted cancer and heart disease phototherapy, using the RGD peptide as a model system; furthermore, we show that they are also non-toxic to cells, even at very high concentrations (> 0.25 mg/mL, OD 5.0). Overall, the nanosnakes represent a promising new imaging modality for dark-field, SERS, and high resolution microscopy, and have a high potential for *in vivo* theranostic applications.

Lastly, we evaluate fluorescent 8-arm-peg NPs for their RGD-assisted targeting to the age-related macular degeneration (AMD) neovasculature. *In vitro* experiments reveal a strong, measurable difference between non-targeted and RGD targeted NPs, with the RGD targeted NPs showing nearly a 100 % increase in cellular uptake at the highest incubated NP concentration (3 mg/mL). *In vivo* experiments at high incubated PEG-RGD concentrations (20 mg/mL injections) show approximately 15-20% enhancement in targeting signal, when compared to non-RGD controls. Overall, we show that 8-arm PEG NPs are a new, readily conjugatable and targetable nanosystem for future optimized AMD diagnosis and therapy, with potential benefits for *in vivo* theranostic enhancement.

Overall, this dissertation evaluates polyacrylamide (PAAm)-encapsulated metal clusters, plasmonic nanosnakes, and RGD-targeted fluorescent 8-arm-peg NPs. These nanobiophotonic platforms are biocompatible, deliverable *in vitro* and/or *in vivo*, and exhibit specialized utility, with clear advantages as a new nanomaterial in cancer therapy, plasmonic imaging, and/or disease targeting for applied nanotherapy and nanoimaging.

Chapter 1: Introduction

The focus of this dissertation is on applied nanotechnology for biomedical applications. The field of nanotechnology is one of the most active fields of modern research and is rapidly transforming the fields of biology and medicine. To exemplify the growth of "nanomedicine", the number of FDA approved nanodevices has been growing exponentially since 2000, with many new drugs in development.[1] This introduction will introduce the core concepts from each chapter of the thesis. In section 1.1, nanoparticles are defined and their basic properties are discussed in relation to applied biomedicine. In section 1.2, nanoparticle-based photodynamic therapy (PDT), a medical treatment involving targeted light therapy, is introduced. In section 1.3, an introduction to nanoparticle-based dark-field imaging is presented, with core concepts of theoretical modeling also outlined. In section 1.4, nanoparticle-based active targeting is discussed, and applications towards macular degeneration (MD)-targeting are introduced. Lastly, section 1.5 presents an outline for the remainder of the dissertation.

1.1 An Introduction to Nanoparticles

1.1.1 What is a Nanoparticle?

The standard definition of a nanomaterial is any material on the scale of 1 – 1000 nm in at least one dimension.[2] Nanomaterials are ubiquitous throughout nature; for example, viruses are largely on the scale of nanometers.[3] Furthermore, as an important historical example, interplanetary dust has naturally occurring morphologies on the nanometer scale, an example which is provided in Figure 1.1; this lead to the development of computational methods to study nanoparticle physics (i.e. Mie Theory and Discrete Dipole Scattering Theory, utilized extensively in Chapter 3).[4] Originating with mankind, nanomaterials have been discovered in Mesopotamian pottery dating back to 9 CE.[5] Furthermore, nanoproducts of gold

(Au) and silver (Ag) have been used in stained glass for centuries, which gives the glass their characteristic hues, as shown in Figure 1.1.

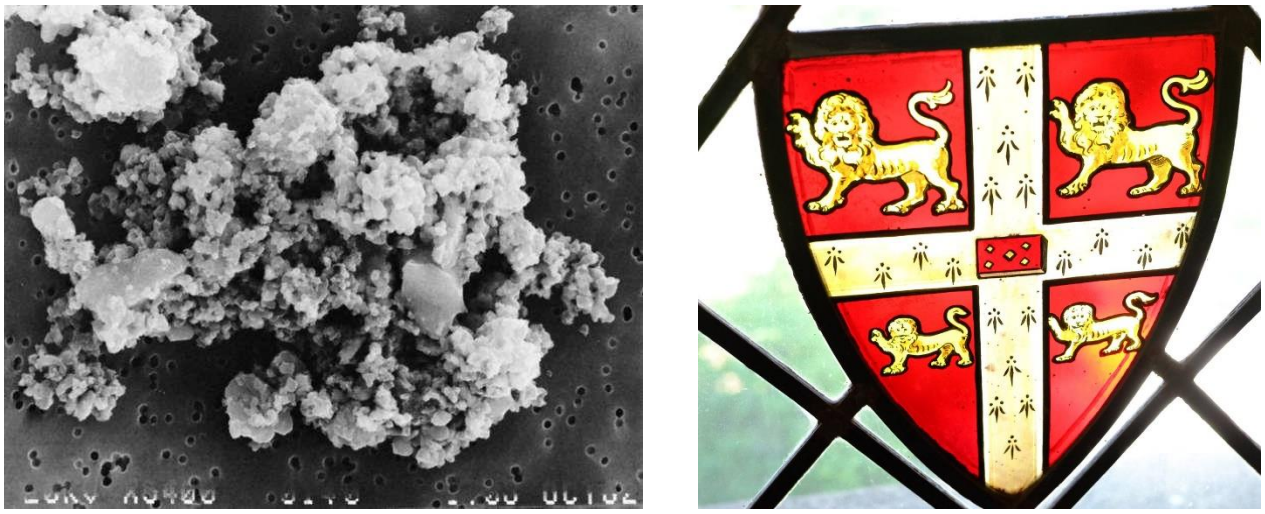

Figure 1.1 (Left) Interplanetary dust particle, thought to originate from a comet. The particle measures 18 µm in its longest axis, with nano-sized sub-morphologies. (Right) Stained glass window in the University Library at Cornell. Starting from around the 10th century, silver and gold nanoparticles were used to give stained glass yellow and red hue, albeit their nature as nanomaterials was unknown until the 20th century.

However, until half a century ago, the field of nanoscience remained practically unstudied.[6] The systematic study of nanoparticles began in the 1970s-1980s, with the coinage of the term nanotechnology in 1974.[6] To achieve some of the first lab-made nanoparticles, the fabrication of nanoparticles had often consisted of using a mortar and pestle to grind materials down into a sub-µm grain.[7] However, in modern days, the fabrication, variability, and even the definition of a nanoparticle has evolved.

1.1.2 Nanoparticle Size and Enhanced Permeability and Retention (EPR)

For biological applications in the modern day, nanoparticles under 250 nm are generally utilized, and the size of the nanoparticle is one of the major parameters of biological importance. For example, larger nanoparticles (250+ nm) are typically too large to be efficiently uptaken by cells.[8,9] In addition, nanoparticles from 7-8+ nm experience in the *in-vivo* enhanced permeability and retention (EPR) effect,

which means that nanoparticles accumulate passively, and in higher concentrations, in specific tissue types (like cancer tissue) more than in normal tissue.[10] Due to the EPR Effect, nanoparticles are a very attractive modality for specific medical applications, like that of cancer medicine. In addition to "passive" accumulation (EPR), nanoparticles can be "actively targeted", being conjugated with small molecules, peptides, or antibodies for targeting to specific tissues or cells.[11,12] For example, the RGD peptide (RGDRGDRGDRGDPGC) is an example of a peptide moiety that binds to Integrin receptors, which are upregulated in cancer cells.[13] In conjunction with the EPR effect, this synergy creates a great enhancement of nanoparticle uptake for a targeted region of interest, like cancer tumor tissue (see Zhan, et. al., for example).[14] A more detailed discussion of active targeting is provided in section 1.4.1 of the introduction, as developing active targeting moieties for the treatment of macular degeneration has been a major research focus for the Kopelman laboratory.

1.1.3 The Variability of Nanoparticles from 1-200 nm, Nanohydrogels, Peg-based Nanomaterials, and Nanometals

Within the 200 nm framework, many different types of nanoparticles have been developed. As a noncomprehensive list, liposomes and micelles, dendrimers, metals (including quantum dots), shell-based nanoparticles (i.e. hydrogels), and fullerenes are examples of nanoparticle platforms in use.[2,5,15] Each of these nanoplatforms has advantages and disadvantages for biological application. For example, liposomes and micelles are often highly biocompatible, but also highly sensitive to in vivo degradation.[16] In contrast, metal-based nanoparticles are often very stable and possess desirable optical properties, but are less biocompatible.[17,18] Figure 1.2, adapted from Silva et. al,[19] pictorially classifies various nanoparticle types and provides a cartoon to realize their structure.

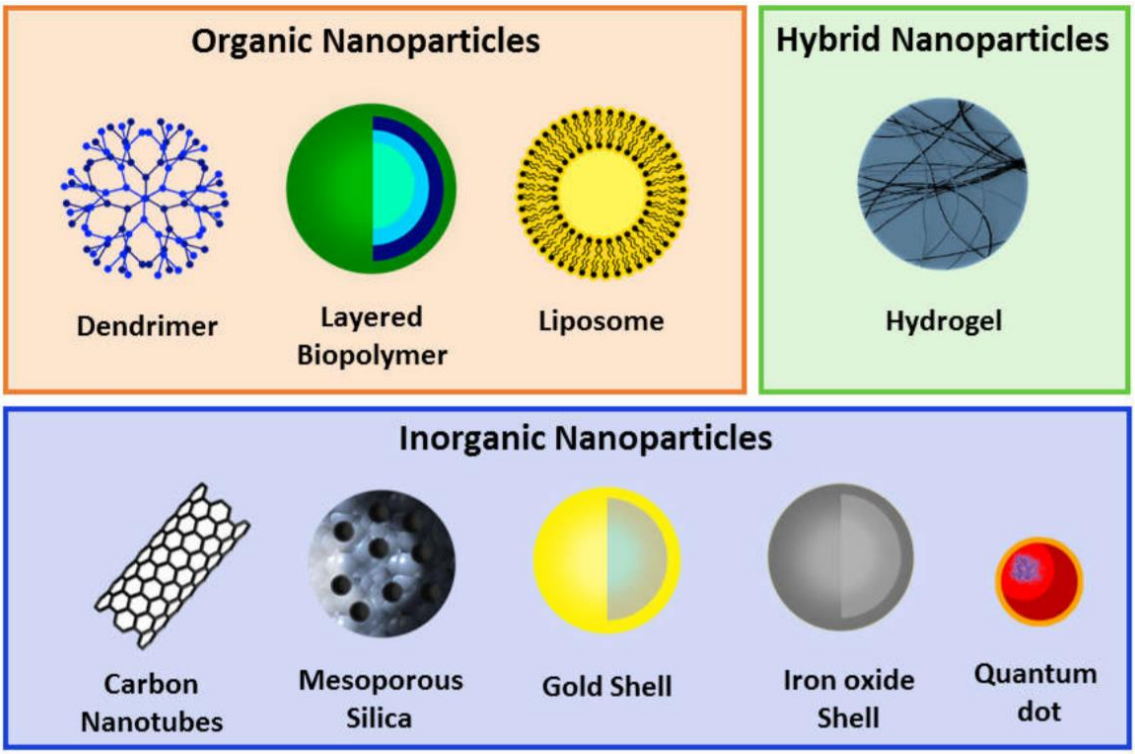

Figure 1.2 Commonly studied nanoparticle varieties. Overall, nanoparticles are divided into organic (dendrimer, biopolymer, liposome, etc.), inorganic (nanotubes, mesoporous silica, gold, iron oxide, quantum dot), or hybrid (hydrogel) categories. It is important to note that carbon nanotubes, fullerenes, and graphene, while carbon-based, are not traditionally considered an 'organic' nanoparticle, as they are allotropes of natural carbon.

Within the scope of this thesis, we investigate three types of nanoparticle platforms: 1.) Nanohydrogels (Chapter 2, polymeric acrylamide nanoshell), 2.) Nanometals (Chapters 2 and 3, Au nanoclusters[20] and nanochains), and 3.) Peg-based nanoplatforms (Chapter 4, 10k and 40k 8-arm-peg). Polymeric acrylamide nanohydrogels are highly biocompatible, customizable (size range can be synthesized from 20 – 100 nm with low standard deviation), low cost, and easy-to-conjugate shell-based nanoplatforms.[21–24] Also, due to their shell-like nature, nanohydrogels can encapsulate drugs and optical imaging agents. In contrast, peg-based nanoplatforms (8-arm-peg), are non-shell based, but smaller in

size (5 – 10 nm) than polymeric acrylamide nanohydrogels.[25,26] To emphasize the contrast between a nanoplatform with targeting and without targeting moieties, using a smaller nanoplatform like 8-arm-peg is preferable over larger nanoparticle, as the EPR effect is smaller. Lastly, Au nanoclusters and nanochains are highly useful nanomaterials due to their desirable optical properties. In brief, Au nanoclusters are an ultrasmall (1 nm), highly stable, two-photon absorbing (750 – 1000 nm) nanomaterial that produces reactive oxygen species (ROS) upon excitation. These "molecular" nanometals can be utilized to elicit cell death in select biological regions with the aid of excitation by light. We have also developed Au nanochains made of 20 nm Au monomer nanoparticles, which have a tunable (590 – 700 nm) imaging window with sub-nm resolution, a highly desirable property in biological imaging.

1.2 Nanoparticle-based Photodynamic Therapy

1.2.1 What is Photodynamic Therapy? What Determines a "Good" Photosensitizer?

Photodynamic therapy (PDT) describes any therapy that utilizes light to excite a chemical substance, formally defined as a photosensitizer, leading to the production of reactive oxygen species (ROS).[27–29] Because reactive oxygen species (ROS) are cytotoxic chemical species even at very low concentrations, the production of these reactive oxygen species leads to the killing of nearby cells very shortly after they are produced. The history of light therapy dates at least as far back as the use of the first nanoparticles: Herodotus, the famous physician of the 2nd century BC, was a proponent of heliotherapy, defined as the utilization of the radiation of the sun for therapeutic application.[30] In addition, the cultures of ancient Egypt, China, and India utilized light to treat diseases such as rickets, vitiligo, psoriasis, skin cancer, and psychosis.[30] The first modern application of phototherapy dates to the late 18th century where photodynamic therapy became established as an effective therapy for rickets.[30] Furthermore, haematoporphyrin (a porphyrin derivative) was the first molecule developed specifically for ROS production (1908).[31,32]

In recent research, many small molecule photosensitizers have been discovered, yet only a

handful of photosensitizers are clinically available for the treatment of diseases such as cancer and macular degeneration.[33] A major factor for why few photosensitizers commercially exist (besides the long time for pharmaceuticals to receive clinical approval) is because designing an effective photodynamic system has several requirements, each which create a unique set of challenges: 1.) Light must be able to penetrate the region of interest (ROI) 2.) After photo-excitation, the photosensitizer must be able to produce reactive oxygen species in a sufficient quantity to kill the ROI (group of cells, cancerous tissue, etc.), and 3.) The photosensitizing molecule must accumulate in the ROI and have no systematic toxicity. Each of these three requirements for an effective photosensitizer are discussed below.

1.) Light Penetration into Tissue

To perform photodynamic therapy, by definition, light serves as the mode to deliver the therapy. However, light penetration into tissue is highly dependent on wavelength, with redder wavelengths penetrating deepest into the skin. In fact, transitioning from 400 nm (blue) to 800 nm (near-infrared), light penetration depth into tissue can change by a factor of 10-100x.[34] Because redder wavelengths penetrate deeper into tissue, using near-infrared light (IR) is most desirable for sub-surface PDT.[34] However, ROS production efficiency begins to lose efficiency beyond 650 nm, as the energy required to create reactive oxygen species may not be met.[35] By ~850 nm, an electronic transition will not have enough potential to create ROS species.[35] This means that in selecting photosensitizers, there is a battle between optimizing penetration depth (redder wavelengths) and efficiently producing ROS species (bluer wavelengths). For one-photon photosensitizers, the efficiency problem is a major reason why few infrared single-photon dyes (700+ nm) exist, although development of IR-PDT agents is a major field of active research.[36] The issue of penetration depth versus reaction efficiency can also be resolved utilizing two-photon excitation (2p-PDT), which we explore using an $Au_{25}Capt_{18}$ nanocluster in Chapter 2 of this thesis.

2.) Efficient Production of Reactive Oxygen Species (ROS) from the Photosensitizer

Given that using near-infrared light is most desirable for sub-surface PDT, molecules must be discovered which 1.) Absorb the target wavelength efficiently (high absorption coefficient for electronic excitations, ideally in the near-infrared) and 2.) Produce efficient ROS. Typically, finding molecules to absorb in the near-infrared is the lesser of these two challenges. Many small molecule dyes and metals exist which absorb between 700-900 nm, like chlorin, phthalocyanine, BODIPY, cyanine, and KFL based molecules.[36] However, as mentioned in 1.), the efficient production of ROS becomes more challenging as redder wavelengths (650+ nm) are utilized. Assuming that the energetic requirements are sufficient (energy difference between ground and excited state), ROS production efficiency is largely determined by the excited state lifetime of the photosensitizer.[35] Overall, the longer the excited state lifetime, the more efficient ROS production will exist. This is because triplet oxygen will have more time to interact with the photosensitizer and convert triplet oxygen to singlet oxygen, when then forms and other ROS species. Following such a trend, the best photosensitizers have the longest excited triplet state lifetimes. Note that, by quantum mechanical selection rules, the original molecular excited state has to have the same multiplicity as the ground state, so as to have a strong optical absorbance, but then has to decay into a lower excited state with different multiplicity (with the aid of "relativistic quantum mechanics effects"), so as to efficiently excite the O2 molecule from its triplet ground state to its excited singlet state, an intersystem crossing transition. For example, Rose Bengal, with an ROS conversion efficiency of 70%, has an phosphorescent lifetime in the millisecond range (150 ms).[37] However, designing molecules with high ROS efficiency is highly challenging, as most molecules do not naturally possess long excited state lifetimes.

3.) Photosensitizer Accumulation and Biosafety

If a photosensitizer absorbs in the near-infrared and has optimal ROS production efficiency, for photodynamic therapy to be effective, the photosensitizer must still accumulate in the region of interest (ROI) and cause no systemic toxicity to the patient. For accumulation of a photosensitizing molecule inside the human body, several challenges exist: the photosensitizer must be soluble in the blood (i.e. have water-like solubility) and reach the ROI effectively. Despite having desirable optical properties, many photosensitizers have poor solubilities, uptake efficiencies in cells, or exhibit toxicity, rendering them unusable. Furthermore, the properties of many photosensitizers are highly sensitive to solvent environment.

1.2.2 Why Are Nanoparticles Good Candidates for PDT?

Nanoparticles are good candidates for PDT as carriers of small molecule photosensitizers. For example, polyacrylamide (PAAm) nanohydrogels can be loaded with small molecules both inside the hydrogel shell and outside the surface of the nanoparticle.[22] To protect the solvent environment of the photosensitizer, it is often most ideal to load the polyacrylamide nanohydrogel with the photosensitizer internally. To do this, if the photosensitizer is water soluble, it can be added during the synthesis of polyacrylamide hydrogels in the water phase before polymerization.[20] Once polymerization commences, the photosensitizer will be trapped inside the polyacrylamide hydrogel that forms. In addition to loading photosensitizers internally, photosensitizers can be loaded externally. For example, nanoparticles with amine functional groups on their surface can be directly conjugated to photosensitizers via an isothiocyanate functional group or utilizing MAL (maleimide)-PEG-SCM (Succinimidyl Carboxyl Methyl ester)) linkers.[38] As a model system, in the case of the PAAm nanoparticle, amine functional groups from the acrylamide and N-(3-Aminopropyl)methacrylamide hydrochloride (APMA) monomers have amine groups, therefore the former types of molecules (isothiocyanate functionalized and SCM-peg-NHS ester linkers) can bind to the surface of the PAAm nanoparticle. In the case of utilizing a MAL-PEG-SCM linker, molecules with a thiol functional group can be added in a second step to react with the maleimide group.[38]

For PAAm nanoparticles, this means that a variety of photosensitizer molecules can be utilized, as a variety of functional groups (isothiocyanate, thiol, etc.) to modify the molecule exist, and attached directly onto the nanoparticle via covalent interaction. In a typical paradigm, attaching a photosensitizer on the outside of the nanoparticle allows for ROS production to have a smaller diffusion distance into tissue, however the tradeoff is that the photosensitizer will not be kept in a consistent environment, as it will be directly exposed to the outside environment (ie tissue solvent). Hence, for different types of tissue and in different regions of the body (i.e. circulating in the blood/inside a cancer cell/inside a healthy cell), the properties of the photosensitizer may change if the photosensitizer is environmentally sensitive. For this reason, two-photon photosensitizers,[39,40] and even many one-photon photosensitizers (like methylene blue)[41] should be conjugated inside the nanoparticle to protect their optical activity.

1.2.3 Two-photon photodynamic therapy (2p-PDT)

Two-photon photodynamic therapy is defined as photodynamic therapy that occurs via the process of two-photon absorption.[42] In brief, two-photon absorption is the near-simultaneous absorption of two photons in which the energy of both photons is summed together during the quantized transition.[43] To determine the energy of the absorbed photon pair, the frequency of each photon should be summed together.[43,44] For example, the frequency of a 400 nm (blue) photon is $7.494(10)^{14}$ Hz and the frequency of an 800 nm (near-infrared) photon is $3.747(10)^{14}$ Hz. When two 800 nm photons are absorbed via two-photon absorption, the summed frequency is $7.494(10)^{14}$ Hz, equivalent to the frequency of a single 400 nm photon. Hence, the energy transition of two-photon absorption with two 800 nm photons is equivalent to that of a single 400 nm photon.

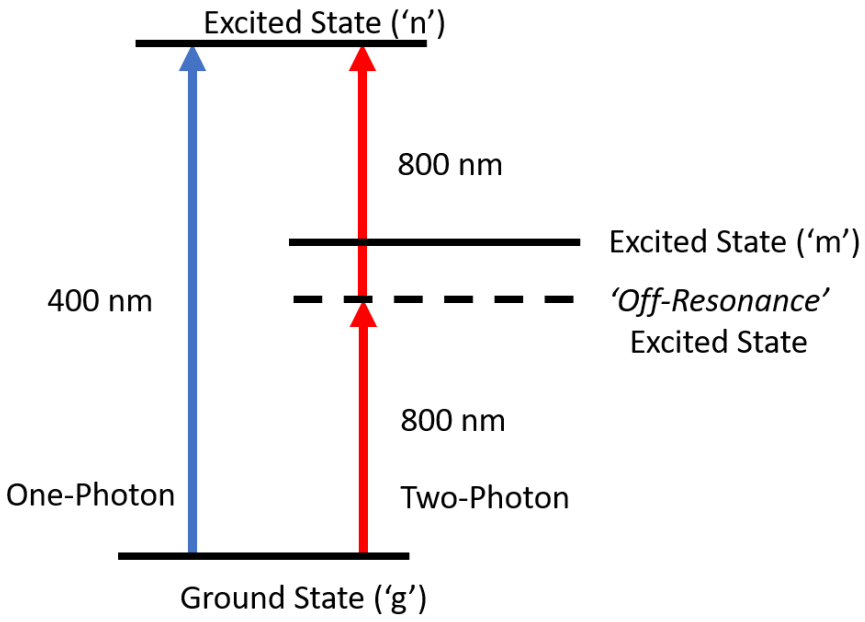

Figure 1.3 One-photon absorption (400 nm; blue) and two-photon absorption (800 nm; red) electronic processes compared side-by-side. One-photon absorption of a photon proceeds directly to the excited state (g->n). In contrast, two-photon absorption involves an intermediate ‘off-resonance’ excited state (g->m->n), whereby a second photon is absorbed to reach the excited state electronic transition.

A simplified diagram of the two-photon ‘electronic transition’, compared to its one-photon counterpart, is shown in Figure 1.3. Of important note is the inclusion of the ‘off-resonance’ excited state, as labeled in between the absorption of photons 1 and 2 in the two-photon process. In most introductory two-photon literature, this transition will most commonly be labeled as a ‘virtual state’. However, this naming convention has been criticized by experts in non-linear optics, because ‘virtual state’ is neither an intuitive term (does ‘virtual’ mean that the photon never existed in that state?), nor does it capture the photophysics of the two-photon absorption process. Instead, it has been proposed to better call this state an ‘off resonance’ excited state, which avoids the metaphysical ambiguities that the term ‘virtual’ creates, and accurately captures the photophysics of the transition.

The advantage of two-photon absorption over one photon absorption largely lies in photon penetration depth: the photon penetration depth is greater by a factor of approximately 10 for 800 nm photons compared to 400 nm photons.[42] Furthermore, whereas single 800 nm photons typically do not have the transition energy to produce ROS,[35] two 800 nm photons far surpass the energy required to produce ROS. This means that reactive oxygen species can be produced via near-IR two-photon absorption 1.) With deep penetration depth, solving the photon penetration depth problem, and 2.) With high potential cell-kill efficiencies due to the ROS energy production limit being met.

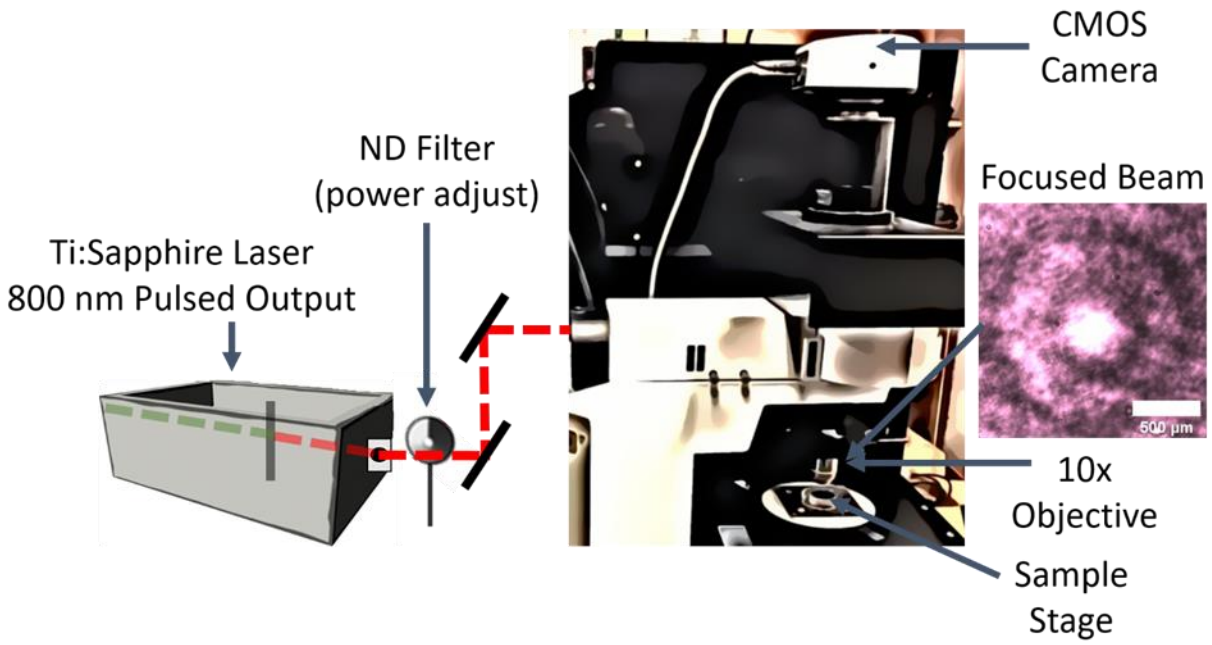

Figure 1.4 Laser setup for two-photon photodynamic therapy.

A summary of a two-photon photodynamic therapy setup, used to induce *in vitro 2p-PDT*, is provided in Figure 1.4. By using an 800 nm pulsed laser, samples can be illuminated at highly 'peak power' intensity to induce the two-photon transition. The neutral density ('ND') filter allows the excitation power to be finely adjusted, and the beam size is measured by calculating the diameter of the Airy disk that forms from the optical back-reflection into the camera detector.

1.3 Nanoparticle-based Microscopy: Dark Field Imaging and Tunable NPs

1.3.1 Plasmonic Nanoparticles in Microscopy

Metal nanoparticles are some of the most useful tools for nanomedical applications, like in microscopy-based imaging, photothermal therapy, and chemical sensing. Metal nanoparticles above 5 nm have desirable optical properties due to exhibiting plasmon resonance. In brief, plasmon resonance is the resonant oscillation of conduction electrons ('collective oscillations') in a metal.[45,46] The frequency of these electron oscillation creates a plasmon, a quasiparticle that can couple to photon oscillation.[45] Furthermore, since plasmons are the quantization of classical plasma oscillations, their properties can be derived from Maxwell's Equations (classical theory).[46] While metals like gold exhibit plasmonic effects at the bulk level (accounting for their specific color), metal nanoparticles are unique in that tuning the plasmonic interaction (thus "color") is possible. For example, the size of the nanoparticle and the geometry of the nanoparticle are both highly conductive towards photon-NP interactions. For gold nanospheres, the optical extinction maxima can be tuned from 520 nm (9 nm) to 585 nm (99 nm) by changing the NP size.[47,48] However, extending the plasmonic peak beyond 585 nm represents a major challenge, as larger gold nanoparticles have broad absorbance spectra with low peak specificity.[48] Furthermore, beyond 250 nm, the utility of large Au nanospheres becomes less practical for biological application. Lastly, fine spectral resolution control (i.e. <5-10 nm) of plasmonic extinction spectra cannot be easily obtained using sphere synthesis, as finely controlling the gold nanoparticle size presents a large practical challenge.

1.3.2 Applications of Metal Plasmonic NPs: Dark-Field Microscopy

Dark field microscopy describes an imaging modality in which light is focused onto a specimen, however a block is typically inserted after the sample to prevent direct imaging.[49] In addition, slits are made far from the center of the specimen plane, with an objective following each slit, to collect signal at a sharp angle. By utilizing the dark field approach, scattered light will largely contribute to the generated

image, whereas directly transmitted light will be blocked.[49] A summary of a typical dark-field microscopy setup is provided in Figure 1.5.

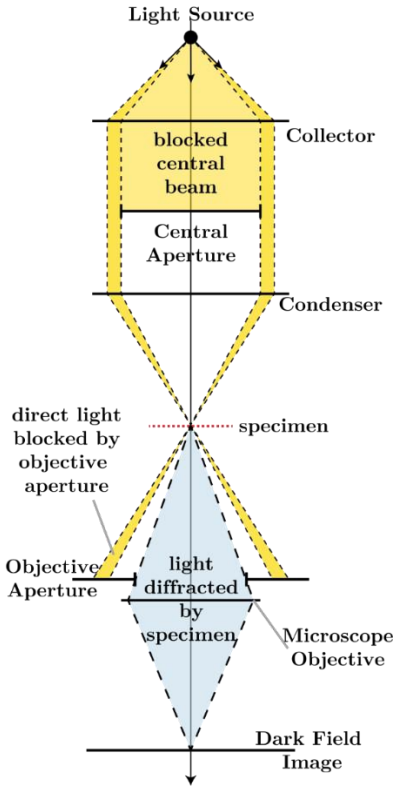

Figure 1.5 Dark field microscopy optics. The incoming light is focused onto the specimen, whereby a beam block is used to block the traditional 'light microscope' direct image of the sample. Instead, at sharp angles, scattered light is focused onto the detector to form an image.

Dark field imaging has advantages that traditional light microscopy does not offer. For example, dark field imaging allows one to image cells almost entirely free of artifacts.[49] Foremost, artifacts due to the main beam are blocked, including interference patterns and fringing. Secondly, cell artifacts like autofluorescence are minimized as the collection angle of the dark-field image can be optimized based on the wavelength of the light scattered. Since plasmonic metal nanoparticles are highly scattering, they are frequently used as contrast agents for dark-field imaging.[50] However, as mentioned previously, the extinction coefficient and scattering coefficient of metal nanoparticles will change depending on the

element selected, size of the nanoparticle, and morphology of the nanoparticle. In the next two sections (1.3.3 and 1.3.4), basic theory is outlined for the optical properties of metallic nanoparticles.

1.3.3 Free Electron 'Drude' Model

Utilizing computation to determine the properties of plasmonic NP optical materials is imperative, as modern theories are highly developed and accessible. The most basic model of plasmonic behavior is the Free Electron (Drude-Sommerfeld model). The plasmon energy from the Free Electron model is,

$$E_p = \hbar \sqrt{\frac{ne^2}{m\epsilon_0}} = \hbar\omega_p \tag{1.1}$$

Where E_p is the plasma energy, n is the conduction electron density, e is the elementary charge, m is the electron mass, ϵ_0 is the permittivity of free space, and ω_p is the plasmon frequency.

Since e, m, and ϵ_0 are constants, ω_p depends on the conduction electron density between metals (n). The conduction electron density is given by $n = ZN\rho_m/m$; where Z is the number of conduction (valence) electrons per atom, N is the Avogadro constant, ρ_m is the density of the solid (atoms/m^3), and M is the atomic mass (kilograms/atom).[51] Furthermore, by modeling the light-plasmon interaction by solving the differential equation for the well-known damped harmonic oscillator (see Mohammadzadeh et. al. for full derivation), one can see that absorption occurs when $\omega_p = \omega_{light}$.[52]

For metals like gold and silver, the plasma frequency is in the ultraviolet (139.45 nm, 137.14 nm respectively).[53] While the Drude model accurately models the plasmon behavior of bulk metals, it fails to model the behavior of nanoparticles systems with 'confined' inner electrons. Furthermore, while modified Drude models to account for nanoparticle behavior are in early development, more established models of determining the optical properties of nanoparticles are in place.[52] In the next section, 1.3.4, we briefly describe Mie Theory and the Discrete Dipole Approximation (DDA), which can be utilized to determine the optical properties of Au NPs.

1.3.4 Mie Theory and Discrete Dipole Approximation

Mie Theory is an analytical solution of Maxwell's Equations for the scattering of electromagnetic radiation interacting with particles of arbitrary size. Mie Theory is typically divided dependent on two parameters 1.) *m*, the magnitude of refractive index (n) mismatch between scattering particles and the host medium where $m = n_p/n_{med}$, and 2.) x, the size parameter of the scattering particles, determined by the ratio of the circumference of the particle to the wavelength of light ($x = 2\pi a/(\lambda/n_{med})$.[54] The Mie Solutions to electromagnetic scattering are described in detail by Bohren and Huffman.[55] Using their notation, the Mie coefficients a_n and b_n compute the amplitudes of a scattered radiative field, whereas c_n and d_n compute the amplitude of the internal field. For particles that are small compared to the radiative wavelength, Bohren and Huffman derive the absorption and scattering coefficients of a homogenous, isotropic sphere utilizing a power series expansion of spherical Bessel functions (canonical solutions to Bessel's differential equation).[55] However, Mie Theory has severe limitations, as the solutions to the wave equation have only been solved for limited geometries.

Instead of using a Mie-based approach, which requires an exact analytical solution of light interacting with a continuous object, other methods have been developed to model light-particle interactions. The discrete dipole approximation (DDA) is one of the most developed, and diverse, classical solutions to the scattering problem.[4] The discrete dipole approximation works by discretizing a continuous object into point dipoles. Whereas complex, continuous objects may not have solvable analytical solution to the wave equation, light interacting with a series of point dipoles has a known solution. Hence, by building geometries of point-dipoles, the optical properties of the material can be solved. Figure 1.6 shows point-dipole input of a sphere for input into DDSCAT. As Figure 1.6 shows, as dipole number is increased, the object more closely resembles the spheroid. This principle demonstrates that higher dipole numbers better approximate continuous objects for DDSCAT input.

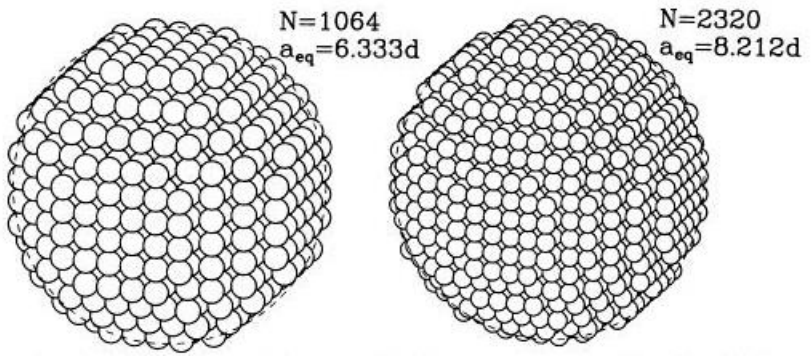

Figure 1.6 Geometry of a spheroid for typical input into the DDSCAT ('Discrete Dipole Scattering') package. As the number of dipoles is increased, the target object will be closer to its continuous morphological analogue (i.e. sphere in above case).

To study nanoparticle systems >5 nm, DDA-based approaches are frequently employed. We use the DDSCAT ('Discrete Dipole Scattering') package to simulate the optical properties of gold nanoparticles.

1.3.5 Gold Nanochains: A New Kind of Plasmon

Chapter 4 discusses the development of gold nanochains, tunable plasmonic nanosystems obtained from the polymerization of nanospheres. Within Chapter 4, we develop a protocol to "grow" nanospheroid-monomers into chain-like structures, example nanochain structures which are shown in Figure 1.7. Once the nanochains grow to the desired length, growth of the chain can be quenched by adding conjugated polyethylene glycol (PEG) capping moieties. In growing the plasmonic nanochain, the optical extinction coefficient can be tuned with approximately 1 nm resolution from 590 nm – 640 nm. In addition, using DDSCAT, we compare the optical properties of the chain from simulation and experiment.

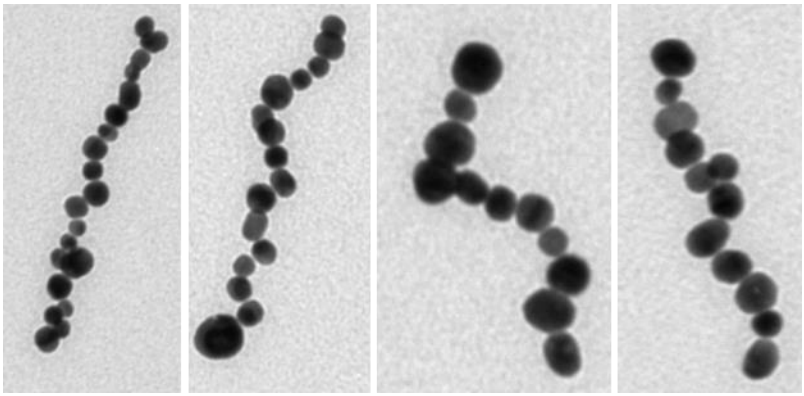

Figure 1.7 Plasmonic nanochains ('nanosnakes'), grown from Au nanospheroid monomers into linear morphologies. The average Au monomer is 20 nm in diameter.

As mentioned in 1.3.1, creating spherical plasmonic nanoparticles (monomers) with plasmonic resonance beyond 585 nm has technical barriers. At sizes beyond that of 100 nm gold NPs (585 nm resonance), the optical extinction spectra of the nanosphere becomes unfocused and red-shifting becomes insignificant. However, in synthesizing gold nanochains, we can tune the optical extinction spectra to up to 640 nm and beyond. While Chapter 4 covers tunable plasmonic nanochains from 590 – 640 nm, we have also synthesized tunable chains with optical extinction maxima up to 700 nm using the same protocol.

1.4 Nanoparticles and Targeting

1.4.1 What is Active Targeting?

Due to the differentiation of cells in the body, the receptors on the surfaces of different cell types vary. Furthermore, when cells become aberrant (cancerous, proliferating) the surface receptors further differentiate. Because of the variety in receptor expression, receptor heterogeneity can be utilized for active targeting. In short, active target describes the process of utilizing a small molecule, protein, or antibody that has a strong affinity for a specific cell receptor.[12,56] Furthermore, when this material is injected into a specimen, due to receptor expression heterogeneity, the material targets preferentially to a cluster of cells or tissue. Figure 1.8 outlines the general process of a nanoparticle-assisted, therapy-

based active-targeting paradigm. After disease diagnosis, nanoparticles with targeting moieties are injected into the patient. Due to targeting specificity, the nanoparticles will localize to the tumor region, where therapy can be treated locally.

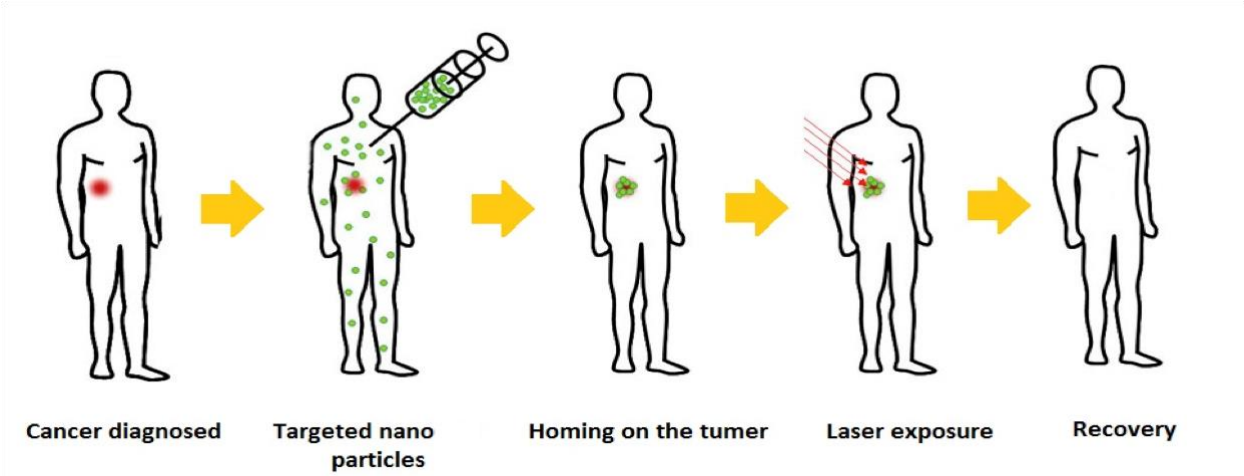

Figure 1.8 Nanoparticle-assisted active targeting in the case of photodynamic cancer therapy.

When active targeting moieties are added to nanoparticles, active targeting can increase nanoparticle localization by several factors (2-5x for many active targeting moieties, >10x in rare cases).[12] Chapter 5 of the thesis will explore nanoparticle-based active targeting for macular degeneration (MD), also known as retinal neovascularization. The following section will briefly underly the utility of active targeting to treat MD.

1.4.2 Macular Degeneration and Targeting

Macular degeneration is the leading cause of progressive vision loss among people older than 60 in developed countries, and affects 10% of people over 75.[57,58] While there are several different types of age-related macular degeneration (AMD), choroidal neovascularization is an aggressive form of AMD (10% of cases) that is caused by the angiogenesis of endothelial cells that invade the subretinal space, which in turn causes photoreceptor loss and vision degeneration. While neovascular AMD is non-cancerous, the neovascularization process is “like a cancer” in that endothelial vessel formation becomes overregulated, largely caused by high amounts of vascular endothelial growth factor (VEGF) in the retina. Hypoxia is a

corollary biological factor that triggers retinal neovascularization, as hypoxia incudible factor 1 (HIF1) becomes overexpressed in cells, leading to VEGF overexpression. Following the hypoxia model, hypoxia also alters the signaling pathway of β-adrenergic receptors. The increased activity of the β-adrenergic pathway is linked to increased VEGF production.[59] Overall, the biological causes of macular degeneration are complex, and continue to be elucidated. Due to the complex model of MD, we explore several potential targeting agents for MD therapy. Namely, within Chapter 5, we develop a peg-based nanosystem for targeting to MD regions, with RGD peptide and iobenguane (MIBG)-derivates as a potential targeting agents.

1.5 Outline of Dissertation

Chapter 1 of this dissertation defines and introduces bio-based nanoparticles (NPs) and introduces key concepts for photodynamic therapy (Ch. 2), dark field imaging (Ch. 3), macular degeneration (Ch. 4), and biological targeting (Ch. 4).

Chapter 2 introduces a new nanoparticle, $Au_{25}Capt_{18}$-Polyacrylamide (PAAm) NPs for applications in two-photon photodynamic therapy. We demonstrate highly efficacious *in vitro* two-photon PDT for these PAAm-$Au_{25}Capt_{18}$ NPs, exhibiting a tremendous enhancement in 2p-PDT-mediated cell death over one-photon PDT-mediated cell death. We demonstrate that this enhancement is associated with the high non-linear optical absorbance cross-section of the Au_{25} NC. Furthermore, we show that as a new two-photon photodynamic agent, the $Au_{25}Capt_{18}$cluster, (a) has a two-photon cross-section 8x larger when compared to 5,10,15,20-Tetrakis(1-methyl-4-pyridinio)porphyrin tetra(p-toluenesulfonate) (TMPYP), the currently most used two-photon photosensitizer, (b) has modest reactive oxygen species (ROS) production (1%) under two-photon excitation, with the potential for this efficiency to be further improved, and (c) when embedded in hydrogel NPs it maintains its unique optical properties while achieving 100% higher tumor uptake and biocompatibility.

Chapter 3 describes the synthesis and characterization of Au plasmonic nanochains for imaging applications. We fabricate and characterize highly linear plasmonic nanochains of gold nanospheres, which we call “nanosnakes”. These nanosnakes are self-assembled from bare Au nanosphere monomers with virgin surfaces, produced in DI water by laser ablation (a green, chemical-free synthesis), where the monomers are surface conjugated with small, biocompatible molecules so as to induce their assembly. These nanosnakes have several highly desirable properties for biological imaging, including two plasmonic modes, one fixed mode at 525 nm (monomer mode) and a second highly tunable mode. The secondary tunable mode ranges from 590 nm to 640 nm, with tunability precision within 1-2 nm. Such tunability towards the infrared is a highly desirable property in plasmonic imaging, due to these photons’ deeper tissue penetration as well as due to their much reduced background cell fluorescence. We also show that the nanosnakes possess scattering cross-sections up to 40x higher than the Au nanosphere monomers (approximately 3x higher per chain monomer nanosphere), thus making them better contrast agents for imaging applications, noting that gold NPs are utilized for both dark-field and X-ray imaging. Lastly, we demonstrate that the nanosnakes can be easily conjugated with active targeting moieties, for applications such as targeted cancer and heart disease phototherapy, using the RGD peptide as a model system; furthermore, we show that they are also non-toxic to cells, even at very high concentrations, up to concentrations as high as 0.25 mg/mL NP mass concentration (OD:5). Overall, the nanosnakes represent a promising new imaging modality for dark-field, SERS, and high resolution microscopy, and have a high potential for *in vivo* theranostic applications.

Chapter 4 describes the development of targeted nanosystems for the diagnosis of macular degeneration, wherein we evaluate fluorescent 8-arm-peg NPs for their RGD-assisted targeting to the age-related macular degeneration (AMD) neovasculature. *In vitro* experiments reveal a strong, measurable difference between non-targeted and RGD targeted NPs, with the RGD targeted NPs showing nearly a 100 % increase in cellular uptake. This 8-arm-peg-based RGD targeting exhibits a concentration dependence,

with the highest incubated NP concentration (3 mg/mL) providing the greatest *in vitro* contrast. *In vivo* experiments at high incubated PEG-RGD concentrations (20 mg/mL injections) show approximately 15-20% enhancement in targeting signal, when compared to non-RGD controls. Overall, we show that 8-arm PEG NPs are a new, readily conjugatable and targetable nanosystem for future optimized AMD diagnosis and therapy, with potential benefits for *in vivo* theranostic enhancement.

Lastly, Chapter 5 is the conclusion to this dissertation, summarizing key points and future implications from Chapters 2-4.

1.6 References

(1) Jones, A. A. D.; Mi, G.; Webster, T. J. A Status Report on FDA Approval of Medical Devices Containing Nanostructured Materials. *Trends Biotechnol.* **2019**, *37* (2), 117–120. https://doi.org/10.1016/j.tibtech.2018.06.003.

(2) Bhatia, S. Natural Polymer Drug Delivery Systems; **2016**. https://doi.org/10.1007/978-3-319-41129-3.

(3) Cohen, S.; Au, S.; Panté, N. How Viruses Access the Nucleus. *Biochim. Biophys. Acta - Mol. Cell Res.* **2011**, *1813* (9), 1634–1645. https://doi.org/10.1016/j.bbamcr.2010.12.009.

(4) Draine, B. T.; Flatau, P. J. Discrete-Dipole Approximation For Scattering Calculations. *J. Opt. Soc. Am. A* **1994**, *11* (4), 1491. https://doi.org/10.1364/josaa.11.001491.

(5) Sattler, K. D. *Handbook of Nanophysics: Nanoparticles and Quantum Dots*; 2016.

(6) Ochekpe, N. A.; Olorunfemi, P. O.; Ngwuluka, N. C. Nanotechnology and Drug Delivery Part 1: Background and Applications. *Trop. J. Pharm. Res.* **2009**, *8* (3), 265–274.

(7) Sasaki, K.; Shi, Z. Y.; Kopelman, R.; Masuhara, H. Three-Dimensional PH Microprobing with an Optically-Manipulated Fluorescent Particle. *Chemistry Letters*. 1996, 25 (2), 141–142. https://doi.org/10.1246/cl.1996.141.

(8) Jani, P.; Halbert, G. W.; Langride, J.; Florence, A. T. Nanoparticle Uptake by the Rat Gastrointestinal Mucosa: Quantitation and Particle Size Dependency. *J. Pharm. Pharmacol.* **1990**, *42* (12), 821–826. https://doi.org/10.1111/j.2042-7158.1990.tb07033.x.

(9) Chithrani, B. D.; Ghazani, A. A.; Chan, W. C. W. Determining the Size and Shape Dependence of Gold Nanoparticle Uptake into Mammalian Cells. *Nano Lett.* **2006**, *6* (4), 662–668. https://doi.org/10.1021/nl052396o.

(10) Nakamura, H.; Jun, F.; Maeda, H. Development of Next-Generation Macromolecular Drugs Based on the EPR Effect: Challenges and Pitfalls. *Expert Opin. Drug Deliv.* **2015**, *12* (1), 53–64. https://doi.org/10.1517/17425247.2014.955011.

(11) Steichen, S. D.; Caldorera-Moore, M.; Peppas, N. A. A Review of Current Nanoparticle and Targeting Moieties for the Delivery of Cancer Therapeutics. *Eur. J. Pharm. Sci.* **2013**, *48* (3), 416–427. https://doi.org/10.1016/j.ejps.2012.12.006.

(12) Muhamad, N.; Plengsuriyakarn, T.; Na-Bangchang, K. Application of Active Targeting Nanoparticle Delivery System for Chemotherapeutic Drugs and Traditional/Herbal Medicines in Cancer Therapy: A Systematic Review. *Int. J. Nanomedicine* **2018**, *13*, 3921–3935. https://doi.org/10.2147/IJN.S165210.

(13) Park, J.; Singha, K.; Son, S.; Kim, J.; Namgung, R.; Yun, C. O.; Kim, W. J. A Review of RGD-Functionalized Nonviral Gene Delivery Vectors for Cancer Therapy. *Cancer Gene Ther.* **2012**, *19* (11), 741–748. https://doi.org/10.1038/cgt.2012.64.

(14) Zhan, C.; Gu, B.; Xie, C.; Li, J.; Liu, Y.; Lu, W. Cyclic RGD Conjugated Poly(Ethylene Glycol)-Co-Poly(Lactic Acid) Micelle Enhances Paclitaxel Anti-Glioblastoma Effect. *J. Control. Release* **2010**, *143* (1), 136–142. https://doi.org/10.1016/j.jconrel.2009.12.020.

(15) Ealias, A. M.; Saravanakumar, M. P. A Review on the Classification, Characterisation, Synthesis of Nanoparticles and Their Application. *IOP Conf. Ser. Mater. Sci. Eng.* **2017**, *263* (3). https://doi.org/10.1088/1757-899X/263/3/032019.

(16) Schwendener, R. A.; Schott, H. Liposome Formulations of Hydrophobic Drugs. *Liposomes.* **2010**, 605, 129-138. https://doi.org/10.1007/978-1-60327-360-2_8.

(17) Mukherjee, S.; Patra, C. R. Biologically Synthesized Metal Nanoparticles: Recent Advancement

and Future Perspectives in Cancer Theranostics. *Futur. Sci. OA* **2017**, *3* (3). https://doi.org/10.4155/fsoa-2017-0035.

(18) Zhang, X. D.; Wu, D.; Shen, X.; Liu, P. X.; Fan, F. Y.; Fan, S. J. In Vivo Renal Clearance, Biodistribution, Toxicity of Gold Nanoclusters. *Biomaterials* **2012**, *33* (18), 4628–4638. https://doi.org/10.1016/j.biomaterials.2012.03.020.

(19) Silva, S.; Almeida, A. J.; Vale, N. Combination of Cell-Penetrating Peptides with Nanoparticles for Therapeutic Application: A Review. *Biomolecules* **2019**, *9* (1), 1–24. https://doi.org/10.3390/biom9010022.

(20) McLean, A.; Wang, R.; Huo, Y.; Cooke, A.; Hopkins, T.; Potter, N.; Li, Q.; Isaac, J.; Haidar, J.; Jin, R.; Kopelman R. Synthesis and Optical Properties of Two-Photon-Absorbing Au25(Captopril)18-Embedded Polyacrylamide Nanoparticles for Cancer Therapy. *ACS Appl. Nano Mater.* **2020**, *3* (2), 1420–1430. https://doi.org/10.1021/acsanm.9b02272.

(21) Wenger, Y.; Schneider, R. J.; Reddy, G. R.; Kopelman, R.; Jolliet, O.; Philbert, M. A. Tissue Distribution and Pharmacokinetics of Stable Polyacrylamide Nanoparticles Following Intravenous Injection in the Rat. *Toxicol. Appl. Pharmacol.* **2011**, *251* (3), 181–190. https://doi.org/10.1016/j.taap.2010.11.017.

(22) Shirakura, T.; Kelson, T. J.; Ray, A.; Malyarenko, A. E.; Kopelman, R. Hydrogel Nanoparticles with Thermally Controlled Drug Release. *ACS Macro Lett.* **2014**, *3* (7), 602–606. https://doi.org/10.1021/mz500231e.

(23) Ray, A.; Wang, X.; Lee, Y. E. K.; Hah, H. J.; Kim, G.; Chen, T.; Orringer, D. A.; Sagher, O.; Liu, X.; Kopelman, R. Targeted Blue Nanoparticles as Photoacoustic Contrast Agent for Brain Tumor Delineation. *Nano Res.* **2011**, *4* (11), 1163–1173. https://doi.org/10.1007/s12274-011-0166-1.

(24) Ray, A.; Yoon, H. K.; Koo Lee, Y. E.; Kopelman, R.; Wang, X. Sonophoric Nanoprobe Aided PH Measurement in Vivo Using Photoacoustic Spectroscopy. *Analyst* **2013**, *138* (11), 3126–3130. https://doi.org/10.1039/c3an00093a.

(25) Avula, U. M. R.; Yoon, H. K.; Lee, C. H.; Kaur, K.; Ramirez, R. J.; Takemoto, Y.; Ennis, S. R.; Morady, F.; Herron, T.; Berenfeld, O.; et al. Cell-Selective Arrhythmia Ablation for Photomodulation of Heart Rhythm. *Sci. Transl. Med.* **2015**, *7* (311). https://doi.org/10.1126/scitranslmed.aab3665.

(26) Hopkins, T.; Swanson, S. D.; Hoff, J. D.; Potter, N.; Ukani, R.; Kopelman, R. Ultracompact Nanotheranostic PEG Platform for Cancer Applications. *ACS Appl. Bio Mater.* **2018**, *1* (4), 1094–1101. https://doi.org/10.1021/acsabm.8b00315.

(27) Dolman, D.; Fukumura, D.; Jain, R. Photodynamic Therapy for Cancer. *Nat. Rev. Cancer* **2003**, *3* (5), 380–387.

(28) Yoon, I.; Li, J. Z.; Shim, Y. K. Advance in Photosensitizers and Light Delivery for Photodynamic Therapy. *Clin. Endosc.* **2013**, *46* (1), 7–23. https://doi.org/10.5946/ce.2013.46.1.7.

(29) Lucky, S. S.; Soo, K. C.; Zhang, Y. Nanoparticles in Photodynamic Therapy. *Chem. Rev.* **2015**, *115* (4), 1990–2042. https://doi.org/10.1021/cr5004198.

(30) Daniell, M. D.; Hill, J. S. A History of Photodynamic Therapy. *Aust. N. Z. J. Surg.* **1991**, *61* (5), 340–348. https://doi.org/10.1111/j.1445-2197.1991.tb00230.x.

(31) Hausmann, W.; Kolmer, W. Uber Die Sensibilisierende Wirkung Pflanzlicher Und Tierischer Farbstoffe Auf Paramecium. *Biochem. Z.* **1908**, 15, 13-18.

(32) Hausmann, W. Die Sensibilisierende Wirkung Tierischer Farbstoffe Und Ihre Physiologische Bedeutung. *Wien. Klin. Wchnschr.* **1908**, 7 (21), 1527-1529.

(33) Baskaran, R.; Lee, J.; Yang, S.-G. Clinical Development of Photodynamic Agents and Therapeutic Applications. *Biomater. Res.* **2018**, *22* (1), 1–8. https://doi.org/10.1186/s40824-018-0140-z.

(34) Jacques, S. L. Optical Properties of Biological Tissues: A Review; Corrigendum. *Phys. Med. Biol.* **2013**, *58* (14), R37–R61, 5007–5008. https://doi.org/10.1088/0031-9155/58/14/5007.

(35) Plaetzer, K.; Krammer, B.; Berlanda, J.; Berr, F.; Kiesslich, T. Photophysics and Photochemistry of Photodynamic Therapy: Fundamental Aspects. *Lasers Med. Sci.* **2009**, *24* (2), 259–268. https://doi.org/10.1007/s10103-008-0539-1.

(36) Chinna Ayya Swamy, P.; Sivaraman, G.; Priyanka, R. N.; Raja, S. O.; Ponnuvel, K.; Shanmugpriya, J.; Gulyani, A. Near Infrared (NIR) Absorbing Dyes as Promising Photosensitizer for Photo Dynamic Therapy. *Coord. Chem. Rev.* **2020**, *411*, 213233. https://doi.org/10.1016/j.ccr.2020.213233.

(37) Stiel, H.; Teuchner, K.; Paul, A.; Leupold, D.; Kochevar, I. E. Quantitative Comparison of Excited State Properties and Intensity-Dependent Photosensitization by Rose Bengal. *J. Photochem. Photobiol. B Biol.* **1996**, *33* (3), 245–254. https://doi.org/10.1016/1011-1344(95)07248-9.

(38) Hermanson, G. *Bioconjugate Techniques*; 2008.

(39) Johnsen, M.; Ogilby, P. R. Effect of Solvent on Two-Photon Absorption by Vinyl Benzene Derivatives. *J. Phys. Chem. A* **2008**, *112* (34), 7831–7839. https://doi.org/10.1021/jp8020326.

(40) Drobizhev, M.; Makarov, N. S.; Tillo, S. E.; Hughes, T. E.; Rebane, A. Two-Photon Absorption Properties of Fluorescent Proteins. *Nat. Methods* **2011**, *8* (5), 393–399. https://doi.org/10.1038/nmeth.1596.

(41) Tang, W.; Xu, H.; Park, E. J.; Philbert, M. A.; Kopelman, R. Encapsulation of Methylene Blue in Polyacrylamide Nanoparticle Platforms Protects Its Photodynamic Effectiveness. *Biochem. Biophys. Res. Commun.* **2008**, *369* (2), 579–583. https://doi.org/10.1016/j.bbrc.2008.02.066.

(42) Ogawa, K.; Kobuke, Y. Recent Advances in Two-Photon Photodynamic Therapy. *Anticancer. Agents Med. Chem.* **2008**, *8*, 269–279.

(43) Pawlicki, M.; Collins, H. A.; Denning, R. G.; Anderson, H. L. Two-Photon Absorption and the Design of Two-Photon Dyes. *Angew. Chemie - Int. Ed.* **2009**, *48* (18), 3244–3266. https://doi.org/10.1002/anie.200805257.

(44) Boyd, R. *Nonlinear Optics*; **2019**.

(45) Pines, D.; Bohm, D. A Collective Description of Electron Interactions: II. Collective vs Individual Particle Aspects of the Interactions. *Phys. Rev.* **1952**, *85* (2), 338–353. https://doi.org/10.1103/PhysRev.85.338.

(46) Yu, H.; Peng, Y.; Yang, Y.; Li, Z. Y. Plasmon-Enhanced Light–Matter Interactions and Applications. *npj Comput. Mater.* **2019**, *5* (1), 1–14. https://doi.org/10.1038/s41524-019-0184-1.

(47) Huang, X.; El-Sayed, M. A. Gold Nanoparticles: Optical Properties and Implementations in Cancer Diagnosis and Photothermal Therapy. *J. Adv. Res.* **2010**, *1* (1), 13–28. https://doi.org/10.1016/j.jare.2010.02.002.

(48) Ziegler, C.; Eychmüller, A. Seeded Growth Synthesis of Uniform Gold Nanoparticles with Diameters of 15-300 Nm. *J. Phys. Chem. C* **2011**, *115* (11), 4502–4506. https://doi.org/10.1021/jp1106982.

(49) Gage, SH. Modern Dark-Field Microscopy and the History of Its Development. *Transactions of the American Microscopial Society,* **1920**, 95-141.

(50) Liu, M.; Chao, J.; Deng, S.; Wang, K.; Li, K.; Fan, C. Dark-Field Microscopy in Imaging of Plasmon Resonant Nanoparticles. *Colloids Surfaces B Biointerfaces* **2014**, *124*, 111–117. https://doi.org/10.1016/j.colsurfb.2014.06.001.

(51) Ashcroft, N.; Mermin, N. Solid State Physics, **1976**.

(52) Kheirandish, A.; Sepehri Javan, N.; Mohammadzadeh, H. Modified Drude Model for Small Gold Nanoparticles Surface Plasmon Resonance Based on the Role of Classical Confinement. *Sci. Rep.* **2020**, *10* (1), 1–10. https://doi.org/10.1038/s41598-020-63066-9.

(53) Ordal, M. A.; Bell, R. J.; Alexander, R. W.; Long, L. L.; Querry, M. R. Optical Properties of Fourteen Metals in the Infrared and Far Infrared: Al, Co, Cu, Au, Fe, Pb, Mo, Ni, Pd, Pt, Ag, Ti, V, and W. *Appl. Opt.* **1985**, *24* (24), 4493. https://doi.org/10.1364/ao.24.004493.

(54) Grainger, R. G.; Lucas, J.; Thomas, G. E.; Ewen, G. B. L. Calculation of Mie Derivatives. *Appl. Opt.* **2004**, *43* (28), 5386–5393. https://doi.org/10.1364/AO.43.005386.

(55) Bohren, C. F. *Absorption and Scattering of Light by Small Particles*; **1983**. https://doi.org/10.1088/0031-9112/35/3/025.

(56) Bazak, R.; Houri, M.; El Achy, S.; Kamel, S.; Refaat, T. Cancer Active Targeting by Nanoparticles: A Comprehensive Review of Literature. *J. Cancer Res. Clin. Oncol.* **2015**, *141* (5), 769–784. https://doi.org/10.1007/s00432-014-1767-3.

(57) Wong, W. L.; Su, X.; Li, X.; Cheung, C. M. G.; Klein, R.; Cheng, C. Y.; Wong, T. Y. Global Prevalence of Age-Related Macular Degeneration and Disease Burden Projection for 2020 and 2040: A Systematic Review and Meta-Analysis. *Lancet Glob. Heal.* **2014**, *2* (2), e106–e116. https://doi.org/10.1016/S2214-109X(13)70145-1.

(58) Klein, R.; R, K.; BE, K.; RA, H.; I, B.; SP, K.; J, S. Prevalence of Age-Related Macular Degeneration in the US Population. *Arch. Ophthalmol.* **2011**, *129* (1), 75. https://doi.org/10.1001/archophthalmol.2010.318.

(59) Casini, G.; Dal Monte, M.; Fornaciari, I.; Filippi, L.; Bagnoli, P. The β-Adrenergic System as a Possible New Target for Pharmacologic Treatment of Neovascular Retinal Diseases. *Prog. Retin. Eye Res.* **2014**, *42*, 103–129. https://doi.org/10.1016/j.preteyeres.2014.06.001.

Chapter 2: Synthesis and Optical Properties of Two-photon Absorbing $Au_{25}Captopril_{18}$-Embedded Polyacrylamide Nanoparticles for Cancer Therapy

2.1 Abstract

$Au_{25}(Captopril)_{18}$ nanoclusters (NCs) are a 1.2 nm water-soluble metal nanomaterial with strong two-photon absorption, excited-state reactive oxygen production, and of potential applicability for biomedical imaging and 2-photon photodynamic therapy (2p-PDT). Due to the low cellular uptake of $Au_{25}(Captopril)_{18}$ clusters, its limited potential for conjugation with targeting agents, and to enhance its biocompatibility, we embedded these clusters into hydrogel nanoparticles (NPs), by synthesizing polyacrylamide-encapsulated $Au_{25}(Capt)_{18}$ nanoparticles (PAAm-$Au_{25}(Capt)_{18}$ NPs). We verified that the two-photon absorption and singlet oxygen production of these PAAm-Au_{25} NPs still exhibit the favorable properties of the original metal nanocluster. Furthermore, the Au_{25}-encapsulated polyacrylamide nanoparticles have enhanced *in vitro* cell uptake, can be easily conjugated to targeting moieties, and exhibit significantly higher biocompatibility. Photo-irradiation experiments on HeLa cancer cells incubated with these PAAm-$Au_{25}(Capt)_{18}$ NPs reveal excellent 2p-PDT efficacy, in contrast to 1p-PDT, thus demonstrating their promising potential for cancer PDT with infrared light that penetrates deeply into live tissue.

2.2 Introduction

Au_{25} nanoclusters are ultra-small (<2 nm), highly unique, molecular nanomaterials, with promising applications to biomedicine,[3–6] catalysis,[7–9] and energy storage.[10,11] Regarding biomedical applications, *Au_{25}* nanoclusters have a promising potential for two-photon photodynamic therapy (2p-PDT). Two-photon photodynamic therapy is the process of using two low energy photons, in a non-linear optical process, to excite a photosensitizing dye. In 2p-PDT, after excitation, energy transfer from the

dye's excited state (ES), to triplet oxygen molecules (O_2), produces reactive oxygen species (ROS). Because reactive oxygen species are cytotoxic, this process can be used to elicit the death of anomalous, pathology driving cells, but only in the highly selectively excited tissue regions.[12–14] At the molecular level, two factors dictate the efficacy of photodynamic therapy dyes: optical absorbance and reactive oxygen production efficiency.[15] Since Au_{25} clusters display high polarizability under photo-excitation, they have extremely high two-photon cross-sections (high optical absorbance).[16,17] In addition, the Au_{25} nanoclusters have been shown to produce reactive oxygen species (ROS) upon photo-excitation. For example, Au_{25} clusters have been used to generate reactive oxygen for ROS-mediated chemical conversion with yields as high as 50%.[18] Au_{25} is also an ideal photodynamic therapy candidate because near-infrared light (800 nm) is used for its excitation. Using such near-IR light has two advantages: 1. Negligible photodamage and 2. Near-IR light exhibits the lowest scattering and thus the deepest penetration into the skin and tissue, making near-IR wavelengths most desirable for sub-surface PDT.[19] Since the availability of one-photon near-IR PDT agents is limited, two-photon PDT agents like Au_{25} need be explored.[20] A schematic of the two-photon PDT process for $Au_{25}(Capt)_{18}$ clusters is given in Figure 2.1. In this figure, incoming light (red) represents 800 nm pulsed light leading to strong two-photon absorption into the excited state (ES), followed by the triplet to singlet oxygen (O_2) conversion required for the PDT processes.

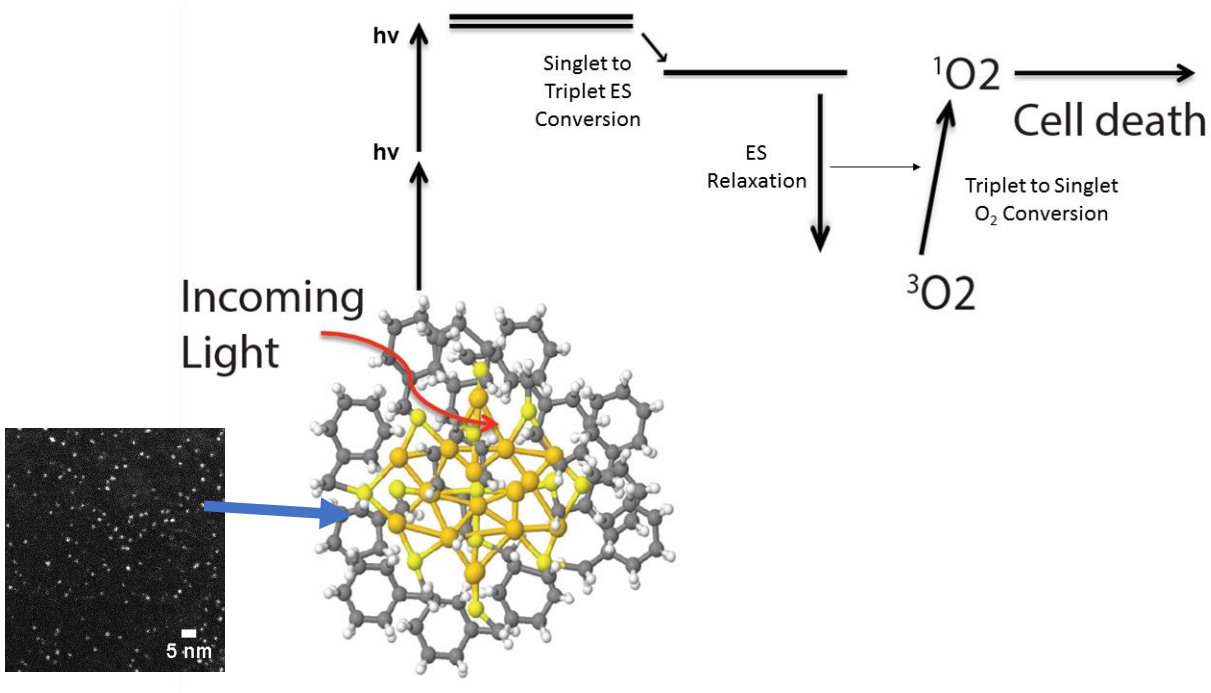

Figure 2.1 Schematic of reactive oxygen production from Au_{25} nanoclusters upon two-photon excitation, where ES is the excited state. The example Au cluster shown in this figure is $Au_{25}Captopril_{18}$ and a TEM of the 1.2 nm clusters is provided.

Gold nanoclusters of other sizes exist (i.e. Au_4, Au_{15}, Au_{28}, Au_{38}, Au_{44}, Au_{144})[17,21,22], however, Au_{25} should be viewed as the most substantiated candidate for two-photon PDT applications. To evaluate molecular absorbance efficiency among nanocluster materials, the "Two-photon Absorption/Volume" ratio (A/V) has been established as an important parameter.[23] Au_{25}, Au_{38}, and Au_{144} clusters have radii ratio of 0.5 nm, 0.65 nm, and 0.8 nm and two-photon cross-section coefficients of $2.0(10)^{-10}$, $3.5(10)^{-10}$, and $7.0(10)^{-10}$ (m/W), respectively.[24,25] Among these clusters, Au_{25} has the best A/V ratio (1.0 vs. 0.80 and 0.85 $W^{-1}m^{-2}$). Furthermore, we note that while larger Au clusters, like $Au_{144}(C_6H_{13}S)$, have a more efficient singlet oxygen production [factor of 2 higher than $Au_{25}(SG)_{18}$], they are not water soluble.[23] On

the other hand, smaller Au clusters like Au_{15} have a high (A/V) ratio, but no proven utility for reactive oxygen production, even under one-photon excitation.[26]

Among the *Au_{25}* variants, most are impractical for in-vivo applications, as few are soluble in water. Notably, water solubility enables embedding in nanogels. $Au_{25}(SG)_{18}$ (SG = $C_{10}H_{17}N_3O_6S$), the most characterized Au_{25} water soluble nanocluster, has been explored for *in-vitro* two-photon photodynamic therapy.[23] The here presented *$Au_{25}(Captopril)_{18}$* – or *$Au_{25}(Capt)_{18}$* -- is a new generation, water soluble, *Au_{25}* nanocluster with significantly higher thermal stability than the glutathione (SG) cluster.[27,28] *$Au_{25}(Capt)_{18}$* has been shown to produce reactive oxygen with 420-460 nm excitation.[18,29] In addition, an *$Au_{25}(Capt)_{18}$ in vitro* one-photon PDT efficacy, even with a concentration as low as 5 μg/mL, was also demonstrated under 420-460 nm excitation.[29] While *$Au_{25}(Capt)_{18}$* has improved thermal properties and proven reactive oxygen generation, efficient cellular targeting with Au clusters is a major challenge for biomedical applications, as cell uptake is low.[30] Furthermore, as we show, high incubation concentrations (>0.1 mg/mL) of these nanoclusters negatively affect cellular metabolism and viability.

To increase cellular uptake and biocompatibility, we have developed larger, biocompatible polyacrylamide nanohydrogels to encapsulate the gold cluster. Polyacrylamide nanohydrogels (PAAm) have been used before to encapsulate photodynamic agents, exhibiting *in vitro* targeting efficiencies beyond 90%.[31] Furthermore, polyacrylamide particles do not produce acute organ damage or other measurable signs of toxicity.[32,33] In addition, polyacrylamide nanoparticles benefit from the enhanced permeability and retention (EPR) effect *in vivo* and can be conjugated with cancer cell targeting peptides.[33,34] Lastly, for two-photon absorbing molecules specifically, it is important to provide a protected, stable environment, as the two-photon cross-section is highly sensitive to local protein electric fields.[35,36] As such, polyacrylamide nanohydrogels have a highly stable solvent environment, preserving the photodynamic capacity of solvent-sensitive dyes like methylene blue.[37]

In this work we investigate the potential of polyacrylamide-encapsulated $Au_{25}(Capt)_{18}$ for two-photon photodynamic therapy (2p-PDT). In synthesizing $Au_{25}(Capt)_{18}$ nanoclusters inside of the polyacrylamide nano-matrix,[33,38] we find the favorable two-photon absorption and singlet oxygen efficiency to be preserved between the metal nanocluster and this cluster when encapsulated in polyacrylamide. Furthermore, in comparing Au_{25} and the encapsulated PAAm-Au_{25}, we find that PAAm-Au_{25} has better targeting to cells and has significantly higher biocompatibility compared to non-encapsulated Au_{25}. Finally, we find that, in complete contrast to 1p-PDT, PAAm-$Au_{25}(Captopril)_{18}$ nanoparticles exhibit high efficacy under 2p-PDT excitation. The latter is of high significance for potential in-vivo PDT.

2.3 Experimental Procedures

2.3.1 Synthesis of $Au_{25}(Capt)_{18}$.

160 mg of $HAuCl_4 \cdot 3H_2O$ and 250 mg of tetraoctylammonium bromide (TOABr) were first dissolved in 30 mL of methanol, and the solution was vigorously stirred for ~15 min until the color changed from yellow to deep red. Then, 435 mg of captopril was rapidly added to the above reaction mixture under stirring; the solution color quickly changed to white. After ~60 min, 150 mg of $NaBH_4$ (dissolved in 7 ml of ice-cold water) was rapidly added to the reaction mixture under vigorous stirring; the solution color immediately turned brown-black. The reaction was allowed to proceed for 24 to 48 h under constant stirring, during which a spontaneous “size-focusing” process occurred, with the unstable clusters decomposed or converted, giving rise to pure $Au_{25}(Capt)_{18}$ nanoclusters with the characteristic UV-vis absorption peaks at 450 and 680 nm (Figure 2.1).

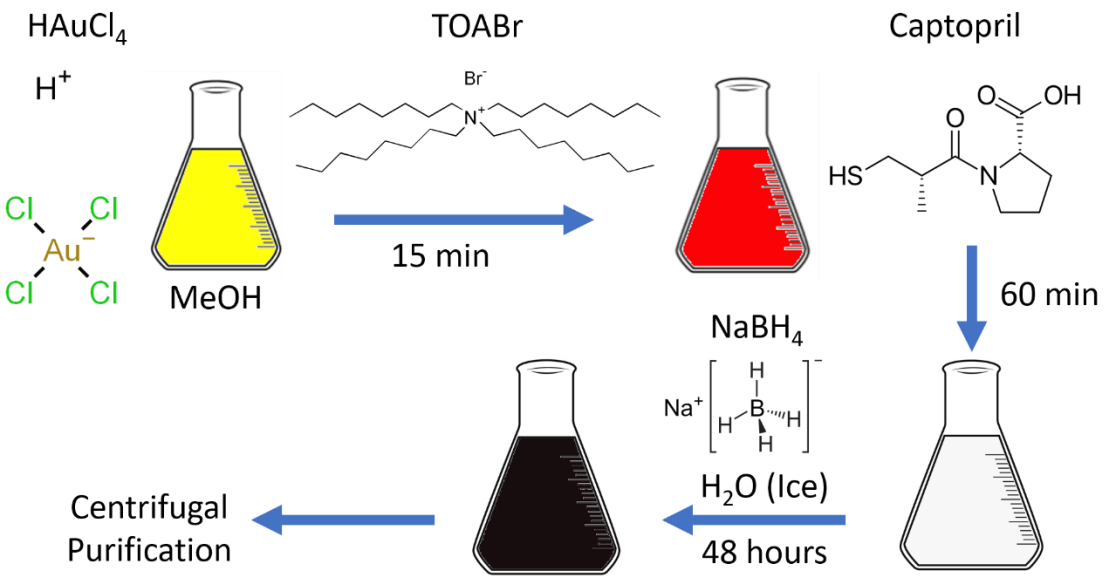

Figure 2.2 Synthetic steps to synthesize the $Au_{25}Capt_{18}$ cluster. Color changes (left to right; top to bottom) are bright yellow, fluorescent red, cream white, and dark black/purple for each synthetic step accordingly.

After the reaction, the mixture was first centrifuged to remove the unreacted, insoluble Au(I):SR polymers (4000 g; 5 min). The supernatant was collected and concentrated by rotary evaporation. The $Au_{25}(Capt)_{18}$ clusters were precipitated by adding excess ethanol to the solution, followed by centrifugation (4000 g; 30 min). The collected $Au_{25}(Capt)_{18}$ precipitate was washed with ethanol several times (3x) and finally dried under vacuum. Typically, ~15 mg $Au_{25}(Capt)_{18}$ with high purity can be obtained in such a synthesis.

2.3.2 Synthesis of PAAm-$Au_{25}(Capt)_{18}$ Hydrogel Nanoparticles.

A solution of 10 mL hexane, 0.357 g AOT, and 0.733 mL Brij30 was added to a 25 mL RB flask and purged under argon while stirring for 20 minutes.[39] Brij was weighed gravimetrically for increased accuracy. The particles were stirred at 600-700 RPM. 122.67 mg of acrylamide and 9.33 mg of APMA were dissolved in 0.31 mL of PBS, and 43 mg of AHM was added. Next, 15 mg of $Au_{25}(Capt)_{18}$ was added to solution. The PBS solution was then injected dropwise into the hexane solution, followed by 33.33 microliters of TEMED, and finally a 10% APS solution of water. The hexanes were evaporated using a rotovap machine

and the remaining particles were washed 5 times with ethanol, followed by 5 washes with water. After, samples were freeze-dried and stored under freezing.

2.3.3 Transmission Electron Microscopy.

JEM 1400 TEM: Transmission electron microscopy was performed using a JEOL JEM 1400 electron microscope at 80 kV in vacuum. Samples were loaded onto a pre-plasma oxidized 200 well copper grid. For loading, a 5 µL sample of PAAm-$Au_{25}(Capt)_{18}$ prepared at 20 mg/mL was drop-added onto the grid. After waiting 30 seconds, a piece of #1 Whatman filter was used to wick the liquid on the edge of the grid. Next, after drop-washing with 5 µL of distilled water, a sample of 5 µL 1% uranyl acetate was applied. After 3 minutes of incubation, the #1 Whatman filter was used to remove any excess uranyl acetate stain.

JEM 2100F *High Resolution STEM* (scanning transmission electron microscopy)*:* A JEOL JEM 2100F with a CEOS STEM corrector mounted was used for imaging the Au_{25} samples working in STEM mode. Both STEM bright-field (BF) and High angle annular dark-field (HAADF) images were taken simultaneously. The specimen in the STEM study was prepared by placing a drop of a sample solution (20 mg/mL) on a Holey-carbon film coated Cu grid and let to dry before loading it into a TEM holder.

2.3.4 One-photon Absorption and Fluorescence.

Absorption was measured using a Shimadzu UV-Vis. All samples were prepared in 1 cm disposable cuvettes in PBS ($Au_{25}Capt_{18}$, PAAm-$Au_{25}Capt_{18}$) or methanol (Coumarin 183). Fluorescence measurements were performed using a Horiba Floromax 4 instrument. Samples were prepared at dilute concentrations (below 0.1 OD) and excited in a 1 cm quartz cuvette. After raw data collection of the

emission spectra, the intensity was adjusted using the Horiba calibration file (MCORRECT) to account for detector efficiency.

2.3.5 Two-photon Excited Fluorescence (TPEF) Cross-Section Measurement.

The two-photon cross-section was measured using the TPEF method.[40] A mode-locked 100 fs pulsed TI:Sapphire laser with a repetition rate of 80 MHz was focused onto the sample at 800 nm excitation and the fluorescence was collected by an Acton Instrument SpectraPro 3000 with a Hamamatsu 928 PMT set at 800 V. Input power from the laser was varied using a neutral density filter. Coumarin 307 dissolved in methanol was used as a reference ($\delta\eta_{800}$ = 14.7 GM).[40] Vitamin C was added to all samples at 1 mg/mL to prevent sample degradation under high power laser irradiation. A vitamin C control was run to observe no laser-induced fluorescence.

The equation below, stemming from Equation 15 in Xu et. al[40], gives the relationship between fluorescence and two-photon cross-section of a given molecule,

$$\log[F(t)] = 2\log[\langle P(t)\rangle] + \log\left[\frac{1}{2}\eta\delta[c]n \cdot \frac{g_p}{\pi\lambda f c}\right] \quad (2.1a)$$

where F(t) is the two-photon fluorescence, P(t) is the excitation power, n is the refractive index of the solvent used, [c] is the concentration of the molecule (M), η is quantum yield of the molecule, δ is the two-photon cross-section of the molecule, λ is the laser wavelength, and g_p 'second order temporal coherence', f 'rep rate', and t 'FWHM' are laser parameters which are experimentally constant during collection.

The above formula is written in the y = mx + b form and applied in the TPEF method via a ratiometric comparison between a known two-photon dye and the sample. Hence, the two-photon cross-section is calculated using Equation 2.1b, where δ is the two-photon cross-section, b is the y-intercept of log[Fluorescence]-log[power] plot, η is the quantum yield, n the refractive index, and [c] the concentration,

$$\eta_{sample}\delta_{sample} = \frac{10^{b_{sample}-b_{std}}\eta_{std}\delta_{std}[c]_{std}n_{std}}{[c]_{sample}n_{sample}} \quad (2.1b)$$

The y-intercept is found by measuring the two-photon fluorescence at multiple powers of excitation, and plotting log[Fluorescence] vs. log[Power]. As equations 2.1a and 2.1b reveal, larger y-intercepts will result in larger cross-sections; for molecules with large two-photon cross-sections, we expect the y-intercept (b) to be non-zero.

2.3.6 Singlet Oxygen Detection via SOSG.

Singlet oxygen sensor green (SOSG) was used to measure the singlet oxygen production of $Au_{25}(Capt)_{18}$, PAAm-$Au_{25}(Capt)_{18}$, and TMPYP (5,10,15,20-Tetrakis(1-methyl-4-pyridinio) porphyrin tetra(p-toluenesulfonate)). TMPYP was chosen for comparison to Au_{25} as it is a popular photosensitizer, with two-photon properties.[41–44] Rose Bengal (RB) was used as a standard, with singlet oxygen efficiency of 0.75 at 549 nm excitation in PBS.[45] All samples were adjusted to have the same optical density (OD = 0.093) in 1 mL PBS solution, measured via UV-Vis on a UV-2600 from Shimadzu Scientific Instruments, Inc. For each sample of identical OD that was prepared, 6 µM of SOSG (20 µL of 0.3 mM stock) was added to the cuvette and stirred for 5 minutes. Next, the samples brought to the fluorimeter (Horiba Fluoromax 4c). Photosensitizers were excited on the fluorometer in 10 minute intervals of 10, 20, 30, and 40 minutes (total excitation time) using 5 nm excitation slit and 1 nm emission slit. Rose Bengal (RB) was excited at 549 nm, and PAAM-$Au_{25}(Capt)_{18}$, $Au_{25}(Capt)_{18}$, and TMPYP samples were excited at 400 nm. PBS controls were additionally prepared, excited at 400 nm and 549 nm respectively, to reveal that SOSG had no sensitivity to either wavelength without photosensitizer. Before each excitation, SOSG fluorescence (504 nm excitation; 520 – 600 nm emission) was collected with 1 nm excitation and emission slits with an integration time of 0.1 seconds. As singlet oxygen is produced, SOSG will increase in fluorescence.[46,47] To calculate the singlet oxygen efficiency of each photosensitizer, the fluorescence increase of SOSG at 530 nm was plotted over time for each sample, and Equation 2.2 was used to calculate efficiency, where ϕ is

the singlet oxygen efficiency of the sample and slope is the slope of SOSG vs. time, assuming equivalent absorbance.

$$\varphi_{sample} = \frac{slope_{sample}}{slope_{ref}} \varphi_{ref} \quad (2.2)^{48}$$

2.3.7 Inductively Coupled Plasma Mass Spectrometry (ICP-MS) Experiments.

Determining Mass Loading of $Au_{25}(Capt)_{18}$ in PAAm-$Au_{25}Capt_{18}$

ICP-MS was run using a Perkin Elmer Nexion 2000. A gold standard (Au 197) was prepared at 1, 2, 3, 4, and 5 ppb in Milli-Q water with bismuth (Bi 209) as an internal standard. The PAAm-$Au_{25}(Capt)_{18}$ was prepared at 100 ppb (100 ng/mL) to determine the amount of Au present. ICP runs were averaged over 3 trials. The counts of all samples were adjusted based on the Bi 209 standard, then a linear fit was determined from the known Au standards (y-intercept fixed at 0) to calculate the $Au_{25}(Capt)_{18}$ mass in PAAm-$Au_{25}(Capt)_{18}$.

Determining HeLa Cell Uptake Efficiency of $Au_{25}Capt_{18}$ and PAAm-$Au_{25}Capt_{18}$

100,000 Hela cells were plated two days before experiment. 24 hours before experiment, media was removed, cells were washed with 1 mL DPBS, and $Au_{25}Capt_{18}$ (0.1 mg/ml, 0.05 mg/ml, 0.025 mg/ml, 0.0125 mg/ml, 0.00625 mg/ml) and PAAm- $Au_{25}Capt_{18}$ (2 mg/ml, 1 mg/ml, 0.5 mg/ml, 0.25mg/ml, 0.125mg) were added to cell plates in 1 mL DMEM (10% FBS, 1% PS, 1% AA) media. The next day, plates were washed 2 times using DPBS, and 1 mL of 1% trypsin was added to each plate. Next, all samples were diluted (250 uL sample in 10 mL PBS). Cell samples incubated with high Au concentrations, namely $Au_{25}Capt_{18}$ (0.1 mg/ml, 0.05 mg/ml) and PAAM-$Au_{25}Capt_{18}$ (2 mg/ml, 1 mg/ml), were additionally diluted (500 mL of first diluted solution in 2 mL PBS). All samples were then analyzed on the Perkin Elmer Nexion 2000 instrument. For calibration, 7.5, 15, 20, 30, 50 and 70 ppb standards were used.

2.3.8 HeLa Biocompatibility Measurements.

The MTT (3-(4,5-dimethylthiazol-2-yl)-2,5-diphenyltetrazolium bromide) assay is employed as a way of measuring whether any stress is placed on the cells by being in the presence of the NPs.[49] Using a 96 well plate, 5,000 HeLa cancer cells were plated in each well in 100 µL of DMEM media. The cells were incubated for 24 hours to ensure adhesion to the plate. The nanoparticles were then added to 5 wells at concentrations of 0.1, 0.3, 0.5, 1.0, 2.0, 5.0, and 10.0 mg/mL, and volumes were brought to 200 µL for all wells. A control sample was made without any nanoparticle treatment. After 24 more hours of incubation, 20 µL of a 0.5 mg/mL solution of MTT dye in PBS was added to each well. After 3 hours, the media was removed and replaced with 200 µL of DMSO. The plate was transferred to an Anthos 2010 plate reader and scanned at 540 nm excitation.

To calculate the viability, the raw data for each nanoparticle concentration was averaged (n=5) to reduce random error. Percent viability was normalized by dividing the average values for each nanoparticle concentration by the control average value. Error bars were determined from the standard deviation of the 5 wells for each sample.

2.3.9 Two-photon photodynamic therapy and imaging microscopy.

HeLa cells were plated at 150,000 cells/plate 2 days before the experiment. For non-controls, PAAm-Au_{25} NPs were incubated at 0.5, 1.0, and 3.0 mg/mL one day before the confocal experiment. 24 hours later, media was aspirated and plates were washed with DPBS buffer. Next, 1 mL of DMEM media was added to all plates. 2.5 µl Calcein AM from a 50 µg/50 µL DMSO solution was added to the plate (2.5 µL/1 mL of media). After 30 minutes incubation, the plate was washed 3 times with DPBS media. Next, 1 mL of DMEM media was added to the plate and 20 µL of Propidium Iodide (PI) at 1 mg/mL was added (20 µL PI/1 mL media).

Two-photon photodynamic therapy was performed using a SpectraPhysics Ti:Sapphire laser with a 100 fs pulse width and a 80 MHz repetition rate at 100 mW/cm^2, under 5 minute and 15 minute excitation, focused onto the sample using a 10x objective (Figure S1). Non-pulsed controls (one-photon) were performed for all samples. Microscopy images were taken using Calcein AM (ex_{max} 495/em_{max} 515) and Propidium Iodide (ex_{max} 535/em_{max} 617) filters in the excited region. After photodynamic illumination, Calcein AM and Propidium Iodide fluorescence was taken in fixed time intervals.

2.4 Results & Discussion

2.4.1 Synthesis and one-photon absorption of PAAm-$Au_{25}Capt_{18}$.

$Au_{25}(Capt)_{18}$ has absorption maxima at 456 nm and 678 nm in phosphate-buffered saline (pH 7.4) as shown in Figure 2.2A. Polyacrylamide (PAAm)-$Au_{25}Capt_{18}$ embedded nanoclusters were synthesized using a reverse-micelle method.[14] As shown in Figure 2.2A, both 456 and 678 nm peaks are present, confirming cluster integrity. The reduction in the peaks may be due to the external PAAm environment, as surrounding ligand has been shown to strongly influence Au_{25} absorbance.[50] Furthermore, as we show later in this manuscript, the two-photon absorption cross-section and singlet oxygen efficiency of the $Au_{25}Capt_{18}$ is preserved when embedded in PAAm, of importance for 2p-PDT.

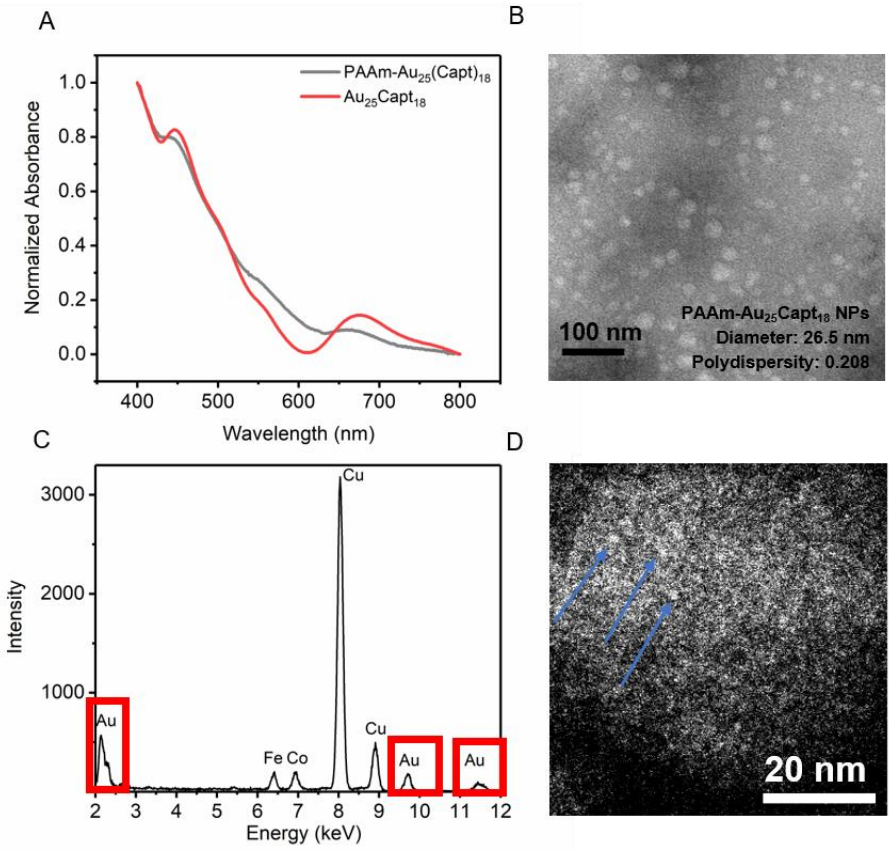

Figure 2.3 A.) UV-Vis spectra of $Au_{25}(Capt)_{18}$ nanoclusters and PAAm-$Au_{25}(Capt)_{18}$ embedded nanoparticles. B.) Transmission electron microscopy image of PAAm-$Au_{25}Capt_{18}$ NPs. C.) Energy dispersive X-Ray spectroscopy peaks of PAAm-$Au_{25}Capt_{18}$ deposited on a copper TEM grid. D.) High-resolution transmission electron microscopy image of polyacrylamide (PAAm) particle revealing encapsulated $Au_{25}Capt_{18}$ clusters (blue arrows point to $Au_{25}Capt_{18}$ NCs speckled in NP).

Using dynamic light scattering, the average diameter of the polyacrylamide particles was found to be 26.5 nm and the polydispersity index (PDI) was 0.208, where PDI is defined by $(STDEV_{diameter}{}^2/(\text{mean diameter})^2)$.[51] The PAAm PDI falls into the range of previously reported particles, and its PDI is below the 0.3 limit defined for monodisperse nano pharmaceuticals.[51–53] The size of PAAm particles is confirmed by transmission electron microscopy (TEM), as shown in Figure 2.2B. Additionally, energy dispersive X-Ray spectroscopy (EDS) peaks, at 2.1, 9.6, and 11.5 keV, confirm the presence of Au

embedded in PAAm (Figure 2.2C). Within the EDS spectra, copper is also identified due to the use of a copper TEM grid and iron and cobalt due to the TEM lens. Using high-resolution transmission electron microscopy, the Au clusters are further visualized (Figure 2.2D, blue arrows). Based on the per mass absorption difference between non-loaded and loaded PAAm-$Au_{25}(Capt)_{18}$, the $Au_{25}(Capt)_{18}$ NC is about 5% by mass of the total PAAm particle. Using inductively-coupled plasma mass spectrometry (ICP-MS), the $Au_{25}(Capt)_{18}$ loading was measured at 4.2% M/M% in PAAm, confirming the UV-Vis results (Figure 2.3).

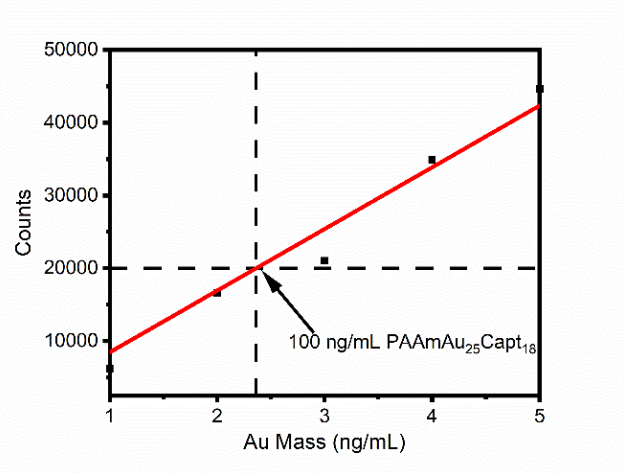

Figure 2.4 ICP Results of PAAm-$Au_{25}(Capt)_{18}$ at 100 ng/mL calibrated against 1-5 ng/mL Au standards (R^2 =0.990).

2.4.2 Two-photon cross-section and singlet oxygen efficiency of PAAm-$Au_{25}(Capt)_{18}$.

As mentioned previously, the absorption and singlet oxygen efficiency determine the molecular efficacy of photosensitizers.[15] While Au_{25} clusters have weak one-photon absorption at 800 nm, Au_{25} clusters are reported to have high two-photon absorption cross-sections at 800 nm.[14,52,53] To measure the two-photon cross-section of nonlinear materials, the Z-scan method or TPEF (two-photon excited fluorescence) methods are most commonly used.[52] However, since $Au_{25}Capt_{18}$ has both linear and non-linear absorbance at 800 nm, a deconvolution must be performed to determine the cross-section with the Z-scan method.[52] On the other hand, to determine the cross-section of Au_{25} clusters by the TPEF

method, the fluorescence intensity in the range of 450 – 550 nm can be utilized (Figure 2.4A), as this fluorescence is purely two-photon in origin.[14,53] Although *$Au_{25}(Capt)_{18}$* has a strong infrared emission, this emission is also one-photon when excited with 800 nm light, attributed to intraband excitation, as discussed by Yi et. al.[54] Figure 2.4B shows the log-log power dependence of the PAAm-*$Au_{25}(Capt)_{18}$* clusters at the 510 nm emission peak. The log-log power dependence of PAAm-*$Au_{25}(Capt)_{18}$* clusters has an averaged slope of 2.05 ± 0.035, indicating a fluorescence originating from purely two-photon absorption (expected slope 2).

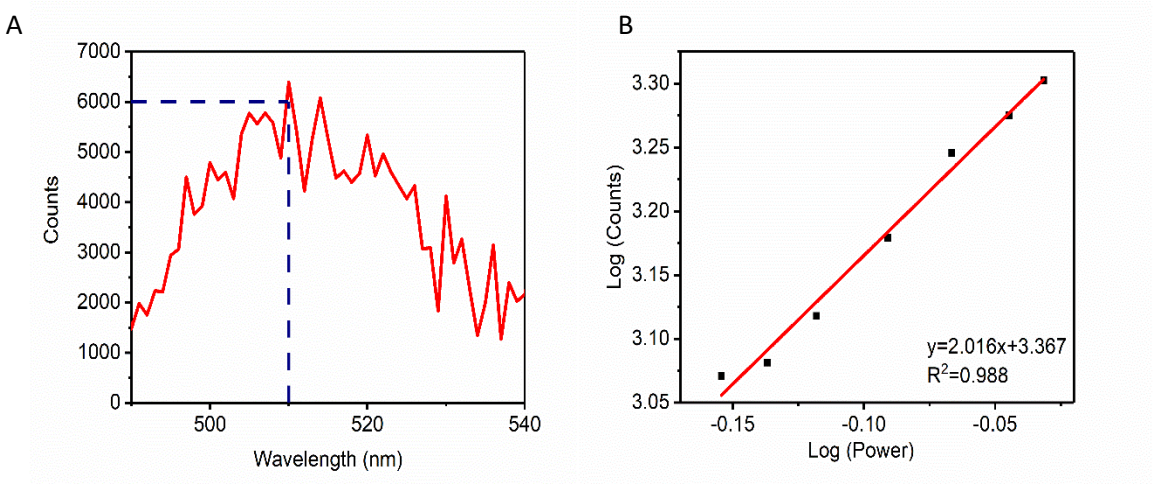

Figure 2.5 A.) Two-photon fluorescence from PAAm-$Au_{25}(Capt)_{18}$ from 800 nm pulsed excitation. B.) Two-photon log[Fluorescence]-log[Power] plot from PAAm-$Au_{25}(Capt)_{18}$ at 510 nm emission. The two-photon cross-section derived from the y-intercept was averaged over 3 experiments.

Using the TPEF method, a large y-intercept means the two-photon cross-section is large.[40] Thus, the y-intercept of 3.3 (Figure 2.4B) indicates that substantial two-photon absorption is taking place. All trials of the power-dependent two-photon fluorescence via TPEF were provided in the Supplementary Materials for $Au_{25}(Capt)_{18}$ and PAAM-$Au_{25}(Capt)_{18}$ (McLean, Kopelman et. al.). Using the TPEF method, the cross-section obtained ("action cross-section") is a product of the fluorescence quantum yield (visible regime) and the two-photon absorbance cross-section. We determine the action two-photon cross-section of Au_{25} and PAAm-Au_{25} to be $3.85 \times 10^{-2} \pm 1.35 \times 10^{-2}$ GM and $4.97 \times 10^{-2} \pm 2.20 \times 10^{-2}$ GM

respectively (Table 1). Due to the ultra-low quantum yield of Au_{25} clusters in the visible regime, the quantum yield cannot be directly measured, and an absolute two-photon cross-section can only be determined by ultrafast techniques,[16] or by taking the ratio of the TPEF cross-section to the action cross-section from the Z-scan method.[26] The deconvoluted two-photon cross-section of $Au_{25}Capt_{18}$ clusters has recently been reported via Z-scan by Olesik-Banska et. al. to be 830 GM,[52] suggesting the quantum yield of $Au_{25}Capt_{18}$ clusters is about 2 x 10^{-5}. This quantum yield is reasonable when compared to quantum yield values (~10^{-7}) of other Au_{25} clusters determined in the literature, as captopril clusters are more fluorescent.[14,24,55]

Singlet oxygen efficiency was determined for both Au_{25} and PAAm-Au_{25} using singlet oxygen sensor green (SOSG) with Rose Bengal (RB) as a standard (Figure 2.5). TMPYP, a common two-photon photosensitizer with a cross-section of 116 GM[56], was also tested to compare to Au_{25} and PAAm-Au_{25} embedded clusters.

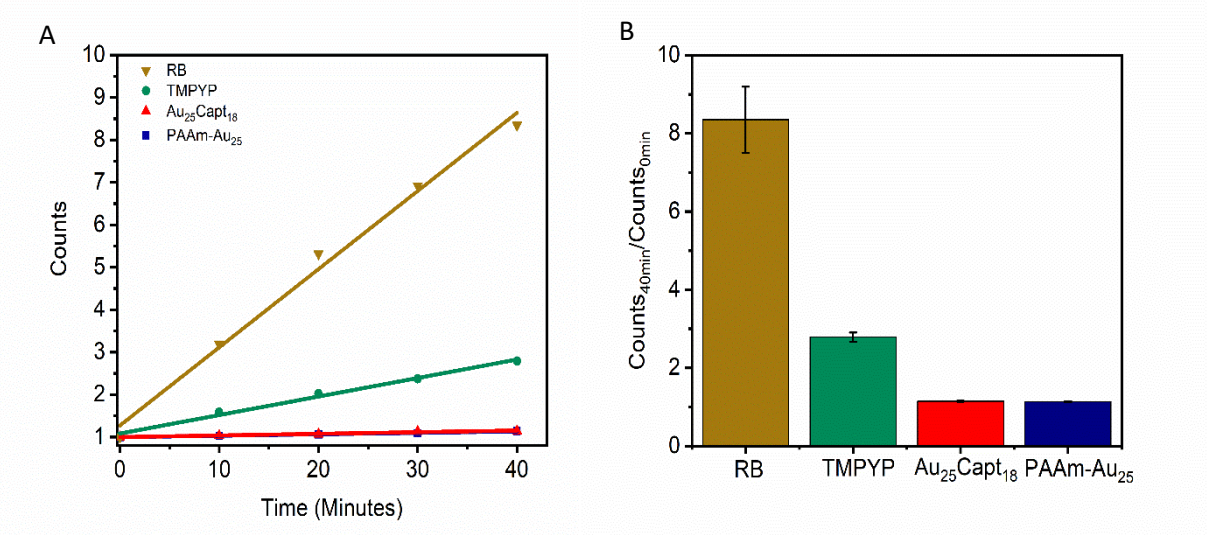

Figure 2.6 A.) Normalized SOSG fluorescence intensity (F_t/F_0), 0 to 40 minutes after continuous Rose Bengal (RB), TMPYP, $Au_{25}Capt_{18}$, and PAAm-$Au_{25}Capt_{18}$ excitation at identical optical densities. $Au_{25}Capt_{18}$ and PAAm-$Au_{25}Capt_{18}$ points nearly coincide. B.) Ratio of SOSG fluorescence intensity (40 min/0 min) from excitation of Rose Bengal (RB), TMPYP, $Au_{25}Capt_{18}$, and PAAm-$Au_{25}Capt_{18}$ to determine singlet oxygen quantum yield.

We determine that the singlet oxygen efficiency of TMPyP, $Au_{25}Capt_{18}$, and $Au_{25}Capt_{18}$-PAAm is 18.2%, 1.6%, and 1.4%, respectively. A summary of the two-photon cross-sections and singlet oxygen efficiencies of TMPYP, Au_{25}, and PAAm-Au_{25} is provided in Table 2.1.

Table 2.1 Two-photon absorption cross-section and singlet oxygen quantum efficiency (σ_{O2}) of TMPYP, $Au_{25}Capt_{18}$, and PAAm-$Au_{25}Capt_{18}$.[a]

Compound	Two-photon absorption cross-section (GM)	Singlet oxygen efficiency (%)
TMPYP	116 ± 21 (ref 56)	18.2
$Au_{25}Capt_{18}$	830 (ref 52), $3.85 \times 10^{-2} \pm 1.35 \times 10^{-2}$ (δn)	1.6
PAAm-$Au_{25}Capt_{18}$	$4.97 \times 10^{-2} \pm 2.20 \times 10^{-2}$ (δn)	1.4

[a]For $Au_{25}(Capt)_{18}$ and PAAm-$Au_{25}(Capt)_{18}$ the two-photon absorption is a product of the two-photon cross section and quantum yield due to the TPEF method used (δn).

The high singlet oxygen efficiency of RB (75%) and TMPYP (18.2%) are due to their long aqueous phosphorescent lifetimes (150 ms and 0.2 ms).[57,58] On the other hand, the excited state lifetime of Au_{25} has been measured on the order of microseconds.[59-61] While TMPYP has a significantly higher singlet oxygen quantum efficiency than Au_{25} (18x), Au_{25} has a two-photon cross-section that is 8x higher than TMPYP. Due to the non-linear nature of two-photon absorption, as the power is increased, significantly more photons will be absorbed, drastically improving two-photon PDT efficacy. Furthermore, synthetic strategies to increase the singlet oxygen efficiency of an Au_{25} photosensitizer should be explored in the future, for example, through charge-transfer to another chromophore.[61,62] Lastly, Au_{25} has another functionality as an X-ray (CT) contrast agent, a theranostic functionality that TMPYP, and organic photosensitizers, do not possess.

2.4.3 Dark biocompatibility of Au_{25} and PAAm-Au_{25} embedded nanoparticles and their in vitro loading efficiencies.

To provide evidence for therapeutic PDT usefulness, it is important to ensure that therapeutic agents do not cause significant stress to the cells without illumination. The dark biocompatibility of Au_{25} clusters is still open to question in the literature, with varying results.[28, 63-67] We tested the viability of HeLa 229 cancer cells in the presence of 0.1 mg/mL through 10 mg/mL $Au_{25}Capt_{18}$ clusters incubated in the dark under 24 hour incubation. Even at 0.1 mg/mL, we found that cells have approximately 50% viability. At 2 mg/mL, less than 5% of cells are viable. On the other hand, PAAm-Au_{25} particles have greater than 85% viability at concentrations as high as 10 mg/mL NP, as shown in Figure 2.6B. We did not provide toxicity experiments for Au NCs stored in daylight, but this is an important precaution to take when handling the NC. In fact, Kauffmann et. al. show that storing Au NCs under light will produce O_2 mediated chemistry, however storing Au NCs under dark conditions will not lead to chemistry between Au_{25} and O_2.[68]

Overall, when comparing biocompatibility of PAAm-Au_{25} and non-encapsulated Au_{25} at equal effective masses of Au (5% loading), PAAm-encapsulated clusters provide a clear and substantial enhancement to viability, as shown in Figure 2.6C. The increased biocompatibility of PAAm-$Au_{25}Capt_{18}$ NPs is a major advantage of the polyacrylamide encapsulation.

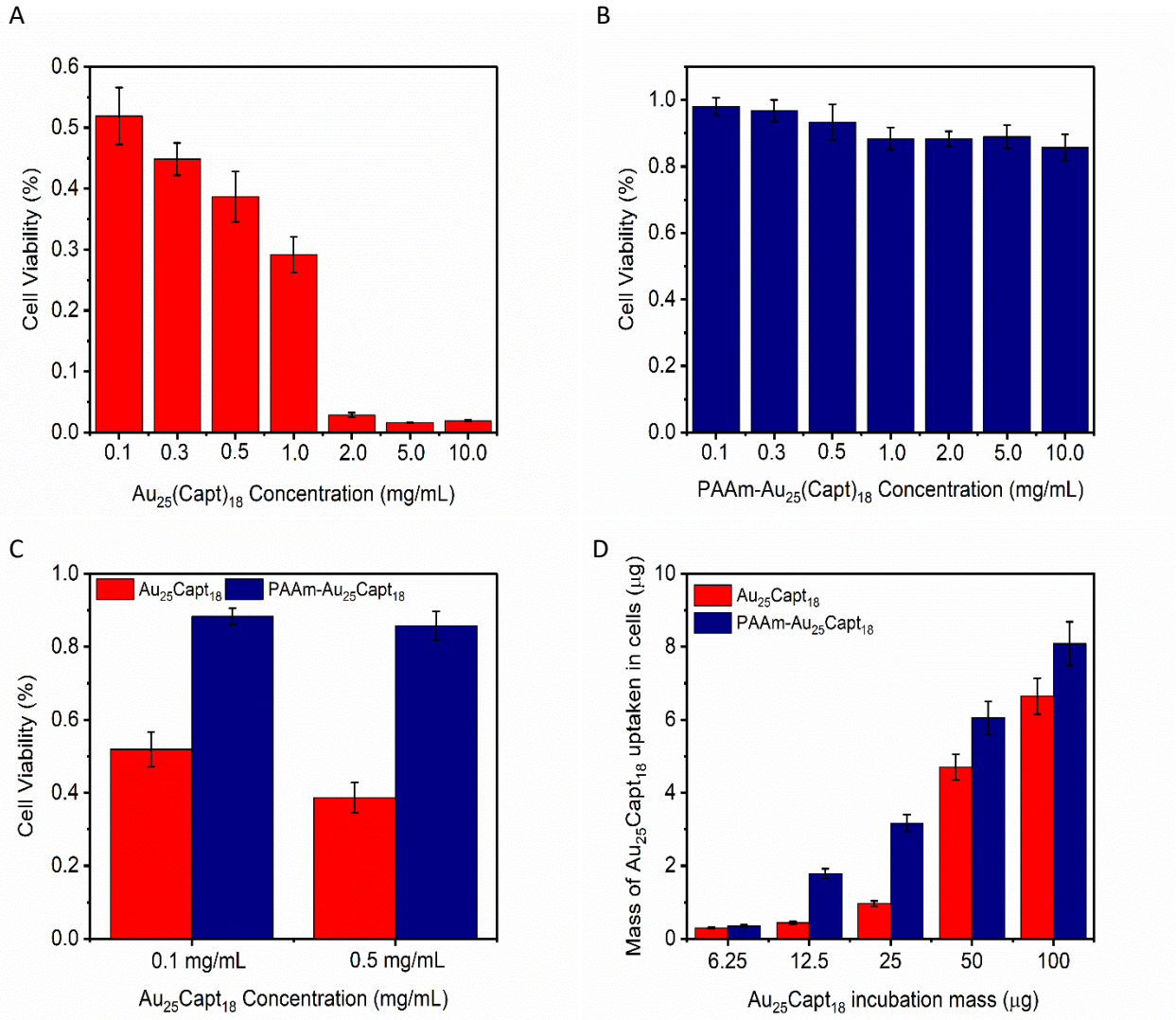

Figure 2.7 A.) Cell viability under dark incubation with $Au_{25}Capt_{18}$ clusters, from 0.1 – 10 mg/mL, B.) Cell viability under dark incubation with PAAm-$Au_{25}Capt_{18}$ NPs from 0.1 – 10 mg/mL, C.) Cell viability comparison of $Au_{25}Capt_{18}$ cluster and PAAm-$Au_{25}Capt_{18}$ NPs at equivalent $Au_{25}Capt_{18}$ dark incubation masses, D.) Mass of $Au_{25}Capt_{18}$ detected via ICP in cells for Au_{25} and PAAm-$Au_{25}Capt_{18}$ with $Au_{25}Capt_{18}$ cluster incubation masses of 6.25 – 100 ug in 1 mL of media.

Due to reports that Au_{25} can have low cell uptake of Au_{25} clusters,[30] we compared the cell uptake of $Au_{25}Capt_{18}$ clusters and PAAm-Au_{25} via inductively-coupled plasma mass spectrometry (ICP-MS). Overall, we find that PAAm-Au_{25} particles have higher *in vitro* loading (10.6 ± 3.5%) per effective gold cluster compared to $Au_{25}Capt_{18}$ (5.6 ± 2.4%), as shown in Figure 2.6D. While not explored in this

manuscript, this increase can be further accentuated for particular tumor types, as PAAm particles have been shown capable of conjugation with cell surface targeting moieties to enhance uptake.[69,70]

2.4.4 Non-linear Optical PDT Efficacy.

For an accurate evaluation of non-linear optical PDT effects, cells were illuminated using 800 nm pulsed light at 100 mW/cm^2 over 15 minute (Figure 2.7) and 5 minute excitations (Figure 2.8). The illumination time and power were chosen based on comparable excitation times and powers from the previous two-photon *in vitro* PDT literature.[71-73] Calcein AM, a fluorescent dye that marks cell viability, and frequently employed to study two-photon PDT, was added to all cells.[71,74-76] The Calcein AM signal will be diminished as cell membranes rupture or their metabolism is affected, and can be used in conjunction with Propidium Iodide (PI) tests to show cell death.[71,75,76]

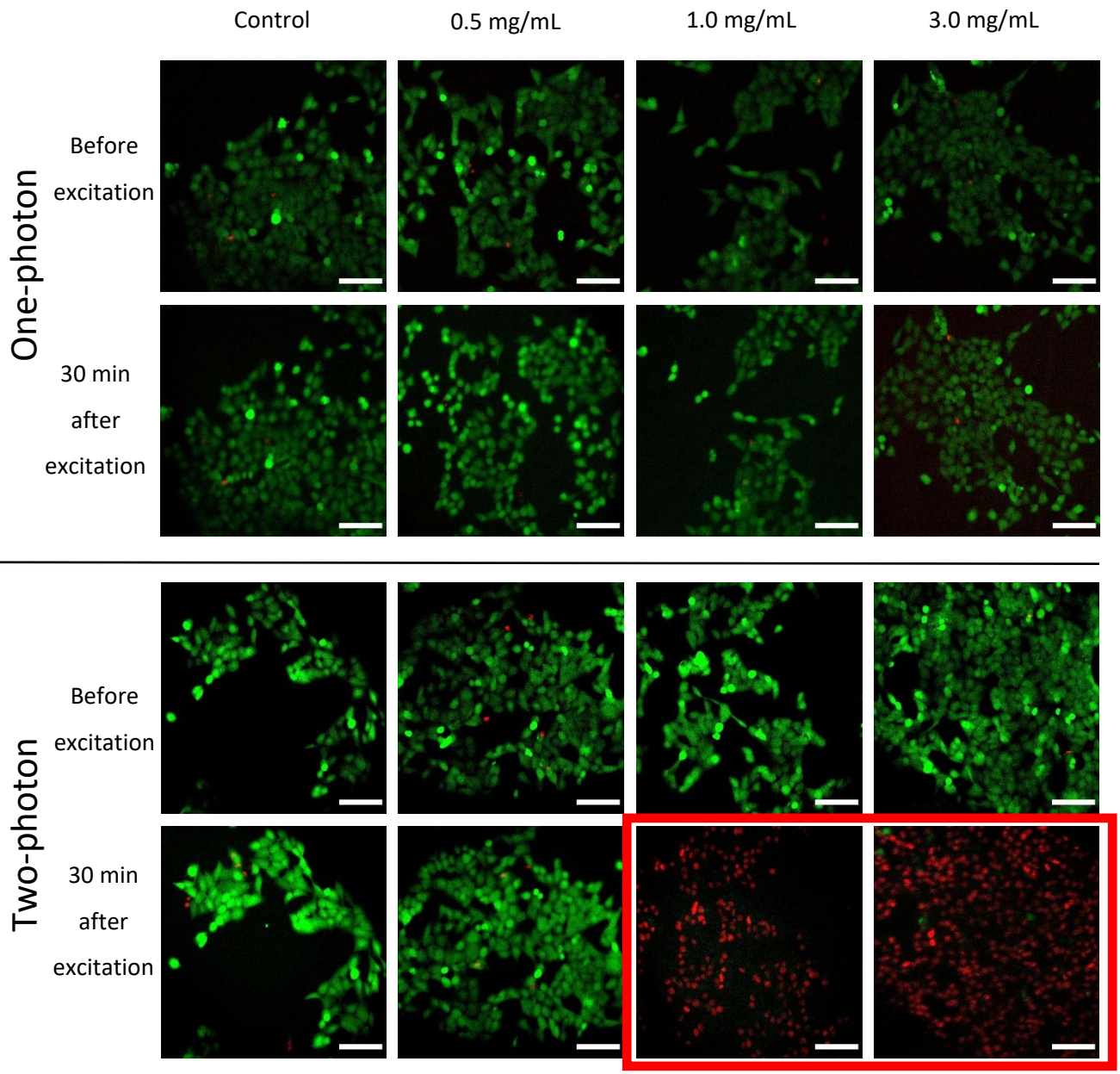

Figure 2.8 PDT images of HeLa cells with control (no NP), 0.5 mg/mL, 1.0 mg/mL and 3.0 mg/mL incubated PAAm-Au_{25}Capt/cm^2 under 800 nm one-photon (non-pulsed) and two-photon illumination (pulsed), 15 minute excitation at 100 mW/cm^2 (average power). Samples were co-stained with Calcein AM and Propidium Iodide (PI) to mark cell viability. Scale bar is 20 µm.

Control HeLa cells, before and after laser illumination, showed no Calcein AM fluorescence change and no PI fluorescence, i.e., no statistically significant cell death after 30 minutes of excitation. Similarly,

PAAm-$Au_{25}Capt_{18}$ incubated cells excited with one-photon excitation show no evidence of PDT-mediated cell death 30 minutes after excitation. However, HeLa cells excited under two-photon illumination at 800 nm with 1.0 mg/mL and 3.0 mg/mL incubated PAAm-$Au_{25}Capt_{18}$ show remarkable cell death efficacy: 30 minutes after excitation, >99% of cells in the region are dead, as indicated by the loss of Calcein AM fluorescence and the presence of PI fluorescence. The cell death observed in the presence of NPs and light must most probably be PDT mediated. While we cannot exclude the possibility that part of the cell kill effect was via two-photon photo-thermal therapy (PTT), PTT has been shown to cause Au_{25}-mediated cell death only at powers above 7.5 W/cm^2 (4 minute) and with high effective Au concentrations (0.75 mg/mL).[77] In contrast, by here only using 100 mW/cm^2 excitation and a maximum effective Au_{25} concentration of 0.15 mg/mL, the conditions to induce PTT were not met in this study. To summarize, with one-photon excitation, only <1% of the cells show PDT-mediated cell death, as propidium iodide indicates. In contrast, under two-photon excitation, >99% of cells show such PDT-mediated cell death. These results point to the substantial benefits of using two-photon PDT.

We also evaluated two-photon photodynamic therapy using 5 minute excitation at 800 nm, with 100 mW/cm^2 (Figure 2.8). Overall, PAAm-Au_{25} concentration-dependent cell death was similar to the 15 minute trials (Figure 2.7), with most effective death occurring under two-photon PDT at 3 mg/mL NP incubation.

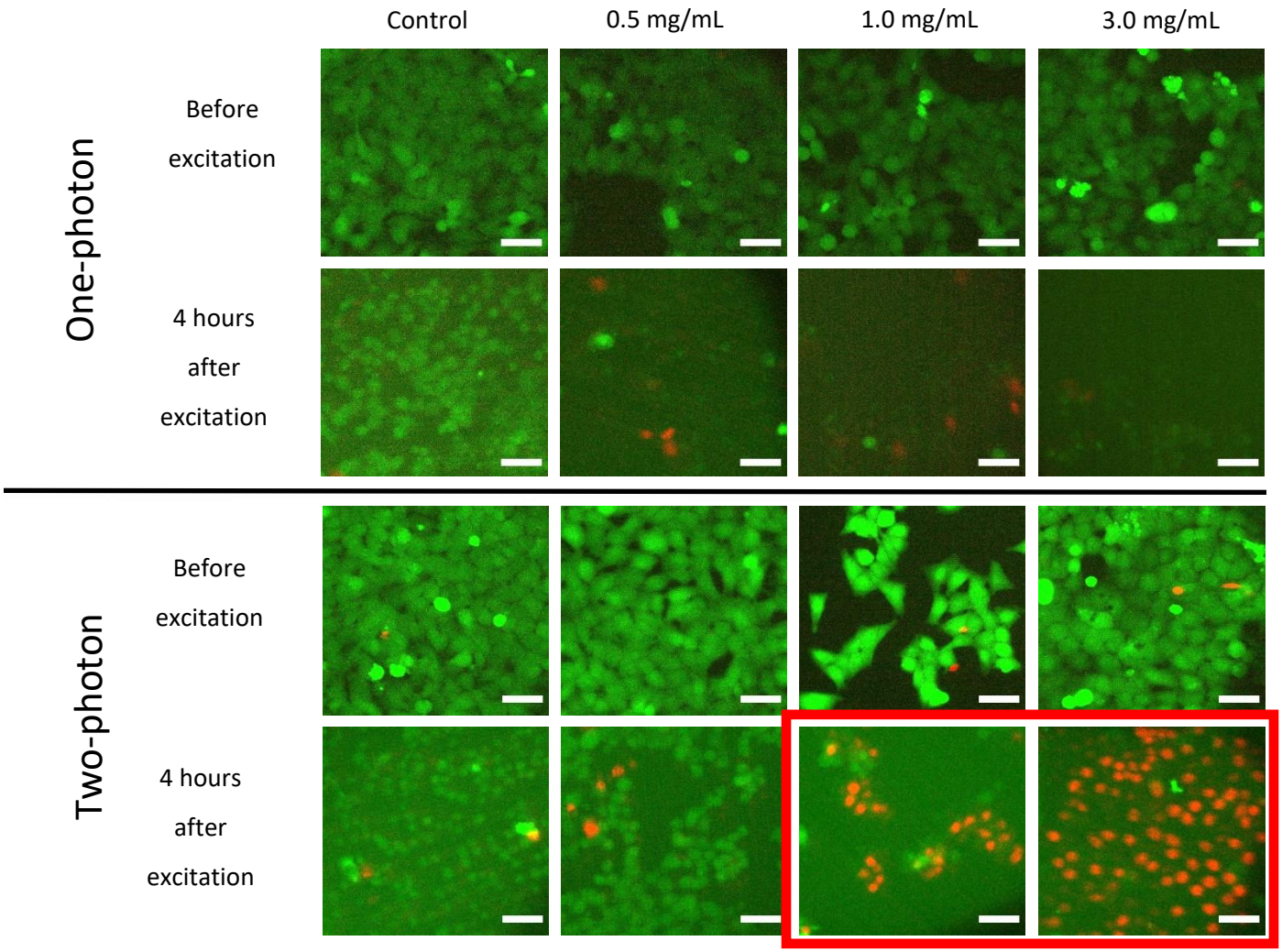

Figure 2.9 PDT images of HeLa cells with control (no NP), 0.5 mg/mL, 1.0 mg/mL and 3.0 mg/mL incubated PAAm-Au_{25}Capt/cm^2 under 800 nm one-photon (non-pulsed) and two-photon (pulsed) illumination, 5 minute excitation at 100 mW/cm^2 (average power). Samples were co-stained with Calcein AM and Propidium Iodide to mark cell viability. Scale bar is 10 µm.

We note that the same NPs could also serve as a contrast agent for CT of soft tumors, as gold compounds do enhance scattering by X-rays, with ample literature examples.[78,79] For future in-vivo research, targeted PAAm-$Au_{25}Capt_{18}$ gold cluster-based nanoparticles should be investigated for theranostic application, with combined CT imaging and 2p-PDT.

2.5 Conclusions

In summary, our work produces and characterizes the PAAm-Au_{25}(Captopril)$_{18}$ nanocluster and its embedded hydrogel nanoparticles, utilizing them for two-photon photodynamic therapy applications. These PAAm-Au_{25} NPs also show (1) highly enhanced cell biocompatibility and (2) greater cell uptake, compared to the unembedded cluster. Furthermore, we have demonstrated highly efficacious *in vitro* two-photon PDT using those PAAm-$Au_{25}Capt_{18}$ NPs, demonstrating a tremendous enhancement in this 2p-PDT-mediated cell death over one-photon PDT. We associate this enhancement with the high non-linear cross-sections of the Au_{25} clusters. This new 2-photon photodynamic agent, the Au_{25} cluster, (a) has a two-photon cross-section 8x bigger compared to TMPYP, a highly used two-photon photosensitizer, (b) has an activity rising quadratically with increased photon power, (c) offers the opportunity for improvement with chemical synthesis stratagems and (d) is also a potential theranostic agent enabling improved CT imaging. Furthermore, when embedded in hydrogel NPs it gives both better biocompatibility and potential tumor targeting.

In future research, one goal should be to improve the reactive oxygen production efficiency of the Au_{25} clusters, possibly via charge-transfer to an acceptor chromophore, as well as to explore targeted PAAm-$Au_{25}Capt_{18}$ for dual 2p-PDT and CT theranostic applications. Overall, due to their high non-linear cross-sections, Au_{25} clusters, especially with encapsulation in PAAm NPs, present an attractive nanosystem for non-linear photodynamic therapy and may have a promising potential for *in vivo* therapy.

2.6 References

(1) Zhang, Y.; Zhang, C.; Xu, C.; Wang, X.; Liu, C.; Waterhouse, G. I. N.; Wang, Y.; Yin, H. Ultrasmall Au Nanoclusters for Biomedical and Biosensing Applications: A Mini-Review. *Talanta* **2019**, 200, 432–442. https://doi.org/10.1016/j.talanta.2019.03.068.

(2) Zheng, K.; Setyawati, M. I.; Leong, D. T.; Xie, J. Antimicrobial Gold Nanoclusters. *ACS Nano* **2017**, 11 (7), 6904–6910. https://doi.org/10.1021/acsnano.7b02035.

(3) Yang, J.; Wang, F.; Yuan, H.; Zhang, L.; Jiang, Y.; Zhang, X.; Liu, C.; Chai, L.; Li, H.; Stenzel, M. Recent Advances in Ultra-Small Fluorescent Au Nanoclusters toward Oncological Research. *Nanoscale* **2019**. https://doi.org/10.1039/c9nr04301b.

(4) Palmal, S.; Jana, N. R. Gold Nanoclusters with Enhanced Tunable Fluorescence as Bioimaging Probes. *Wiley Interdiscip. Rev. Nanomedicine Nanobiotechnology* **2014**, 6 (1), 102–110. https://doi.org/10.1002/wnan.1245.

(5) Li, G.; Jin, R. Atomically Precise Gold Nanoclusters as New Model Catalysts. *Acc. Chem. Res.* **2013**, 46 (8), 1749–1758. https://doi.org/10.1021/ar300213z.

(6) Li, G.; Abroshan, H.; Chen, Y.; Jin, R.; Kim, H. J. Experimental and Mechanistic Understanding of Aldehyde Hydrogenation Using Au_{25} Nanoclusters with Lewis Acids: Unique Sites for Catalytic Reactions. *J. Am. Chem. Soc.* **2015**, 137 (45), 14295–14304. https://doi.org/10.1021/jacs.5b07716.

(7) Li, G.; Abroshan, H.; Liu, C.; Zhuo, S.; Li, Z.; Xie, Y.; Kim, H. J.; Rosi, N. L.; Jin, R. Tailoring the Electronic and Catalytic Properties of Au25 Nanoclusters via Ligand Engineering. *ACS Nano* **2016**, 10 (8), 7998–8005. https://doi.org/10.1021/acsnano.6b03964.

(8) Chen, Y. S.; Choi, H.; Kamat, P. V. Metal-Cluster-Sensitized Solar Cells. A New Class of Thiolated Gold Sensitizers Delivering Efficiency Greater than 2%. *J. Am. Chem. Soc.* **2013**, 135 (24), 8822–8825. https://doi.org/10.1021/ja403807f.

(9) Choi, H.; Chen, Y. S.; Stamplecoskie, K. G.; Kamat, P. V. Boosting the Photovoltage of Dye-Sensitized Solar Cells with Thiolated Gold Nanoclusters. *J. Phys. Chem. Lett.* **2015**, 6 (1), 217–223. https://doi.org/10.1021/jz502485w.

(10) Dolman, D.; Fukumura, D.; Jain, R. Photodynamic Therapy for Cancer. *Nat. Rev. Cancer* **2003**, 3 (5), 380–387.

(11) Yoon, I.; Li, J. Z.; Shim, Y. K. Advance in Photosensitizers and Light Delivery for Photodynamic Therapy. *Clin. Endosc.* **2013**, 46 (1), 7–23. https://doi.org/10.5946/ce.2013.46.1.7.

(12) Lucky, S. S.; Soo, K. C.; Zhang, Y. Nanoparticles in Photodynamic Therapy. *Chem. Rev.* **2015**, 115 (4), 1990–2042. https://doi.org/10.1021/cr5004198.

(13) Agostinis, P; Berg, K; Cengel, K; Foster, TH; Girotti, AW; Gollnick, SO; Hahn, SM; Hamblin, MR; Juzenienne, A; Kessel, D; Korbelik, M; Moan, J; Mroz, P; Nowis, D; Piette, J; Wilson, BC; Golab, J. Photodynamic therapy of cancer: An Update. *Ca Cancer J. Clin.* **2017**, 61, 250–281. https://doi.org/10.3322/caac.20114.

(14) Ramakrishna, G.; Varnavski, O.; Kim, J.; Lee, D.; Goodson, T. Quantum-Sized Gold Clusters as Efficient Two-Photon Absorbers. *J. Am. Chem. Soc.* **2008**, 130 (15), 5032–5033. https://doi.org/10.1021/ja800341v.

(15) Qian, H.; Zhu, M.; Wu, Z.; Jin, R. Quantum Sized Gold Nanoclusters with Atomic Precision. *Acc. Chem. Res.* **2012**, 45 (9), 1470–1479. https://doi.org/10.1021/ar200331z.

(16) Kawasaki, H.; Kumar, S.; Li, G.; Zeng, C. J.; Kauffman, D. R.; Yoshimoto, J.; Iwasaki, Y.; Jin, R. C. Generation of Singlet Oxygen by Photoexcited $Au_{25}(SR)_{(18)}$ Clusters. *Chem. Mater.* **2014**, 26 (9), 2777–2788. https://doi.org/10.1021/cm500260z.

(17) Jacques, S. L. Optical Properties of Biological Tissues: A Review; Corrigendum. *Phys. Med. Biol.* **2013**, 58 (14), R37–R61, 5007–5008. https://doi.org/10.1088/0031-9155/58/14/5007.

(18) Yuan, A.; Wu, J.; Tang, X.; Zhao, L.; Xu, F.; Hu, Y. Application of Near-Infrared Dyes for Tumor Imaging, Photothermal, and Photodynamic Therapies. *J. Pharm. Sci.* **2013**, 102 (1), 6–28. https://doi.org/10.1002/jps.23356.

(19) Link, S.; El-Sayed, M. A.; Schaaff, T. G.; Whetten, R. L. Transition from Nanoparticle to Molecular Behavior: A Femtosecond Transient Absorption Study of a Size-Selected 28 Atom Gold Cluster. *Chem. Phys. Lett.* **2002**, 356 (3–4), 240–246. https://doi.org/10.1016/S0009-2614(02)00306-8.

(20) Rinkevicius, Z.; Ågren, H.; Autschbach, J.; Prasad, P. N.; Baev, A.; Swihart, M. Novel Pathways for Enhancing Nonlinearity of Organics Utilizing Metal Clusters. *J. Phys. Chem. A* **2010**, 114 (28), 7590–7594. https://doi.org/10.1021/jp102438m.

(21) Ho-Wu, R.; Yau, S.-H.; Goodson III, T. Efficient Singlet Oxygen Generation in Metal Nanoclusters for Two-Photon Photodynamic Therapy Applications. *J. Phys. Chem. B* **2017**, 112 (43), 10073-10080. https://doi.org/10.1021/acs.jpcb.7b09442.

(22) Ohta, T.; Shibuta, M.; Tsunoyama, H.; Negishi, Y.; Eguchi, T.; Nakajima, A. Size and Structure Dependence of Electronic States in Thiolate-Protected Gold Nanoclusters of $Au_{25}(SR)_{18}$, $Au_{38}(SR)_{24}$, and $Au_{144}(SR)_{60}$. *J. Phys. Chem. C* **2013**, 117 (7), 3674–3679. https://doi.org/10.1021/jp400785f.

(23) Philip, R.; Chantharasupawong, P.; Qian, H.; Jin, R.; Thomas, J. Evolution of Nonlinear Optical Properties: From Gold Atomic Clusters to Plasmonic Nanocrystals. *Nano Lett.* **2012**, 12 (9), 4661–4667. https://doi.org/10.1021/nl301988v.

(24) Russier-Antoine, I.; Bertorelle, F.; Vojkovic, M.; Rayane, D.; Salmon, E.; Jonin, C.; Dugourd, P.; Antoine, R.; Brevet, P.-F. Non-Linear Optical Properties of Gold Quantum Clusters. The Smaller the Better. *Nanoscale* **2014**, 6 (22), 13572–13578. https://doi.org/10.1039/C4NR03782K.

(25) Kumar, S.; Jin, R. Water-Soluble Au25(Capt)18 Nanoclusters: Synthesis, Thermal Stability, and Optical Properties. *Nanoscale* **2012**, 4 (14), 4222. https://doi.org/10.1039/c2nr30833a.

(26) Kumar, S. Synthesis, Characterization and Application of Water-Soluble Gold and Silver Nanoclusters Synthesis, Characterization and Application of Water-Soluble Gold and Silver Nanoclusters (Thesis). **2013**, 1–111.

(27) Miyata, S; Miyaji, H; Kawasaki, H; Yamamoto, M; Nishida, E; Takita, H; Akasaka, T; Ushijima, N; Iwanaga, T; Sugaya, T. Antimicrobial Photodynamic Activity and Cytocompatibility of Au25(Capt)18 Clusters Photoexcited by Blue LED Light Irradiation. *Int. J. Nanomedicine* **2017**, 12, 2703–2716.

(28) Tay, C. Y.; Yu, Y.; Setyawati, M. I.; Xie, J.; Leong, D. T. Presentation Matters: Identity of Gold Nanocluster Capping Agent Governs Intracellular Uptake and Cell Metabolism. *Nano Res.* **2014**, 7 (6), 805–815. https://doi.org/10.1007/s12274-014-0441-z.

(29) Kuruppuarachchi, M.; Savoie, H.; Lowry, A.; Alonso, C.; Boyle, R. W. Polyacrylamide Nanoparticles as a Delivery System in Photodynamic Therapy. *Mol. Pharm.* **2011**, 8 (3), 920–931. https://doi.org/10.1021/mp200023y.

(30) Wenger, Y.; Schneider, R. J.; Reddy, G. R.; Kopelman, R.; Jolliet, O.; Philbert, M. A. Tissue Distribution and Pharmacokinetics of Stable Polyacrylamide Nanoparticles Following Intravenous Injection in the Rat. *Toxicol. Appl. Pharmacol.* **2011**, 251 (3), 181–190. https://doi.org/10.1016/j.taap.2010.11.017.

(31) Koo, Y. E. L.; Reddy, G. R.; Bhojani, M.; Schneider, R.; Philbert, M. A.; Rehemtulla, A.; Ross, B. D.; Kopelman, R. Brain Cancer Diagnosis and Therapy with Nanoplatforms. *Adv. Drug Deliv. Rev.* **2006**, 58 (14), 1556–1577. https://doi.org/10.1016/j.addr.2006.09.012.

(32) Nakamura, H.; Jun, F.; Maeda, H. Development of Next-Generation Macromolecular Drugs Based on the EPR Effect: Challenges and Pitfalls. *Expert Opin. Drug Deliv.* **2015**, 12 (1), 53–64. https://doi.org/10.1517/17425247.2014.955011.

(33) Drobizhev, M.; Makarov, N. S.; Tillo, S. E.; Hughes, T. E.; Rebane, A. Two-Photon Absorption Properties of Fluorescent Proteins. *Nat. Methods* **2011**, 8 (5), 393–399. https://doi.org/10.1038/nmeth.1596.

(34) McLean, A. M.; Socher, E.; Varnavski, O.; Clark, T. B.; Imperiali, B.; Goodson, T. Two-Photon Fluorescence Spectroscopy and Imaging of 4-Dimethylaminonaphthalimide Peptide and Protein Conjugates. *J. Phys. Chem. B* **2013**, 117 (50), 15935–15942. https://doi.org/10.1021/jp407321g.

(35) Tang, W.; Xu, H.; Park, E. J.; Philbert, M. A.; Kopelman, R. Encapsulation of Methylene Blue in Polyacrylamide Nanoparticle Platforms Protects Its Photodynamic Effectiveness. *Biochem. Biophys. Res. Commun*. **2008**, 369 (2), 579–583. https://doi.org/10.1016/j.bbrc.2008.02.066.

(36) Koo, O. M.; Rubinstein, I.; Onyuksel, H. Role of Nanotechnology in Targeted Drug Delivery and Imaging : A Concise Review. *Nanomedicine: Nanotech, Biology, and Medicine* **2005**, 1, 193–212. https://doi.org/10.1016/j.nano.2005.06.004.

(37) Ray, A.; Mukundan, A.; Xie, Z.; Karamchand, L.; Wang, X.; Kopelman, R. Highly Stable Polymer Coated Nano-Clustered Silver Plates: A Multimodal Optical Contrast Agent for Biomedical Imaging. *Nanotechnology* **2014**, 25 (44), 445104. https://doi.org/10.1088/0957-4484/25/44/445104.

(38) Xu, C.; Webb, W. W. Measurement of Two-Photon Excitation Cross Sections of Molecular Fluorophores with Data from 690 to 1050 Nm. *J. Opt. Soc. Am. B* **1996**, 13 (3), 481. https://doi.org/10.1364/JOSAB.13.000481.

(39) Gao, D.; Agayan, R. R.; Xu, H.; Philbert, M. A.; Kopelman, R. Nanoparticles for Two-Photon Photodynamic Therapy in Living Cells. *Nano Lett.* **2006**, 6c (11), 2383–2386. https://doi.org/10.1021/nl0617179.

(40) Snyder, J. W.; Lambert, J. D. C.; Ogilby, P. R. 5,10,15,20-Tetrakis(N-Methyl-4-Pyridyl)-21H,23H-Porphine (TMPyP) as a Sensitizer for Singlet Oxygen Imaging in Cells: Characterizing the Irradiation-

Dependent Behavior of TMPyP in a Single Cell†. *Photochem. Photobiol.* **2006**, 82 (1), 177. https://doi.org/10.1562/2005-05-30-ra-553.

(41) Chen, L.; Lin, L.; Li, Y.; Lin, H.; Qiu, Z.; Gu, Y.; Li, B. Effect of Oxygen Concentration on Singlet Oxygen Luminescence Detection. *J. Lumin.* **2014**, 152, 98–102. https://doi.org/10.1016/j.jlumin.2013.10.034.

(42) Sierra, H.; Cordova, M.; Chen, C. S. J.; Rajadhyaksha, M. Confocal Imaging-Guided Laser Ablation of Basal Cell Carcinomas: An Ex Vivo Study. *J. Invest. Dermatol.* **2015**, 135 (2), 612–615. https://doi.org/10.1038/jid.2014.371.

(43) Gottfried, V.; Peled, D.; Winkelman, J. W.; Kimel, S. Photosensitizers in Organized Media: Singlet Oxygen Production and Spectral Properties*. Photochem. Photobiol.* **1988**, 48 (2), 157–163. https://doi.org/10.1111/j.1751-1097.1988.tb02801.x.

(44) Flors, C.; Fryer, M. J.; Waring, J.; Reeder, B.; Bechtold, U.; Mullineaux, P. M.; Nonell, S.; Wilson, M. T.; Baker, N. R. Imaging the Production of Singlet Oxygen in Vivo Using a New Fluorescent Sensor, Singlet Oxygen Sensor Green®. *J. Exp. Bot.* **2006**, 57 (8), 1725–1734. https://doi.org/10.1093/jxb/erj181.

(45) Gollmer, A.; Arnbjerg, J.; Blaikie, F. H.; Pedersen, B. W.; Breitenbach, T.; Daasbjerg, K.; Glasius, M.; Ogilby, P. R. Singlet Oxygen Sensor Green®: Photochemical Behavior in Solution and in a Mammalian Cell. *Photochem. Photobiol.* **2011**, 87 (3), 671–679. https://doi.org/10.1111/j.1751-1097.2011.00900.x.

(46) Ragàs, X.; Cooper, L. P.; White, J. H.; Nonell, S.; Flors, C. Quantification of Photosensitized Singlet Oxygen Production by a Fluorescent Protein. *ChemPhysChem* **2011**, 12 (1), 161–165. https://doi.org/10.1002/cphc.201000919.

(47) Mosmann, T. Rapid Colorimetric Assay for Cellular Growth and Survival: Application to Proliferation and Cytotoxicity Assays. *J. Immunol. Methods* **1983**, 65 (1–2), 55–63. https://doi.org/10.1016/0022-1759(83)90303-4.

(48) Yuan, X.; Zhang, B.; Luo, Z.; Yao, Q.; Leong, D. T.; Yan, N.; Xie, J. Balancing the Rate of Cluster Growth and Etching for Gram-Scale Synthesis of Thiolate-Protected Au_{25} Nanoclusters with Atomic Precision. *Angew. Chemie - Int. Ed.* **2014**, 53 (18), 4623–4627. https://doi.org/10.1002/anie.201311177.

(49) Danaei, M.; Dehghankhold, M.; Ataei, S.; Hasanzadeh Davarani, F.; Javanmard, R.; Dokhani, A.; Khorasani, S.; Mozafari, M. R. Impact of Particle Size and Polydispersity Index on the Clinical Applications of Lipidic Nanocarrier Systems. *Pharmaceutics* **2018**, 10 (2), 1–17. https://doi.org/10.3390/pharmaceutics10020057.

(50) Ray, A.; Yoon, H. K.; Koo Lee, Y. E.; Kopelman, R.; Wang, X. Sonophoric Nanoprobe Aided PH Measurement in Vivo Using Photoacoustic Spectroscopy. *Analyst* **2013**, 138 (11), 3126–3130. https://doi.org/10.1039/c3an00093a.

(51) Shirakura, T.; Kelson, T. J.; Ray, A.; Malyarenko, A. E.; Kopelman, R. Hydrogel Nanoparticles with Thermally Controlled Drug Release. *ACS Macro Lett.* **2014**, 3 (7), 602–606. https://doi.org/10.1021/mz500231e.

(52) Olesiak-Banska, J.; Waszkielewicz, M.; Matczyszyn, K.; Samoc, M. A Closer Look at Two-Photon Absorption, Absorption Saturation and Nonlinear Refraction in Gold Nanoclusters. *RSC Adv.* **2016**, 6 (101), 98748–98752. https://doi.org/10.1039/c6ra20610g.

(53) Devadas, M. S.; Kim, J.; Sinn, E.; Lee, D.; III, T. G.; Ramakrishna, G. Unique Ultrafast Visible Luminescence in Monolayer-Protected Au_{25} Clusters. *J. Phys. Chem. C* **2010**, 114, 22417–22423.

(54) Yi, C.; Zheng, H.; Herbert, P. J.; Chen, Y.; Jin, R.; Knappenberger, K. L. Ligand-and Solvent-Dependent Electronic Relaxation Dynamics of Au25(SR)18- Monolayer-Protected Clusters. *J. Phys. Chem. C* **2017**, 121 (39), 24894–24902. https://doi.org/10.1021/acs.jpcc.7b09347.

(55) Yousefalizadeh, G.; Stamplecoskie, K. G. A Single Model for the Excited-State Dynamics of $Au_{18}(SR)_{14}$ and $Au_{25}(SR)_{18}$ Clusters. *J. Phys. Chem. A* **2018**, 122 (35), 7014–7022. https://doi.org/10.1021/acs.jpca.8b07072.

(56) Wang, J.; Zhang, Z.; Zha, S.; Zhu, Y.; Wu, P.; Ehrenberg, B.; Chen, J. Y. Carbon Nanodots Featuring Efficient FRET for Two-Photon Photodynamic Cancer Therapy with a Low Fs Laser Power Density. *Biomaterials* **2014**, 35 (34), 9372–9381. https://doi.org/10.1016/j.biomaterials.2014.07.063.

(57) Stiel, H.; Teuchner, K.; Paul, A.; Leupold, D.; Kochevar, I. E. Quantitative Comparison of Excited State Properties and Intensity-Dependent Photosensitization by Rose Bengal. *J. Photochem. Photobiol. B Biol.* **1996**, 33 (3), 245–254. https://doi.org/10.1016/1011-1344(95)07248-9.

(58) Gonalves, P. J.; Franzen, P. L.; Correa, D. S.; Almeida, L. M.; Takara, M.; Ito, A. S.; Zílio, S. C.; Borissevitch, I. E. Effects of Environment on the Photophysical Characteristics of Mesotetrakis Methylpyridiniumyl Porphyrin (TMPyP). Spectrochim. *Acta - Part A Mol. Biomol. Spectrosc.* **2011**, 79 (5), 1532–1539. https://doi.org/10.1016/j.saa.2011.05.012.

(59) Wen, X.; Yu, P.; Toh, Y. R.; Hsu, A. C.; Lee, Y. C.; Tang, J. Fluorescence Dynamics in BSA-Protected Au_{25} Nanoclusters. *J. Phys. Chem. C* 2012, 116 (35), 19032–19038. https://doi.org/10.1021/jp305902w.

(60) Stamplecoskie, K. G.; Chen, Y. S.; Kamat, P. V. Excited-State Behavior of Luminescent Glutathione-Protected Gold Clusters. *J. Phys. Chem. C* **2014**, 118 (2), 1370–1376. https://doi.org/10.1021/jp410856h.

(61) Yu, P.; Wen, X.; Toh, Y. R.; Huang, J.; Tang, J. Metallophilic Bond-Induced Quenching of Delayed Fluorescence in Au 25@BSA Nanoclusters. *Part. Part. Syst. Charact.* **2013**, 30 (5), 467–472. https://doi.org/10.1002/ppsc.201200111.

(62) Devadas, M. S.; Kwak, K.; Park, J. W.; Choi, J. H.; Jun, C. H.; Sinn, E.; Ramakrishna, G.; Lee, D. Directional Electron Transfer in Chromophore-Labeled Quantum-Sized Au 25 Clusters: Au_{25} as an Electron Donor. *J. Phys. Chem. Lett.* **2010**, 1 (9), 1497–1503. https://doi.org/10.1021/jz100395p.

(63) Zhang, X. D.; Wu, D.; Shen, X.; Liu, P. X.; Fan, F. Y.; Fan, S. J. In Vivo Renal Clearance, Biodistribution, Toxicity of Gold Nanoclusters. *Biomaterials* **2012**, 33 (18), 4628–4638. https://doi.org/10.1016/j.biomaterials.2012.03.020.

(64) Bi, H.; Dai, Y.; Yang, P.; Xu, J.; Yang, D.; Gai, S.; He, F. Glutathione and H 2 O 2 Consumption Promoted Photodynamic and Chemotherapy Based on Biodegradable MnO_2 – Pt @ Au_{25} Nanosheets. *Chem. Eng. J.* **2019**, 356, 543–553. https://doi.org/10.1016/j.cej.2018.09.076.

(65) Yang, D.; Yang, G.; Gai, S.; He, F.; An, G.; Dai, Y.; Lv, R.; Yang, P. Au_{25} Cluster Functionalized Metal-Organic Nanostructures for Magnetically Targeted Photodynamic/Photothermal Therapy Triggered by Single Wavelength 808 Nm near-Infrared Light. *Nanoscale* **2015**, 7 (46), 19568–19578. https://doi.org/10.1039/c5nr06192j.

(66) Zhang, X. D.; Chen, J.; Luo, Z.; Wu, D.; Shen, X.; Song, S. S.; Sun, Y. M.; Liu, P. X.; Zhao, J.; Huo, S.; Fan, S; Liang, XJ; Xie, J. Enhanced Tumor Accumulation of Sub-2 Nm Gold Nanoclusters for Cancer Radiation Therapy. *Adv. Healthc. Mater.* **2014**, 3 (1), 133–141. https://doi.org/10.1002/adhm.201300189.

(67) Liu, P.; Yang, W.; Shi, L.; Zhang, H.; Xu, Y.; Wang, P.; Zhang, G.; Chen, W. R.; Zhang, B.; Wang, X. Concurrent Photothermal Therapy and Photodynamic Therapy for Cutaneous Squamous Cell Carcinoma by Gold Nanoclusters under a Single NIR Laser Irradiation. *J. Mater. Chem. B* **2019**, 7, 6924-6933. https://doi.org/10.1039/c9tb01573f.

(68) Kauffman, D. R.; Alfonso, D.; Matranga, C.; Li, G.; Jin, R. Photomediated Oxidation of Atomically Precise Au25(SC 2H4Ph)18 - Nanoclusters. *J. Phys. Chem. Lett.* **2013**, 4 (1), 195–202. https://doi.org/10.1021/jz302056q.

(69) Ray, A.; Wang, X.; Lee, Y. E. K.; Hah, H. J.; Kim, G.; Chen, T.; Orringer, D. A.; Sagher, O.; Liu, X.; Kopelman, R. Targeted Blue Nanoparticles as Photoacoustic Contrast Agent for Brain Tumor Delineation. *Nano Res.* **2011**, 4 (11), 1163–1173. https://doi.org/10.1007/s12274-011-0166-1.

(70) Winer, I.; Wang, S.; Lee, Y. E. K.; Fan, W.; Gong, Y.; Burgos-Ojeda, D.; Spahlinger, G.; Kopelman, R.; Buckanovich, R. J. F3-Targeted Cisplatin-Hydrogel Nanoparticles as an Effective Therapeutic That

Targets Both Murine and Human Ovarian Tumor Endothelial Cells in Vivo. *Cancer Res.* **2010**, 70 (21), 8674–8683. https://doi.org/10.1158/0008-5472.CAN-10-1917.

(71) Gao, D.; Agayan, R. R.; Xu, H.; Philbert, M. A.; Kopelman, R. Nanoparticles for Two-Photon Photodynamic Therapy in Living Cells. *Nano Lett.* **2006**, 6 (11), 2383–2386. https://doi.org/10.1021/nl0617179.

(72) Hu, W.; He, T.; Jiang, R.; Yin, J.; Li, L.; Lu, X.; Zhao, H.; Zhang, L.; Huang, L.; Sun, H.; Huang, W; Fan, Q. Inner Salt-Shaped Small Molecular Photosensitizer with Extremely Enhanced Two-Photon Absorption for Mitochondrial-Targeted Photodynamic Therapy. *Chem. Commun.* **2017**, 53 (10), 1680–1683. https://doi.org/10.1039/c6cc09473b.

(73) Luo, L.; Zhang, Q.; Luo, Y.; He, Z.; Tian, X.; Battaglia, G. Thermosensitive Nanocomposite Gel for Intra-Tumoral Two-Photon Photodynamic Therapy. *J. Control. Release* **2019**, 298, 99–109. https://doi.org/10.1016/j.jconrel.2019.01.019.

(74) Bratosin, D.; Mitrofan, L.; Palii, C.; Estaquier, J.; Montreuil, J. Novel Fluorescence Assay Using Calcein-AM for the Determination of Human Erythrocyte Viability and Aging. *Cytometry* **2005**, 66A, 78-74. https://doi.org/10.1002/cyto.a.20152.

(75) Kachynski, A. V.; Pliss, A.; Kuzmin, A. N.; Ohulchanskyy, T. Y.; Baev, A.; Qu, J.; Prasad, P. N. Photodynamic Therapy by in Situ Nonlinear Photon Conversion. *Nat. Photonics* **2014**, 8 (6), 455–461. https://doi.org/10.1038/nphoton.2014.90.

(76) Gu, B.; Wu, W.; Xu, G.; Feng, G.; Yin, F.; Chong, P. H. J.; Qu, J.; Yong, K. T.; Liu, B. Precise Two-Photon Photodynamic Therapy Using an Efficient Photosensitizer with Aggregation-Induced Emission Characteristics. *Adv. Mater.* **2017**, 29 (28), 1–7. https://doi.org/10.1002/adma.201701076.

(77) Katla, S. K.; Zhang, J.; Castro, E.; Bernal, R. A.; Li, X. Atomically Precise $Au_{25}(SG)_{18}$ Nanoclusters: Rapid Single-Step Synthesis and Application in Photothermal Therapy. *ACS Appl. Mater. Interfaces* **2018**, 10 (1), 75–82. https://doi.org/10.1021/acsami.7b12614.

(78) Reuveni, T.; Motiei, M.; Romman, Z.; Popovtzer, A.; Popovtzer, R. Targeted Gold Nanoparticles Enable Molecular CT Imaging of Cancer: An in Vivo Study. *Int. J. Nanomedicine* **2011**, 6, 2859–2864. https://doi.org/10.2147/ijn.s25446.

(79) Zhang, X. D.; Luo, Z.; Chen, J.; Song, S.; Yuan, X.; Shen, X.; Wang, H.; Sun, Y.; Gao, K.; Zhang, L.; Fan, S; Leong, D; Guo, M; Xie, J. Ultrasmall Glutathione-Protected Gold Nanoclusters as next Generation Radiotherapy Sensitizers with High Tumor Uptake and High Renal Clearance. *Sci. Rep.* **2015**, 5, 1–7. https://doi.org/10.1038/srep08669.

Chapter 3: Gold Nanosnakes: Controlled Synthesis of Linear Nanochains with Tunable Plasmon Resonance for Nano-Biophotonics

3.1 Abstract

The development of plasmonic nanomaterials with controlled linearization and optical tunability is of wide interest in biophotonics and nanomedicine, provided they are biocompatible. Highly linear gold nanochains, “gold nanosnakes”, were prepared by a controlled synthesis scheme, starting from ultrapure gold nanosphere monomers, having a bare (virgin) surface. They exhibit 1-2 nm tunable longitudinal surface plasmon resonance (LSPR) over the range from 590 to 640 nm. To determine the ensemble statistics of the nanosnake lengths and their branching, transmission electron microscopy (TEM) images were acquired, in batch, correlated with the nanosnake longitudinal SPR maxima (590 to 640 nm). Utilizing the distributions from TEM image analysis, discrete dipole approximation computations reproduce the experimental UV-Vis spectra, confirming sample integrity. *In vitro* dark-field microscopy, and biocompatibility measurements, demonstrate the nanosnakes’ (1) enhanced scattering cross-sections related to the plasmon coupling between the constituent nanospheres, (2) highly accessible surface enabling facile conjugating with cell targeting ligands, and (3) absence of cell toxicity. Monte-Carlo simulations quantify the selectivity of the chemical reaction: chain-end gold nanosphere units are 3-4 times more reactive than chain-center units. The synthesized, highly-linear, spectrally tunable gold nanosnakes represent a new and biocompatible nanosystem, which could be utilized in photonic, biomedical, and theranostic applications.

3.2 Introduction

Colloidal gold nanoparticles (Au NPs) have been intensively studied and utilized over a broad range of biomedical fields, such as imaging[1–4], chemical sensing[5–7], diagnostics[1,8], and cancer/disease therapies[8–13]. Au NP colloids display unique size-, morphology-, and composition-dependent optical properties not observed from their bulk or molecular counterparts (e.g. nanoclusters) that produce their utility.[14–16] These new properties have been attributed to a longitudinal surface plasmon resonance (LSPR) that arises from collective oscillations of the conducting electrons in the valence band.[17,18] A colloidal solution of Au NP monomers can be produced in large quantities, via chemical (synthetic) approaches.[19] Alternatively they can be produced by physical methods, like the one used in the present study: pulsed laser ablation (PLA).[17,20] However, the scalable production of dimer, trimer, and higher order nanochains (tetramers, pentamers, etc.) is still exploratory. Overall, colloidal gold nanochains can have many advantages as a new nanomaterial. For example, these gold nanochains, when linear, exhibit significantly red-shifted absorption spectra, thus allowing imaging at redder wavelengths, i.e. within the biological window of optical absorbance and lower light scattering.[21] In addition, gold nanochains have been shown to have enhanced scattering cross-sections, thus an increased potential for SERS (surface enhanced Raman spectroscopy), due to the existence of plasmonic hot spots inside the gaps of the NPs within the chain.[22,23]

The step-growth synthesis of colloidal gold nanochains has been documented in the past.[24–26] Several methods have been used to fabricate such nanosystems, including template-based methods (lithography, shell-driven aggregation) and template-free methods, and different types of monomers have been utilized, like Au nanospheres and Au nanorods. Template-based methods, for example lithographic arrays, or polydimethylsiloxane (PDMS) substrates, can be used to synthesize plasmonic nanomaterials (chains, globular clusters), but require extensive fabrication and specialized molds.[27–29] Thus, while lithographic arrays can produce nanochains with low polydispersity, the cost, fabrication time, and

scalability are major limitations on the use of such lithographic (i.e. electron beam, ion beam) techniques.[30] Utilizing PDMS molds is a promising new, cheaper technology for fabricating nanochains and nanoglobules; however, controlling gap distances, dispersity, and plasmonic tunability, in addition to scalability, remain as challenges.[28,29] Alternatively, polymeric shells and chiral small molecule-conjugated micelles ('surface template' nanochemistry) have been used to encapsulate Au NPs so as to create polydisperse linear nanochains; however shell formation is irreversible and biotoxicity remains an issue, with its severity depending on the polymers used.[31–33] Template-free methods have also been used to synthesize nanochains, but most require ethanol and typically occur over short timescales (<30 min). However, long timescales are desired so as to better control nanochain formation.[21,26,34,35] More specifically, inducing nanochain assembly over long timescales has two advantages: 1.) Synthesizing highly precise LSPR nanomaterials is more easily achievable using longer time scales, because the quenching-time is less prone to error, 2.) Longer timescales are typically required so as to produce highly linear chains.[26,36] For example, Yang et. al. demonstrated that when polymer-assisted nanochain aggregation occurred over long timescales (8 hours), samples were highly linear and the spectral band (LSPR shift) was sharp and pronounced.[26] However, over fast timescales, globular products formed with a wide spectral band-width.[26] Most aqueous-based techniques, such as Au NP-aptamer aggregate synthesis, have been useful in producing globular clusters, but the production of highly anisotropic, linear clusters has remained a challenge.[37,38] Notably, Au nanospheres, rather than Au nanorods, are utilized for chain formation in the present study. Au nanorods may have been the most studied material for their optical property of a tunable plasmonic resonance.[39] However, Au nanorods have intrinsic disadvantages as a biomedical material, including the cetyltrimethylammonium bromide (CTAB) conjugation that makes the nanorods toxic.[40–42] Also, the ligand-exchange methods that are required for modifying the nanorod surface do hinder greatly both ease-of-fabrication and scalability.[42] For example, so as to conjugate nanorods with thiolated peg, the ligand-replacement takes 24 hours due to the strong binding of the CTAB, as reported

by Wan et. al.[42] Also, in contrast to elongated Au nanorods, the here assembled Au nanosphere chains, with their nano-gaps (between nanospheres), provide highly intense electric field hotspots, and such intense fields are of interest to many applications, such as imaging and microscopy.[43,44]

In the present study, we report a facile method for large-scale fabrication of highly linear and biocompatible gold nanochains suspended in aqueous solution with controllable length and short interparticle gap distance (<2 nm). These highly linear gold nanochains are named "gold nanosnakes" in the rest of this paper. They are synthesized via first producing 20 nm Au NP monomers having virgin surfaces, using the pulsed-laser ablation (PLA) method, as shown in Figure 3.1-1. The PLA method was chosen here because compared to other, typically chemical, methods it is a complete green synthesis (fulfilling all 12 principles of green chemistry).[45,46] Thus we produce nontoxic, stable, and high-purity Au NP monomers in deionized (DI) water. To perform the PLA method, a high-power, femtosecond pulsed laser ablates the pure bulk Au metal in DI water (Figure 3.1-1), and the Au NPs are formed in the same DI water, thus not requiring precursor, reductant, stabilizing or capping agents. Hence this method does not introduce any chemical toxicity or biological hazards; it is thus a low environmentally impacting technique. Furthermore, these PLA-generated AuNP monomers, with their bare (virgin) surfaces, provide unique surface properties. For example, in our previous studies we have demonstrated that the bare (virgin) surface ensures facile, rapid (1-2 hours), and highly controllable conjugation of ligands, such as methoxy polyethylene glycol (mPEG), with a tunable surface coverage between 0 to 100%.[47,48] Also, efficient peptide and small molecule conjugation has been demonstrated on PLA-produced Au monomers with high molar ratios (on the scale of thousands of peptides per gold NP).[49,50] As such, PLA-produced Au nanospheres, with their virgin surfaces, may be the best starting material for nanochain development involving highly controlled surfaces.

After the fabrication of the Au NP monomers, the self-assembly of colloidal Au NPs into nanosnakes in aqueous solution was performed by modifying the Au NP surface with two different types

of ligands: pentapeptide with an amino acid sequence CALNN and cysteamine (Figure 3.1-2). This was done in a sequential manner by first mixing the colloidal Au NPs with CALNN and then with cysteamine. The binding to the NPs of the CALNN peptides and the cysteamine is possible due to the strong anchoring of the gold-sulfur bonds, which covalently attach two ligands to the surface of the Au NPs. The CALNN peptides were bound onto the NPs because they are well-known ligands for improving NP colloidal stability.[51] The latter is critical so as to achieve a proper balance between the repulsive and attractive forces after addition of the cysteamine molecules, which is a governing factor in linker-mediated assembly of NPs.[52] The cysteamine molecules were coated onto the nanoparticles because they contain two reactive terminal groups, sulfhydryl (-SH) and amine (-NH2), which can link or bridge Au NPs via attaching to their surface by either covalent bonds (-SH groups) or by electrostatic attraction (-NH2), thereby forming nanosnakes within 24 – 72 hours, depending on the desired longitudinal SPR shift (Figure 3.1-3). It is worth noting that only the minimal amount of CALNN peptides and cysteamine molecules necessary for inducing nanosnakes formation is used for the surface modification of the Au NPs. In this way, enough space is left on the surfaces of the gold nanosnakes for subsequent conjugation of biomolecules, such as targeting ligands necessary for use in various biomedical applications. Notably, utilizing UV-Vis spectroscopy to 'monitor' chain assembly, the growth of the nanochains can be quenched at will by adding thiol terminated methoxy polyethylene glycol (mPEG-SH), as shown in Figure 3.1-4.

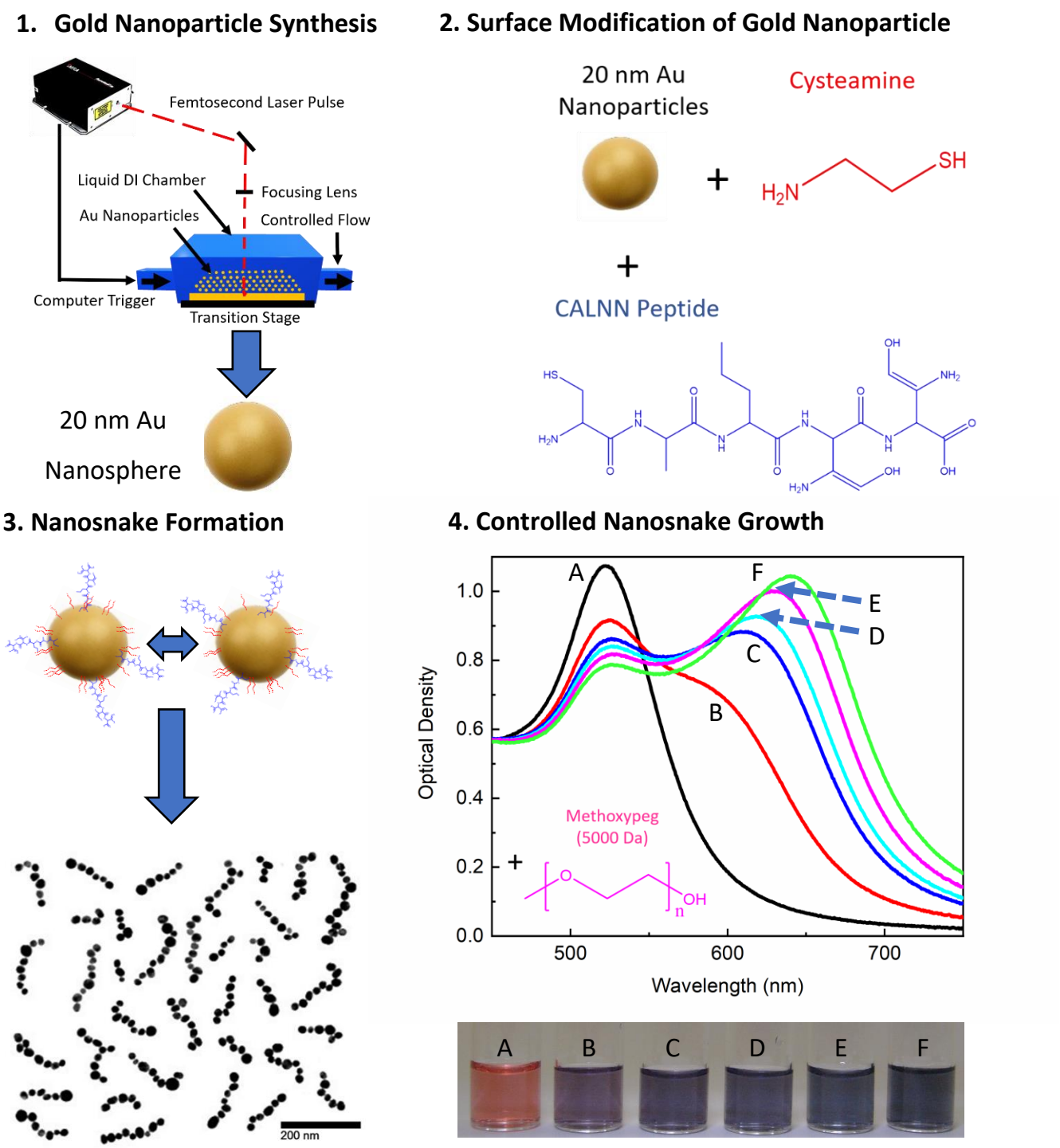

Figure 3.1 Summary of nanosnake formation. Step 1. Au nanoparticle monomers of 20 nm in diameter, having virgin surfaces, are produced by pulsed laser ablation. Step 2. Surfaces of monomers are modified with CALNN peptide (blue; 2400:1) and cysteamine (red; 1800:1). Step 3. Self-assembly of monomers into

nanosnakes after surface modification. The ensemble of nanosnakes with longitudinal surface plasmon resonance (LSPR) mode at 620 nm is shown as an example. Step 4. Nanosnake growth is controlled by UV-Vis monitoring and quenching at a desired LSPR, using thiol terminated methoxy polyethylene glycol (mPEG-SH) with molecular weight of 5000 Da. The gold nanosnake samples synthesized are labeled in the photograph insert [A, gold monomer with SPR at about 525 nm; B-F nanosnake samples with LSPR at 590 nm (B), 610 nm (C), 620 nm (D), 630 nm (E), and at 640 nm (F)].

Overall, the advantages of our technique are:

1.) Starting from 20 nm Au NP monomers produced by the PLA method with a virgin surface (homogenous and ultrapure) allows for their controlled self-assembly on a large scale. As mentioned earlier, the surface conjugation is facile, rapid (1-2 hours), non-toxic, and highly controlled (ligand ratios for surface conjugation between 0-100% can be precisely controlled). Currently, the batch volume of nanosnake synthesis with optical density (OD) 1, at the tunable LSPR, is 1 liter.
2.) The self-assembly of nanosnakes (from Au monomers) can be spectrally monitored and tuned, wherein rapid quenching can be used to select for the desired plasmonic wavelength, with a spectral resolution precision of about a couple of nanometers (1-2 nm).
3.) Unlike other anisotropic gold nanosystems, i.e. assembled nanorods which suffer from high toxicity and challenging conjugation paradigms[40–42], the Au nanosnake synthesis does not involve toxic intermediates and, in addition, the surface conjugation with peptides or small molecules is facile.
4.) The Au nanosnakes have intense electric field hotspots in the gaps between monomers, of immense potential utility for a variety of imaging and microscopy applications.
5.) The synthesis is performed in aqueous environments (DI water) and samples can thus be used immediately upon synthesis completion.

Using the above method, we have synthesized five samples of highly linear gold nanosnakes exhibiting red-shifted longitudinal SPR from 590 nm to 640 nm, and verified their linearity by transmission electron microscopy (TEM). In addition, Monte-Carlo simulations of nanosnake formation from Au NP monomers have been performed, which provide an interesting insight into the selectivity of the synthesis, revealing that the *center* units of nanosnakes are about 3-4 times less reactive than their *end* units, thus preventing chain branching and thus driving the growth of highly linear nanosnakes, rather than nanoglobules. Furthermore, by coupling the theoretical results of DDA (discrete dipole approximation), calculations of the extinction spectra for each linear oligomer (monomer, dimer, trimer, etc.) with the weighted experimental nanosnake length distribution obtained from TEM image analysis, we can reproduce the optical extinction spectra for all experimental samples, thus confirming sample integrity. Moreover, we have confirmed the enhanced scattering cross sections of the nanosnakes revealed from our DDA calculations (enhanced by approximately 3x when normalized to the number of AuNP monomers constituting the nanosnakes) via comparing the brightness of the nanosnakes to that of the AuNP monomers, observed *in vitro* by dark-field light scattering microscopy. Lastly, the *in-vitro* (3-(4,5-dimethylthiazol-2-yl)-2,5-diphenyltetrazolium bromide) tetrazolium reduction assay (MTT) demonstrates the gold nanosnakes' little or no cytotoxicity at a mass concentration as high as 0.25 mg/mL. Therefore, the synthesized gold nanosnakes have several highly desirable properties for a wide range of potential biomedical applications, such as enhanced *in vitro* and *in vivo* contrast imaging, diagnostics, and targeted theranostics.

3.3 Experimental Procedures

3.3.1 Materials and Instrumentation

All chemicals were used as received without further purification. mPEG-SH with a molar mass of 5000 g mol^{-1} (mPEG 5k-SH) was purchased from Creative PEGWorks (Chapel Hill, NC). Both cysteine-modified Arginine–glycine–aspartic acid (RGD)-containing peptides with an amino acid sequence

RGDRGDRGDRGDPGC and pentapeptide ligand with an amino acid sequence CALNN having purity higher than 95% were custom-synthesized by RS synthesis LLC (Louisville, KY). Cysteamine (CAS Number: 60-23-1) with purity higher than 95% was purchased from Sigma-Aldrich. PEG, peptides, and cysteamine were in powder form and dissolved in DI (de-ionized) water having an electric conductivity less than 0.7 μS cm^{-1}. All solutions were freshly made as needed and used within twelve hours. UV–Vis absorption spectra were recorded by a spectrophotometer (UV-3600, Shimadzu Corp., Japan).

3.3.2 Production of the colloidal Au NPs

We first produced primary spherical colloidal Au NPs having virgin surfaces, to be used for the fabrication of gold nanosnakes via a physical method of femtosecond PLA of a bulk Au target (Purity: 99.99%) immersed in DI water, as described in our previous publication.[47] This method uses tightly focused micro-joule (μJ) femtosecond laser pulses to produce NPs and the size/size distribution of the generated NPs can be precisely controlled by optimizing the laser parameters, such as wavelength, pulse energy, duration, and repetition rate.[47]

Briefly, the ytterbium-doped femtosecond fiber laser (FCPA μJewel D-1000, IMRA America, Ann Arbor, MI), operating at 1.045 μm, delivered laser pulses at a repetition rate of 100 kHz, with 10 μJ pulse energy and 700 fs pulse duration. The emitted laser beam was first focused by an objective lens and then reflected by a scanning mirror to the surface of the bulk gold target, which was submerged in flowing de-ionized water (18 MΩcm). The size of the laser spot on the gold target was estimated to be 50 μm and its position was precisely controlled by the scanning mirror. Colloidal Au NPs with an average diameter of 20 nm were produced by this PLA method and used in our experiments. The generated nanoparticles have a narrow size distribution and have an absorption peak at 520 nm due to the localized surface plasmon resonance.[38]

It is worth mentioning that during the PLA, the generated Au NPs are partially oxidized by oxygen present in the solution. These Au-O compounds were hydroxylated, followed by a proton loss, to give a

surface of Au-O^-.[53] Therefore, the Au NPs produced using the PLA method are naturally negatively charged and no capping agents or stabilizing ligands are required for maintaining their colloidal stability. This unique feature of having a virgin surface because of a capping-agent free procedure does allow versatile surface modifications for obtaining Au NPs with controllable surface chemistry,[47] which is utilized in the present study to assemble them into spectrally tunable gold nanosnakes.

3.3.3 Characterization of Au Nanoparticle Surface Coverage

To characterize the surface coverage of the Au nanoparticles, dynamic light scattering (DLS) was used to measure the increase in the Au NP radius after the small molecule (i.e. peptide) coverage. Dynamic light scattering has been used before to study surface conjugation of Au NPs by peptides.[54,55] In brief, the hydrodynamic diameter of the peptide-modified (CALNN peptide in this study) gold nanoparticle monomer nanospheres (20 nm), which includes the nanoparticle surface coating and the hydrated water ions, is measured (Malvern Nano Zetasizer ZS90 DLS). The Malvern Nano Zetasizer DLS is equipped with a 633 nm He–Ne laser and an avalanche photodiode serves for detecting the scattered light at a 90-degree angle. In a standard measurement made in the automated mode, the instrument selected the attenuation factor and then recorded between 12 and 16 runs, measuring the dynamic light scattering (DLS) of the nanoparticles, which is determined by their Brownian motion, for calculating the intensity-average diameter. Three successive DLS measurements were performed for each sample and the mean diameter increase was reported with the error bar corresponding to the standard deviation over these three measurements. As shown in Figure 3.2, a 20,000:1 molar peptide ratio is required for surface saturation, indicating that the CALNN (2400:1), cysteamine (1800:1), and peg (200:1) molar ratios used in this study will not result in complete surface coverage for the 20 nm Au monomers.

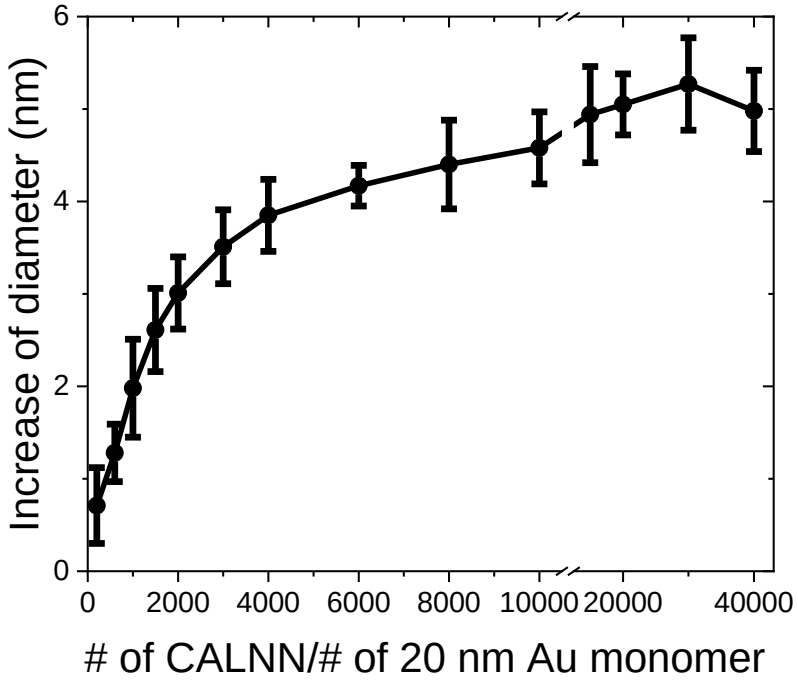

Figure 3.2 Increased diameter (nm) of 20 nm Au monomers after CALNN peptide conjugation at various CALNN molar conjugation ratios (200:1-40000:1) determined through dynamic light scattering (DLS).

3.3.4 Self-assembly of Au NPs into Nanosnakes

In a typical process, colloidal Au NPs with an average diameter of 20 nm (STD 3 nm) and a zeta potential of -40 mV were mixed with a pH 7.0 aqueous solution of CALNN peptides, so as to achieve a defined molar ratio of 2400:1 between the CALNN peptides and the Au NPs. The mixture of Au NPs and CALNN peptides was kept undisturbed for 2 hrs at room temperature so as to enable sufficient conjugation of CALNN peptides to the Au NPs via gold-sulfur bonds. Following the surface conjugation of the CALNN peptide, the Au NPs were further modified with cysteamine molecules, by mixing with the cysteamine solution, so as to achieve a molar ratio of 1800:1 between the cysteamine molecules and the Au NPs. The solution was kept undisturbed until observing a significant color change, from red-pink to blue, which typically occurs between 24 hours to 72 hours after addition of cysteamine and serves as clear evidence for a successful self-assembly of NPs into nanosnakes.

Furthermore, gold nanosnakes with controllable lengths and tunable LSPR were fabricated by quenching the growth of the nanosnakes via binding mPEG 5k-SH molecules onto them after their LSPR reaches a desired wavelength. This was done by adding a solution of mPEG 5k-SH so as to achieve a molar ratio of 200:1 between the mPEG 5k-SH molecules and the Au NPs. The PEG molecules can stop the growth of the nanosnakes because they introduce steric repulsions between the Au NPs. Notably, PEG with molecular weight of 5000 Da specifically has been used by other groups (i.e. Scott et. al.) in biological nanosystems so as to reduce adsorption.[56] In the present study a total of five distinct samples of gold nanosnakes were produced, with the LSPR ranging from 590 nm to 640 nm.

In our search of the CALNN and cysteamine ratios to be used for fabricating the gold nanosnakes, our principle for determining the appropriate ratio was to choose the minimal amounts of CALNN and cysteamine necessary for inducing the self-assembly of Au NP monomers into stable nanosnakes. By minimizing the molar ratio of each component, there remains enough empty space on the surface of the nanosnakes for subsequent conjugation of other functional ligands. Based on this principle, we found the ratios of 2400:1 and 1800:1 to be the best ratios, respectively, for the CALNN/Au NP and cysteamine/Au NP conjugations. Furthermore, in terms of pH stability, Jia. et. al. showed that CALNN conjugated Au NPs have stable aggregation properties for pH<9.[57] For cysteamine, within the range of pH 4-10, Au-cysteamine aggregates have been shown to be stable, with pH>10 resulting in the deprotonation of the sulfur moiety, leading to destabilization of the product.[58,59] Notably, our *in vitro* experiments were performed at pH = 7.4, under stable pH conditions.

3.3.5 Transmission Electron Microscopy (TEM) and Image Analysis

Nanosnake samples were deposited on TED Pella (trade name) 200 Cu mesh grids (Lot#: 160419). To determine the mass distributions of the Au nanosnakes, TEM imaging was performed at 80 kV on a JOEL JEM 1400 transmission electron microscope. For every sample, 3 grids were analyzed with over 50 images taken per grid at 10,000x magnification. After image acquisition, individual nanosnakes were

cropped via ImageJ from the raw images. Following cropping, so as to identify the number of monomers in each nanoparticle, the images were analyzed using the CellProfiler program.[60] In brief, CellProfiler can identify objects using an intensity threshold (lowest accepted pixel intensity compared to max intensity) and the shape of the object (circular), and has been shown to be a useful tool to conduct quality control for properties like the size and shape of nanoparticles and nanoparticle aggregates.[61] For this study, thresholds of 60, 70, and 80% were tested for identifying individual monomer shapes. As the sample images show in Figure 3.3, the CellProfiler output identifies individual monomers from their circular outline (the monomers identified are given separate colors). After identification, the number of counted monomers within a nanosnake are summed together to determine the total number of monomers per nanosnake. Due to the intensity variation between samples, the highest count was selected among 60, 70, and 80% thresholds.

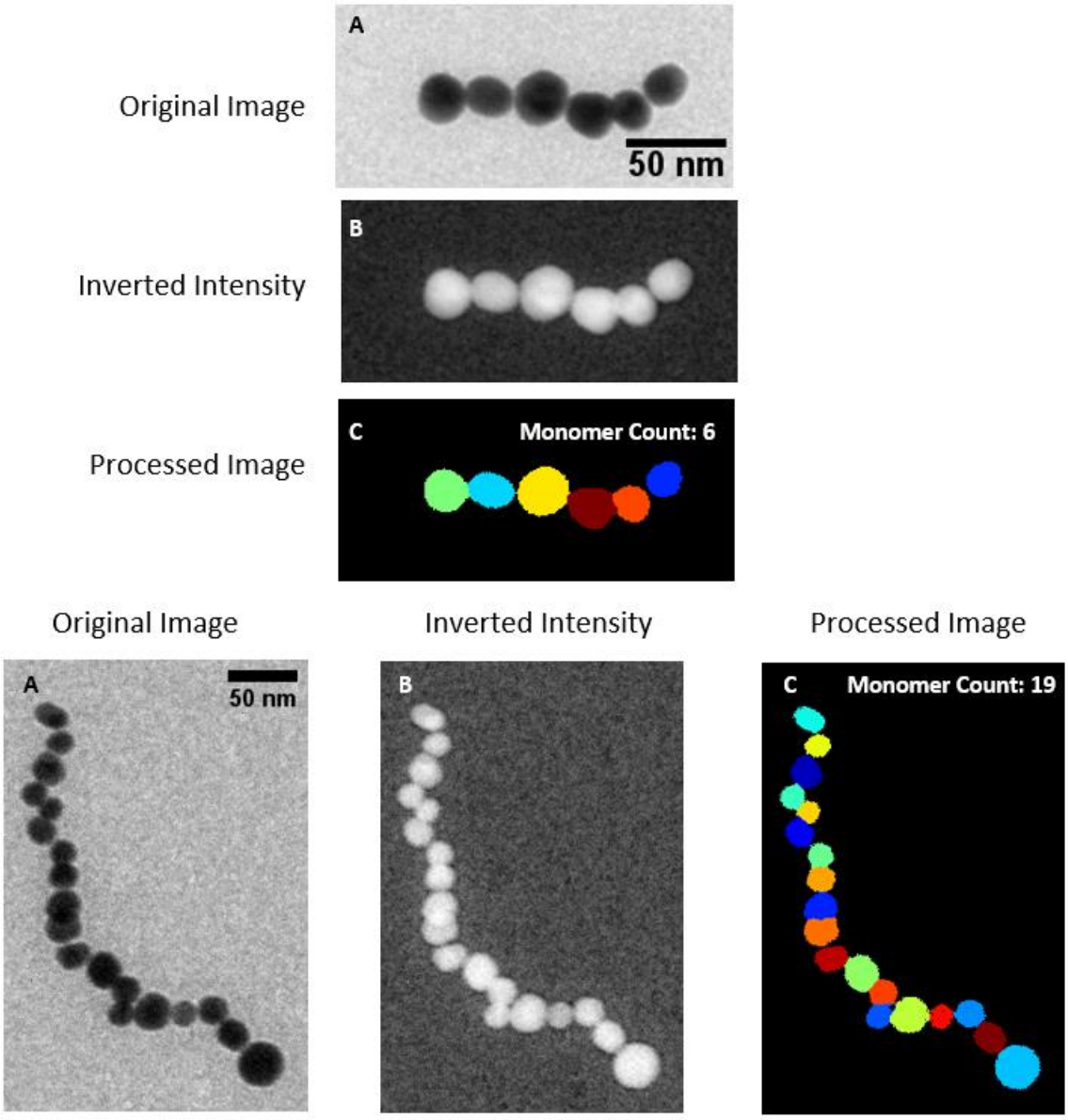

Figure 3.3 Nanosnakes processed through CellProfiler. For each nanosnake pair, the A.) original image (no scale bar) is B.) inverted, and then C.) processed through CellProfiler, where each unique color is an identified counted monomer.

High resolution TEM microscopy was utilized to determine the gap distance (spacing) between monomers in the Au nanosnakes. The high resolution microscopy was performed on a JEOL JEM 2100F scanning transmission electron microscope. Under such conditions, pixel resolution ranges from 0.05 –

0.5 nm, using highest (2500000x) and lowest (250000x) magnifications. After acquiring high resolution TEM images, the gap distances were analyzed using ImageJ 'measure' tool on raw (unadjusted) intensity data by importing image data with the NIH developed DM3 Reader Plugin (https://imagej.nih.gov/ij/plugins/DM3_Reader.html). Note that to preserve image fidelity, DM3 images were utilized for gap distance determination, instead of converting images to a compressed format. For each gap distance, measurements were collected three times and averaged to determine the error (standard deviation reported).

3.3.6 Monte Carlo (MC) Simulations

A number of NPs (monomers), equal to the total number of NPs for each experiment, are randomly placed on a cubic lattice with fixed concentration ($c = 10^{-3}$ for the 3-dimensional lattice). The monomers are considered to be clusters of size s = 1. Diffusion of the clusters starts by randomly choosing a cluster and allowing it to move to a neighboring position, which consumes one microstep. The diffusion constant is considered to be inversely proportional to m, the mass.[62–64] Thus a random number $x \in (0,1)$ is chosen and if $x < 1/m$ the cluster diffuses by moving one cell length in a random direction to a neighboring site (or sites) on the lattice, assuming they are not already occupied by the NPs of another cluster (excluded volume condition). If two or more clusters contact each other (i.e. there are monomers at neighboring sites), they merge into one cluster with a (sticking) probability that depends on the position of the contacting NPs in the cluster. The ratio of the sticking probabilities of *end* vs. *center* particles was tested at 0.01, 0.1, 0.2, 0.3, 0.5, and 1.0. Thus, we have p = 1 if the contacting monomers of both clusters are at the end of their cluster and p = 0.01-1.0 otherwise. For each monomer we keep track of the number n of neighboring monomers to which it is connected. Thus, a lone monomer (cluster of size s = 1) has n = 0, the monomers of a cluster with size s = 2 both have n = 1, a linear cluster with size s = 3 has two monomers (at the edges) with n = 1 and one central monomer with n = 2. A cluster's monomers that have

n = 0 or n = 1 are considered to be at the *end* of the cluster. Other monomers in a cluster with n > 1 are "central". Sticking to them has the adjusted probability provided above (0.01-1.0).

The time after each step is increased by Δt = 1/N (one MC microstep), where N is the number of clusters remaining, regardless of whether the cluster moved or not.[65–67] Clusters of increasing size s are formed as the simulation proceeds and the simulation stops when the number N of the remaining clusters becomes equal to the number of clusters in the target experimental sample. Whenever two objects (particles or clusters) are merged into one, they are combined irreversibly and the number of neighbors of the contacting monomers is increased by 1, with periodic boundary conditions utilized. Monte Carlo simulations are run 100 times per sample, and the cluster distributions are averaged.

3.3.7 Discrete Dipole Approximation (DDA) Calculations

Discrete dipole calculations were performed using DDSCAT ("Discrete Dipole Scattering") version 7.3.2 to compute the optical extinction coefficient, absorbance, and scattering spectra of linear clusters of Au NPs in an aqueous medium (n = 1.33). Reviews of the discrete dipole approximation technique and DDSCAT have been provided by previous authors.[68,69] To run DDSCAT, several user inputs are required: 1.) The complex polarizability of Au, 2.) The geometry of the Au NP clusters, and 3.) The Effective radius of the Au NP snakes (See Equation 3.1). The complex polarizability (function of wavelength from 300-800 nm) of Au was utilized from Johnson et. al.[70] To generate the geometry of the Au NP clusters, we wrote a Python code that specifies the monomer radius, the length of linear clusters of Au NPs, and the interparticle gap distance, so as to generate input files. The following code is posted to GitHub in a public repository at: https://github.com/KopelmanLab. Lastly, the effective radius is computed by,

$$r_{eff} = (n(r_{monomer})^3)^{1/3} \quad (3.1)$$

Here r_{eff} is the effective radius, n is the length (number of units) of the linear clusters, and $r_{monomer}$ is the radius of an Au NP monomer (10 nm).

Of particular importance for the discrete dipole computations is the number of dipoles-per-nanometer (dpnm) in the input geometry.[71,72] Previous studies have found that above a 1 dpnm resolution for nanosized objects, the generated spectra are minimally affected by dpnm increases.[72] Hence, within the main body of this paper, all spectra are generated from 1 dpnm geometries.

Following the DDSCAT computations, UV-Vis spectra were generated based on the simulated DDA extinction spectra and the experimentally measured mass distributions of the synthesized gold nanosnakes. Figure 3.4 shows a summary of the steps required for this process. In brief, a weighted linear combination of the DDA-computed spectra for linear clusters of Au NPs was taken with respect to each oligomer's percent frequency from the experimental TEM distribution. For every element (i.e. dimer, trimer, etc.) within the computed DDA linear combination set, the incoming light (k-vector) x, y, z orientational contribution to the extinction spectra was averaged with equal weight (light is unpolarized along each orientation). Furthermore, due to the 'resolution' of DDSCAT (using a 1 dpnm computation can only yield output for integer spacing), non-integer gap distance extinction spectra were interpolated using the 1.00, 2.00, and 3.00 nm computed extinction spectra at each wavelength (350 – 800 nm) from 2nd order polynomial fitting.

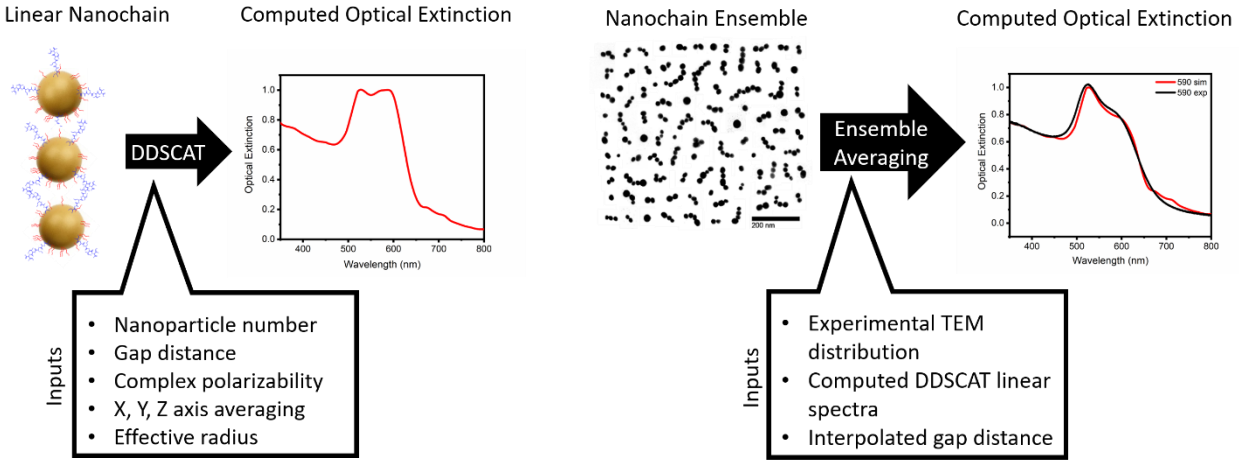

Figure 3.4 Protocol used to compute the optical extinction spectra of the nanochain ensemble. First, the optical extinction spectrum of each linear nanochain is computed via DDSCAT assuming unpolarized

excitation (left diagram with example spectrum). Next, ensemble averaging is performed utilizing TEM distributions to generate a simulated spectra (red) compared to an experimental spectra (black).

A mean squared error of the computed optical extinction spectra of the ensemble average was determined using gap distances ranging from 0.8 nm to 2.0 nm, with 0.05 nm resolution. The mean squared error (MSE) is defined as,

$$\text{MSE} = \frac{\Sigma(n_{theoretical} - n_{sample})^2}{n} \quad (3.2)$$

Where $n_{theoretical}$ is the value of the theoretical point (i.e. simulated 'y') at value 'x', n_{sample} is the value of the sample point (i.e. experimental 'y') at the same 'x', and n is the total number of theoretical samples evaluated in the sum. To generate the electric field data, DDSCAT electric field output (.E format) was converted to VTR format and imaged using the Mayavi Python package.[73]

3.3.8 Conjugation of RGD Peptides onto Au Nanosnakes

RGD peptides are well-known to bind preferentially to the αvβ3 integrin proteins, which are overexpressed on the surface of most types of cancer cells.[74] Therefore, we chose to conjugate them onto gold nanosnakes for obtaining cancer cell-targeting conjugates. Within five gold nanosnake samples fabricated, the samples with LSPR at 640 nm were selected for this conjugation and the conjugation was done by adding 12 uL RGD peptide solution, with a concentration of 1 mM, to a 10 mL sample of gold nanosnakes with an optical density (OD) of 1 at 640 nm. The resultant solutions were allowed to stand for 2 hrs at room temperature, to ensure a sufficient conjugation of the RGD peptides onto the unoccupied surfaces of the gold nanosnakes. The final solution was transferred into a 15 mL centrifugal tube and centrifuged at 1000 g for 0.5 hr. After removing the supernatant, the final OD of the RGD peptide-conjugated colloidal gold nanosnakes was adjusted to 10 by resuspending the NP pellet with a 4 mM borate buffer (pH 8.2) containing 5 mg/mL BSA.

3.3.9 Human HeLa Cell Culture

The Human HeLa 229 cell line was selected for our study and was cultured according to the following protocol. (1) 6 mL human HeLa 229 cells in the logarithmic growth phase (American Type Culture Collection), at a density of 1 X 10^4 cells/ml, prepared in Dulbecco's modified Eagle medium (DMEM 11995) supplemented with 10% fetal bovine serum (FBS) and 1% penicillin-streptomycin, were first seeded into a BD Falcon Primaria tissue culture dish (100 mm x 20 mm) and were cultured aseptically at 37°C and 5% CO_2 in a humidified incubator; (2) Cells were allowed to grow to at least 70% confluence in a 100 mm x 20 mm petri dish. At the end of incubation, the culture medium was gently aspirated and then the cells were washed twice with 5 ml Dulbecco's Phosphate Buffered Saline (DPBS); (3) After their careful washing with DPBS, the cell culture was passaged, by incubating the cells with a 1 ml 0.05% Trypsin-EDTA solution at 37°C, until the cells attained a rounded morphology, followed by resuspension of the detached cells, by adding 4 ml DMEM supplemented with 10% FBS and 1% penicillin-streptomycin, and centrifugation for 5 minutes at 500 g; (4) Following the centrifugation, trypsin and DPBS were aspirated and then the cell pellets were resuspended, by adding a 3 ml clear cell culture medium of DMEM without 10% FBS; (5) Replating a 1 mL suspension of the cells from step 4 into a 35 mm petri dish; then the cells were cultured for an additional 24 hours at 37°C and 5% CO_2 in a humidified incubator, thus allowing cells to attach to the surface of a new petri dish, prior to initiating treatment with the RGD peptide-conjugated gold nanosnakes.

3.3.10 Cellular Incubation with RGD Peptide-conjugated Gold Nanosnakes

The following procedure was used to incubate Human HeLa 229 cells with RGD peptide-conjugated gold nanosnakes. (1) A stock solution of RGD-conjugated gold nanosnakes was mixed with Dulbecco's modified Eagle medium (DMEM 11995) without 10% fetal bovine serum (FBS), to achieve a new suspension of gold nanosnakes with an OD of 1 at the given LSPR; (2) A 35 mm petri dish containing the HeLa cells designated for an imaging test was aspirated of its original culture medium, which was followed by washing the cells twice with 1 ml of Dulbecco's Phosphate Buffered Saline (DPBS); (3)

Thereafter, a 1 mL suspension of RGD-conjugated gold nanosnakes from step 1 was added to cells and the cells were incubated for 12 hours at 37°C and 5% CO_2 in a humidified incubator, for allowing cellular uptake of the nanosnake conjugates; (4) At the end of incubation, cells were washed with 1 ml 1X PBS buffer, three times, to remove free gold nanosnake conjugates in solution; (5) Cells were fixed onto a petri dish by adding 0.5 mL of fresh 4% paraformaldehyde in PBS for 15 min, followed by washing cells three times with 1 ml 1x PBS buffer; (6) Finally, 1 mL 1x PBS buffer was added to the petri dish and the cells were stored at 4°C before the optical imaging analysis.

3.3.11 Dark-field Light Scattering Imaging

The dark-field light scattering images were recorded using an inverted Nikon Epiphot 200 microscope equipped with an incandescent tungsten-halogen lamp (100 W) as a white light source. In order to acquire high-quality images, a high numerical aperture (NA > 0.55) is necessary. Therefore, a Nikon long working distance (f = 8 mm) 50x air immersion objective lens, with a numerical aperture of 0.55, was used to focus the incident light from the tungsten-halogen lamp onto the samples, and also to collect only the scattered light from the samples. The dark-field light scattering pictures of the cells were captured by using a Nikon digital sight DS-Fi1 camera with an exposure time of 2 seconds. Under this dark-field light scattering microscope, intense colors of orange should be clearly seen to spread out in the human HeLa 229 cells, due to the intense light scattering of the internalized gold nanosnakes with an LSPR at 640 nm.

3.3.12 Cell Toxicity Experiments (MTT)

The MTT (3-(4,5- dimethylthiazol-2-yl)-2,5-diphenyltetrazolium bromide) assay is employed as a way of measuring whether any stress is placed on the cells by being in the presence of the nanosnakes. By use of a 96-well plate, 5000 cells (HeLa, MDA-MB-231, BE(2)-C) were plated onto each well in 100 µL of Dulbecco's Modified Eagle Media pH 7.4 (DMEM). The cells were incubated for 24 hrs, to ensure adhesion to the plate. For each cell line, a gold nanosnake sample with LSPR at 640 nm was added to five wells, at mass concentrations of 0.025, 0.05, 0.125, and 0.25 mg/mL, with an adjusted volume of 200 µL

for all wells. A control sample was made for each cell line, without any NP treatment. After an additional 24 hrs of incubation, 20 µL of a 0.5 mg/mL solution of the MTT dye in PBS was added to each well. After 3 hrs, the media was removed and replaced with 200 µL of dimethyl sulfoxide (DMSO). The plate was transferred to an Anthos 2010 plate reader and scanned at 550 nm excitation. To calculate the viability, the raw data for each nanosnake mass concentration were averaged (n = 5), so as to reduce random error. The percent viability was normalized by dividing the average values for each nanosnake mass concentration by the control average value. Error bars were determined from the compound standard deviation of the five trials for each sample.

3.4 Results and Discussion

3.4.1 Synthesis and Physical Characterization of Au Nanosnakes

Starting from 20 nm Au NP monomers having virgin surfaces, gold nanosnakes were synthesized as described in the Experimental Section. These gold nanosnakes display characteristic shifts in their UV-Vis absorption spectra (Figure 3.5), with a new secondary peak first emerging at approximately 590 nm, which can be tuned to 640+ nm, in addition to the fixed primary "monomer" 525 nm peak. The red-shifting of the UV-Vis spectra is caused by the nanosnakes' growth, which occurs over a period of up to 72 hours. The nanosnake solution exhibits changes in color over time, with images taken after quenching occurred at 2 (B), 5 (C), 10 (D), 27 (E), and 72 (F) hours after nanosnake assembly initialization.

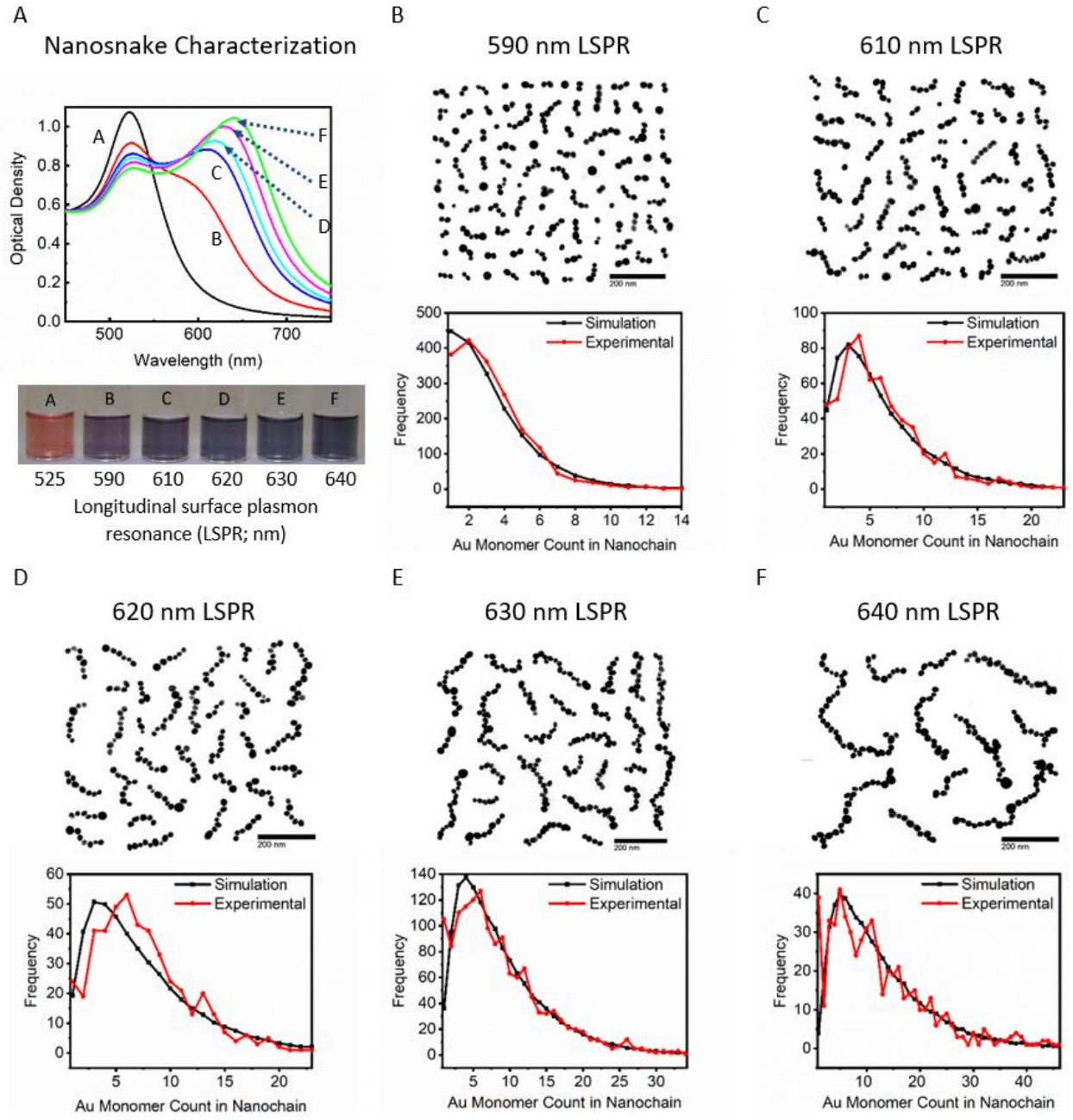

Figure 3.5 A.) (Top) UV-Vis spectra of Au nanosnakes and (bottom) color images for each sample: 525 nm (monomer); 590 – 640 nm LSPR peaks (nanosnakes). B-F.) (Top) Compositive TEM images of gold nanosnakes with LSRP peaks ranging from 590 to 640 nm. (Bottom) Nanochain distributions as determined from TEM images (red) and from 3D Monte Carlo simulation (black), where the simulation

chain-end-unit/chain-center-unit sticking probability is 3.3:1, an optimal value determined from the simulation fits to the experimental results.

The stability of the Au nanosnakes (the shelf-life) was tested by comparing the UV-Vis spectra immediately after the 640 nm LSPR synthesis to the UV-Vis spectra at 1, 2, and 4 months after synthesis, under room temperature storage conditions. As Figure 3.6 shows, no substantial change in the UV-Vis spectra occurs, indicating that the sample exhibits long-term stability.

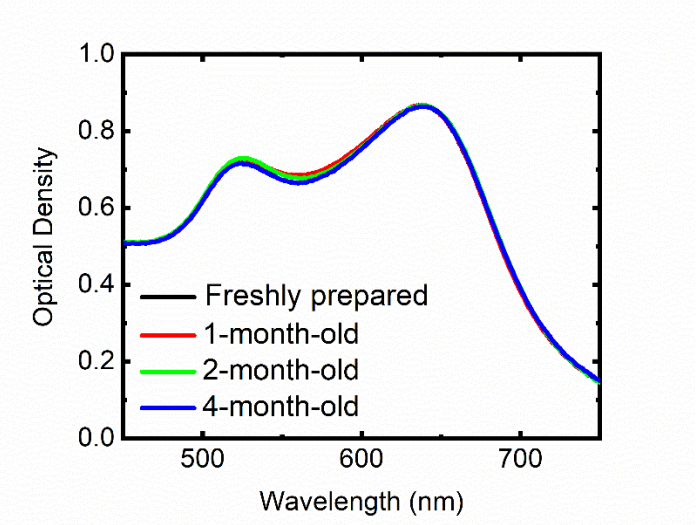

Figure 3.6 UV-Vis spectra of 640 nm Au nanosnakes immediately after preparation, and 1, 2, and 4 months after preparation. The black line cannot be seen, as it lies behind the red line. The UV-Vis spectra do not significantly change, indicating that the nanosnake sample integrity is maintained.

To better characterize the nanosnake samples, solutions with a 590, 610, 620, 630 and 640 nm LSPR were deposited on TEM grids for size analysis. Due to the low sample grid density, a combined image of TEM crops (single nanosnakes were aggregated into a single image) is given for every sample in Figure 3.5. As the LSPR of the nanosnakes shifts towards the red end of the spectrum, the correlated chain distribution is clearly shown to grow bigger, with longer chains becoming more common.

3.4.2 Monte-Carlo Computer Simulations of Nanosnake Formation

To model the growth of the nanosnakes, Monte Carlo simulations were run, utilizing a starting monomer density of 10^{-3} (monomers/total lattice sites number) and an applied sticking ratio of 3.3:1 between the center and the end of the chain, with the starting number of monomers derived from the experiment (Figures 3.5 and 3.7).

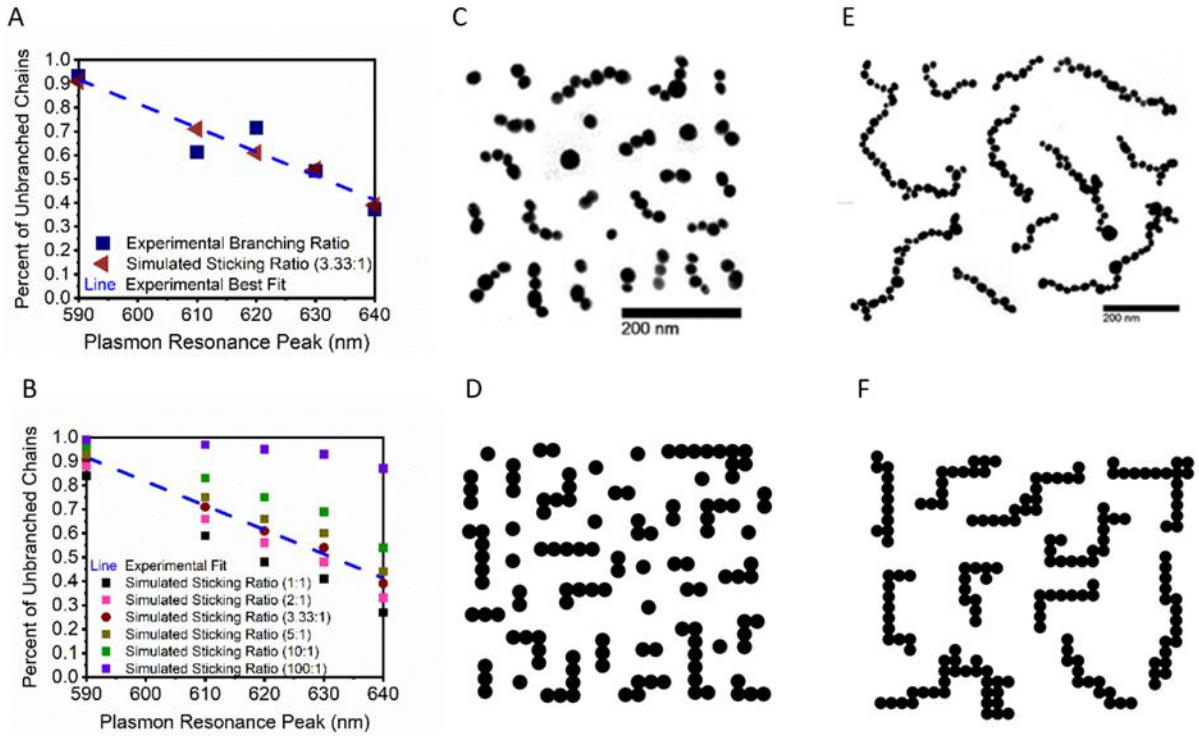

Figure 3.7 A.) Experimental branching percentages (% unbranched, snake-like linear chains) determined via TEM imaging of single nanochains for 590-640 nm (dark blue) LSPR samples (n>200 per sample), the best fit of the experimental data (dashed blue line; $R^2 = 0.87$), and Monte Carlo simulation results using a sticking ratio of 0.3 for non-end ("center") chain components (3.3:1 sticking preference of end-over-middle sticking). B.) Simulated branching results (% of unbranched chains) for various ratios of end-over-middle sticking (1:1, 2:1, 3.3:1, 5:1, 10:1, 100:1). Out of these samples, an end-over-middle sticking ratio of 3.3:1 has the lowest mean squared error (ratiometrically 53x, 11x, 1x, 8x, 59x, 418x respectively). C.) TEM morphology for the 590 LSPR nanosnake sample. D.) Monte Carlo morphology for the simulated 590

LSPR nanosnake sample using a 3.3: 1 sticking ratio (2D projection on square lattice). E.) TEM morphology for the 640 LSPR nanosnake sample. F.) Monte Carlo morphology for the simulated 640 LSPR nanosnake sample, using a 3.3:1 sticking ratio (2D projection on square lattice).

Overall, the distributions of the experimental nanosnake lengths (number of Au monomer units in snake) highly matches the simulated distributions when a 3.3:1 sticking ratio is utilized (Figure 3.5). Furthermore, the morphologies of the nanosnakes look highly similar to the Monte Carlo morphologies. As an example, the TEM morphologies of the nanosnakes (590 and 640 LSPR) are shown in Figures 7c and 7e, with the comparable Monte Carlo simulations in Figures 7d and 7f. Overall, the Monte Carlo simulations provide an important insight into the chemical nature of the synthetic method used, where attachment to chain-"*end* units" is favored over attachment to chain "*center* units", the ones with more than one nearest neighbor; the latter units seem to be better shielded towards chemical attachment (3-4 times more than the *end* units), thus accounting for the formation of gold nanosnakes rather than producing Au NP globules. The biased sticking probability (3.3:1 ratio) for chain-*end* units means that the aggregation process cannot simply occur from a model of diffusion limited cluster aggregation (DLCA), where a non-biased sticking probability (1:1 ratio) would be expected. Instead, this aggregation process is likely due to a combination of diffusion and dipole-dipole forces, where dipole moments form at the ends of the nanochain and drive preferential sticking, similar to that in the case of previously reported nano-metals.[36,75,76]

3.4.3 Simulation of the Optical Extinction Spectra of Gold Nanosnakes

In the field of nanochain plasmonics, a large challenge has been to relate UV-Vis spectra quantitively to TEM distributions.[77] Indeed, quantitatively establishing a clear correlation between TEM and UV-Vis data faces large challenges: 1.) Chains should have few branches, and disordered aggregation should be avoided when depositing samples onto TEM grids.[77] 2.) A quantitative correlation relating TEM distributions to UV-Vis spectra requires all the UV-Vis elements from within the TEM distribution

(monomer, dimer, trimer, etc.) to be known. Because the nanosnakes synthesized in this work are highly linear, the first issue of quantitative correlation can be overcome by depositing samples onto TEM grids with low density. To help with the second issue, we have used the discrete dipole scattering (DDSCAT) package to compute the optical spectra of all the linear chains within the TEM distribution, as shown in Figure 3.8. Performing such DDSCAT computations is typically not feasible for long chain lengths (10+ monomers), as prior to this publication DDSCAT had not been parallelized to allow computations to be performed on multi-core computational clusters. To overcome this computation bottleneck, we developed a Python script to run DDSCAT on a Linux-based SLURM cluster, running such computations on up to 400 parallelized cores, where parallelization was split along excitation wavelength (350 – 800 nm). Hence, instead of a single core computing all the optical wavelengths so as to determine the optical extinction, each core only computed 1-2 wavelengths, thus accelerating computation time by approximately 2 orders of magnitude (approximately 100x).

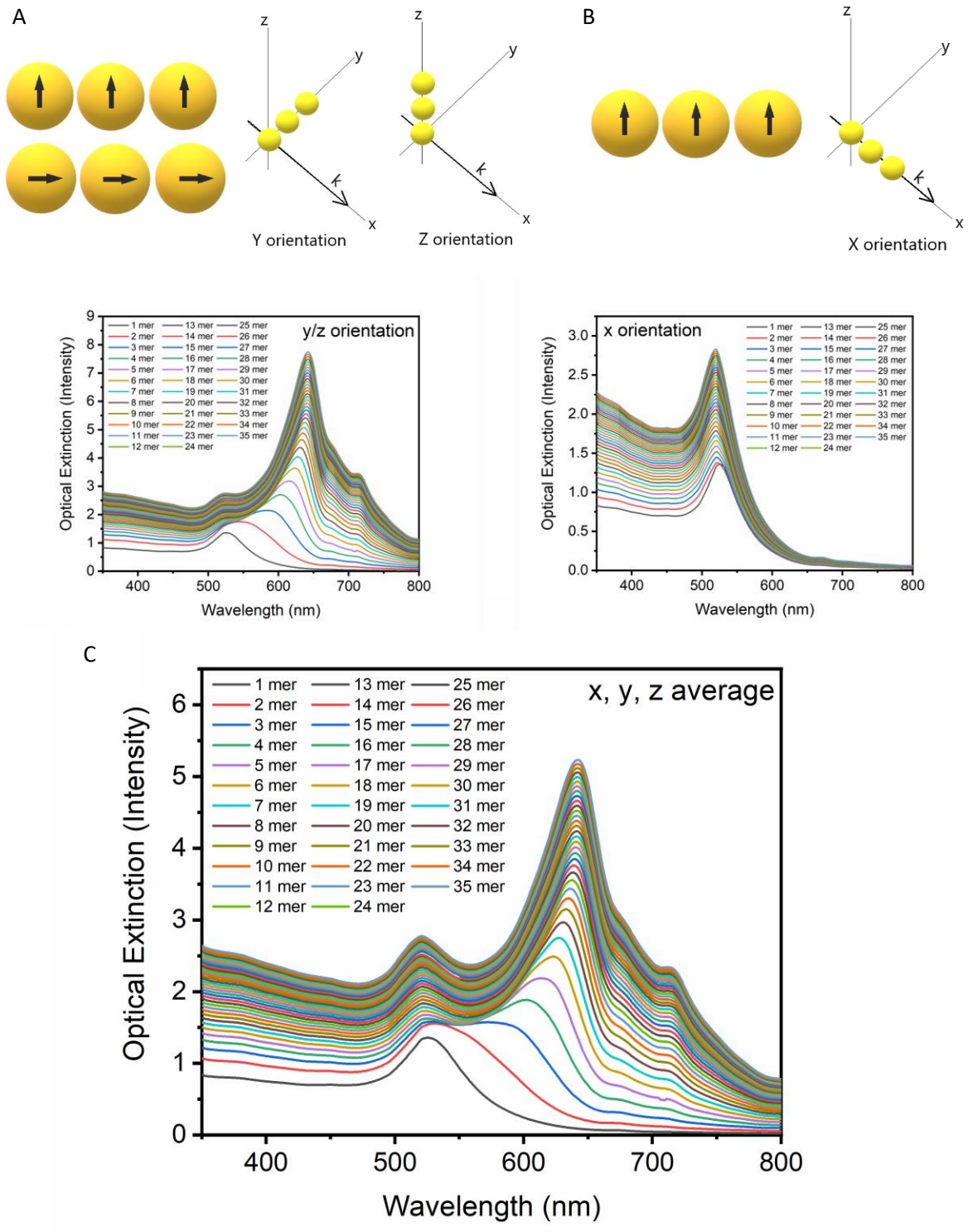

Figure 3.8 Optical extinction spectra computed for linear chains (up to 35 mer) assuming a 1.15 nm gap between monomers. A.) Linear extinction spectra along the y and z orientations. Both electric field

orientations of the incoming light (k vector) are averaged to simulate excitation from unpolarized light, with y orientation e-field vectors shown above. B.) Linear extinction spectra along the x orientation. Due to electric field symmetry, both electric field orientations lie transverse to the chain, so the LSPR shift is not observed. C.) Total spectra for 1.15 nm monomer-to-monomer linear chains from averaged x, y, and z orientations (equal weight along each orientation) for each chain length.

Utilizing a linear combination of chains and their frequencies from the TEM distributions, spectra were weighted and a combined spectrum was generated (Figure 3.9). The gap distance (distance between monomers) is an important parameter that determines the spectral properties of the nanosnakes. Due to the gap distances being less than 2 nm, determining accurate distances experimentally is challenging. Hence, for the simulations performed, we tested whether we could predict the gap distance via DDA. To do so, the mean squared error value (Equation 3.2 in Methods) was determined for each spacing between 0.75 – 4.00 nm, so as to determine the best fit. Overall, a 1.15 nm gap distance gave the best average fit, among all the samples (Figure 3.9). The spectrum generated from the simulation is compared to each respective experimental spectrum, as shown in Figure 3.9.

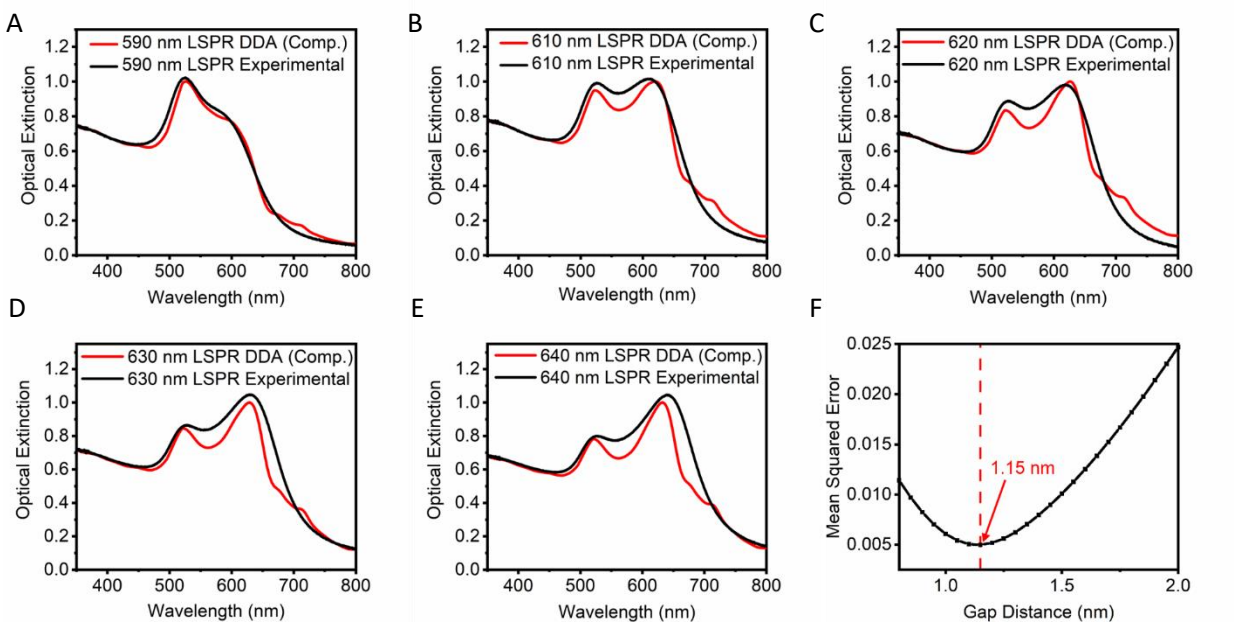

Figure 3.9 (A-E.) Computationally generated (red curve) and experimental (black curve) optical extinction spectra for samples with LSPR ranging from 590 nm to 640 nm utilizing chain length distributions determined by TEM and a gap distance of 1.15 nm. F.) The mean squared error (MSE) as a function of gap distance between simulated and experimental spectra. A gap distance of 1.15 nm is found to have the smallest mean squared error.

Within each spectrum we can see both a transverse SPR mode (near 520 nm) and an LSPR mode (590+ nm). Overall, both the DDA transverse SPR and the LSPR mode closely match the experimental results. In addition to determining the extinction coefficient for each sample, the absorption and scattering contributions to the extinction coefficient were also calculated in DDSCAT, using a 1.15 nm gap distance, as shown in Figure 3.10. Of high importance is the following observation: As the length of a linear cluster of Au NPs grows longer, the scattering contribution to the extinction coefficient substantially grows (from a 0.8% contribution in the monomer to a 16% contribution in the 640 nm LSPR sample). This increased scattering cross-section of approximately 40x enhancement in scattering amplitude is a major advantage of using gold nanosnakes as probes in scattering-based imaging, like dark-field optical microscopy.

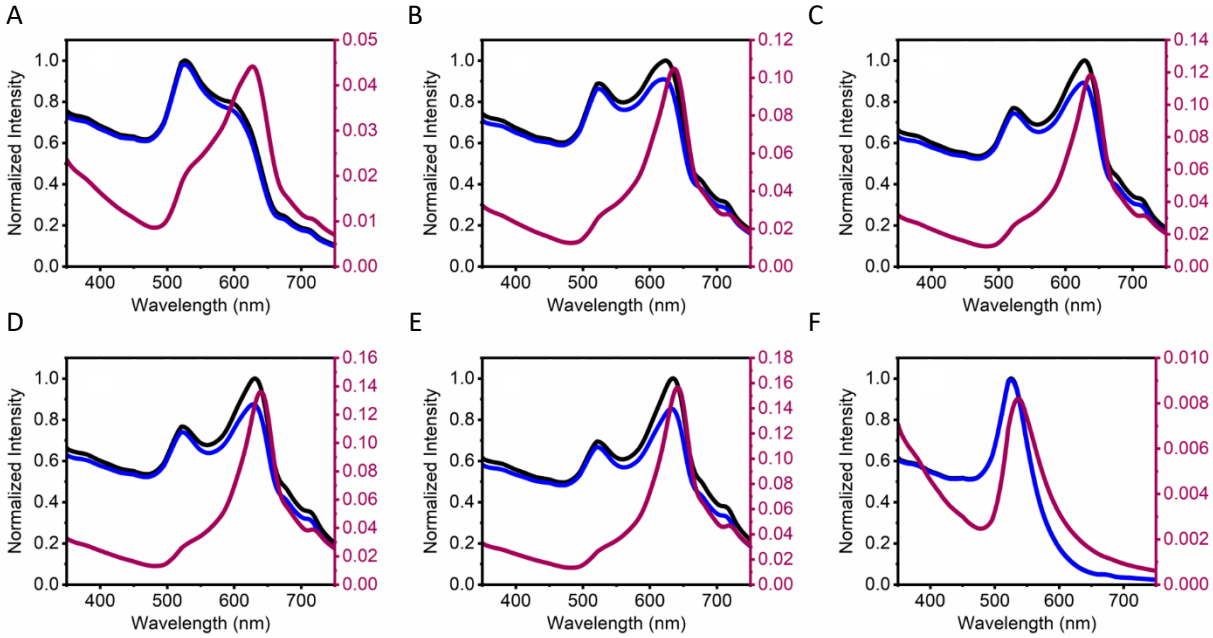

Figure 3.10 Relative components of absorption (blue; left axis) and scattering (purple; right axis) that compose the extinction spectra (black; left axis) for each sample, A: 590 nm LSPR, B: 610 nm LSPR, C: 620 nm LSPR, D: 630 nm LSPR, E: 640 nm LSPR, F: 525 nm (monomer) plasmon resonance maxima, determined via DDSCAT simulation using 1.15 nm gap distance. As chain length grows, the scattering contribution to the extinction coefficent grows rapidly (a shift from 0.8% contribution (monomer) to 16% contribution

occurs). In terms of maximum scattering intensity compared to the maximum monomer scattering intensity, scattering amplitiude increases by 6.92x, 20.2x, 24.77x, 29.27x, and 39.45x respectively (590 nm, 610 nm, 620 nm, 630 nm, 640 nm LSPR). For the monomer sample (F), the black line (extinction) is hidden behind the blue line (absorption) due to their close overlap.

To verify the accuracy of the predicted gold nanosnake gap distance via DDA calculation, we measured this distance experimentally using high resolution transmission electron microscopy, as shown in Figure 3.11.

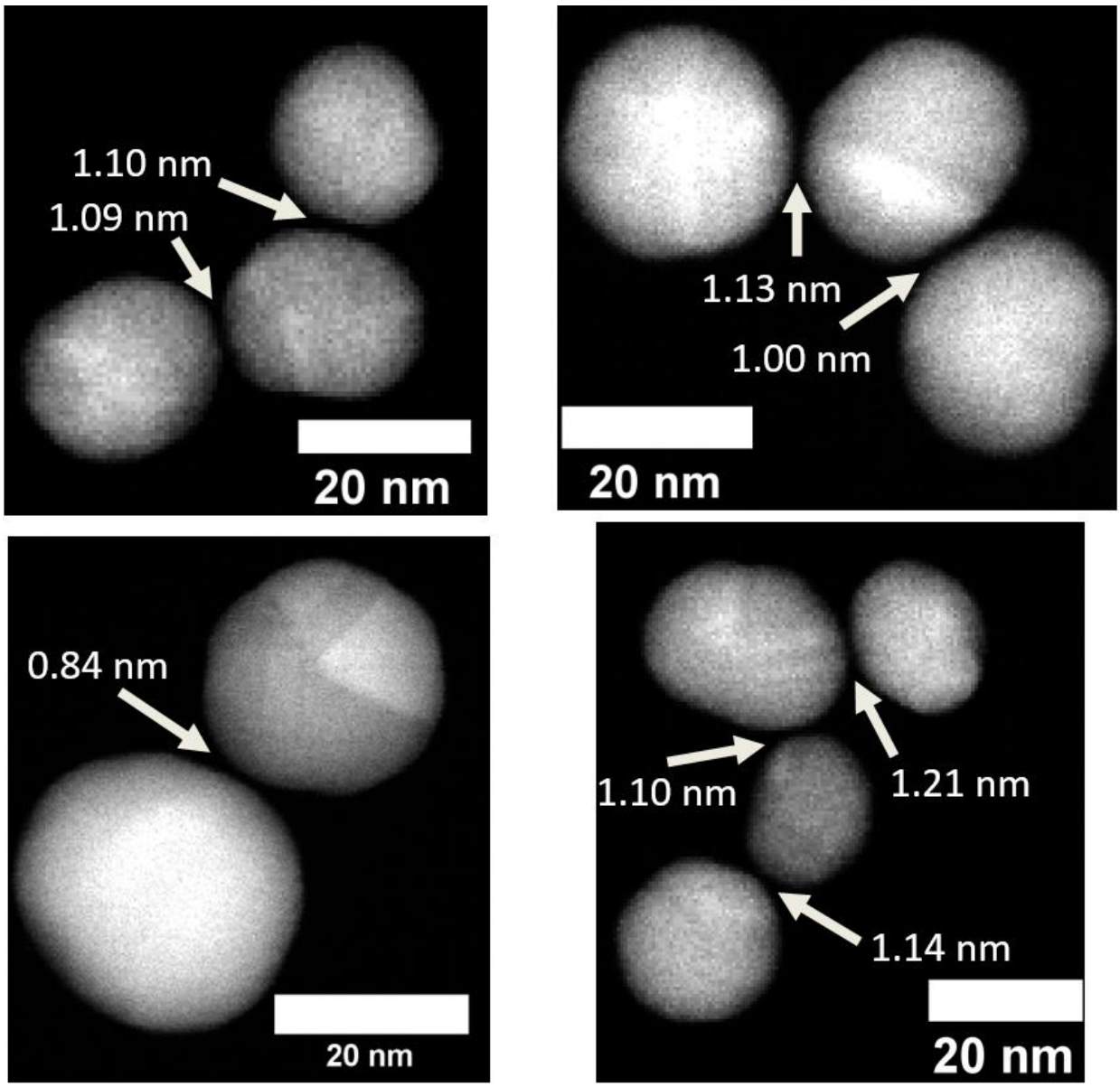

Figure 3.11 High-resolution TEM images of Au nanosnakes, revealing narrow gap distances (0.80 – 1.25 nm), with an average gap distance of 1.08 nm ± 0.11 nm. Gap distance average standard deviation between measurements (n=3) was 0.062 nm.

The gap distance obtained from the high resolution TEM data lies between 0.80 to 1.25 nm, with an average gap distance at 1.08 nm ± 0.11 nm, in excellent agreement with the DDA predicted value of 1.15 nm.

3.4.4 Dark-field Light Scattering Microscopy and MTT Cytotoxicity Assay

With the optical properties of the gold nanosnakes characterized, RGD peptide-conjugated gold nanosnakes, with an LSPR at 640 nm, were incubated with HeLa cancer cells and then imaged under dark-field optical microscopy (Figure 3.12B). The gold nanosnakes with LSPR at 640 nm were selected for being used in the dark-field optical imaging because they have the reddest excitation wavelength (deeper penetration depths) and highest maximum scattering cross-section among all samples. RGD peptide-conjugated Au NP monomers (surface plasmon resonance at about 525 nm) were also incubated with HeLa cancer cells, as a control for comparing image properties (Figure 3.12A). As shown in Figure 3.12, HeLa cancer cells stained with Au NP monomers and gold nanosnakes appear green and orange, respectively, under dark-field optical microscopy. This is because the surface plasmon resonance of the gold nanostructures determines the image color when they are used as contrast agents in dark-field light scattering imaging.

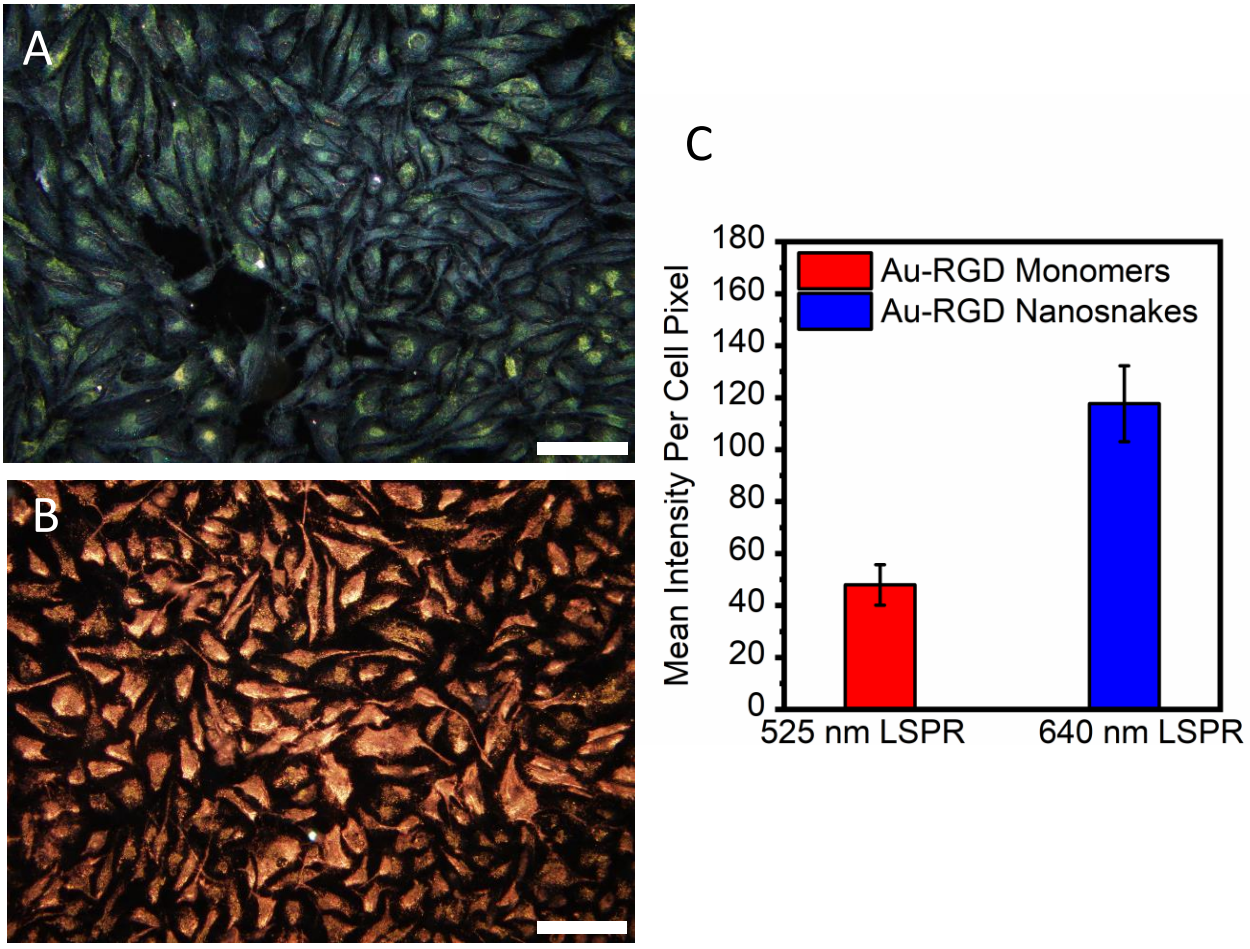

Figure 3.12 Dark-field light scattering images of human HeLa cancer cells stained with (A) 20 nm RGD peptide-conjugated Au NP monomers and (B) RGD peptide-conjugated Au nanosnakes with LSRP at 640 nm. The scale bar is 100 µm. (C). Mean intensity per cell pixel (n = 12 cells) for HeLa cells incubated with 20 nm RGD-conjugated Au monomers and RGD-conjugated 640 nm LSPR nanosnakes (equal incubation masses).

Overall, for individual cells within each image, the Au monomers incubated cells have a mean intensity per pixel of 48.0 ± 7.78 and the Au nanosnake incubated cells have a mean intensity per pixel of 118 ± 14.5 (Figure 3.12C), revealing that the Au nanosnakes have a 2.46x ± 0.50x greater mean scattering intensity per Au nanosphere, compared to the Au monomer nanospheres. The scattering increase from the Au nanosnakes, by a factor of 2.46 ± 0.50, reveals the functional benefits of Au nanosnakes for dark

field imaging, as equal masses of gold (equivalent masses of gold nanospheres) were added for both the Au nanosnake and the Au monomer samples during cell incubation. This enhancement by about 2.5 also closely resembles the predicted DDA per nanosphere enhancement value of 3.35 ± 0.55 (Figure 3.13), and may be a bit smaller due to a somewhat less efficient uptake of the larger Au NPs by the HeLa cells. Note that Albanese et. al. show that Au NPs on the scale of 20 nm are 20-30% better uptaken than larger Au aggregates (on the 100 nm scale).[78]

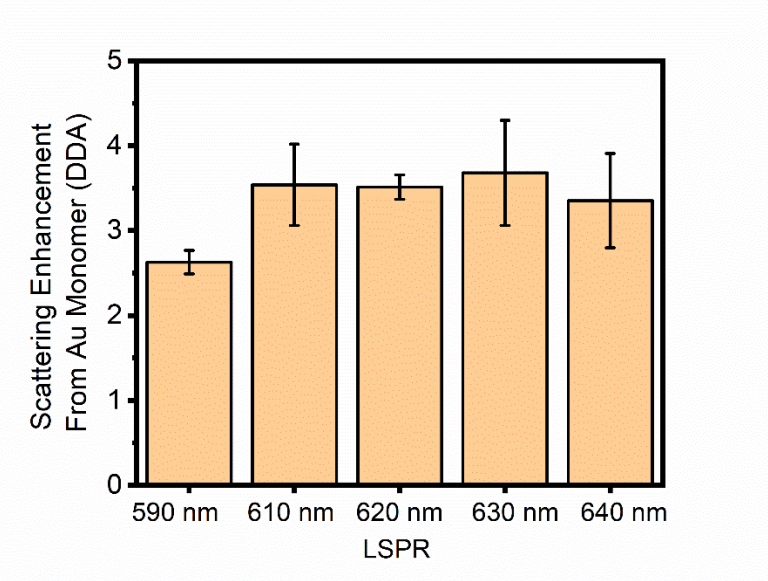

Figure 3.13 Computed (DDA) scattering enhancement for 590 nm, 610 nm, 620 nm, 630 nm, and 640 nm LSPR nanosnakes under excitation from a tungsten halogen (500 – 700 nm excitation) lamp per nanosphere as compared to a 20 nm Au monomer (525 nm LSPR).

Applying gold nanosnakes as imaging contrast agents presents multiple advantages. Foremost, because the LSPR of the gold nanosnakes is tunable, optical imaging at a selected wavelength, avoiding background from cell scattering or other scattering/fluorescent dyes, is possible. Second, images with high brightness could be acquired using gold nanosnakes, because of the highly enhanced scattering cross section relative to that of the NP monomer. Third, it is advantageous to tune the gold nanosnake optical properties (absorption, scattering) into the near-infrared for studying thick cell layers (> 1 μm) or for

performing *in vivo* imaging, because near-infrared light travels deeper into tissue, by a factor of 10-100x, compared to bluer light, with much lower background fluorescence.[79] Fourth, the gold nanosnakes synthesized here can be easily conjugated with active targeting moieties, like the RGD peptide shown in Figure 3.12, for *in vitro* and, most importantly, for *in vivo* targeting. Fifth, the gold nanosnakes have intense electric field hotspots between monomers (Figure 3.14) which can serve to enhance near-field coupling with fluorescent dyes, currently of immense interest in super resolution, single molecule, and SERS microscopy.[80–84]

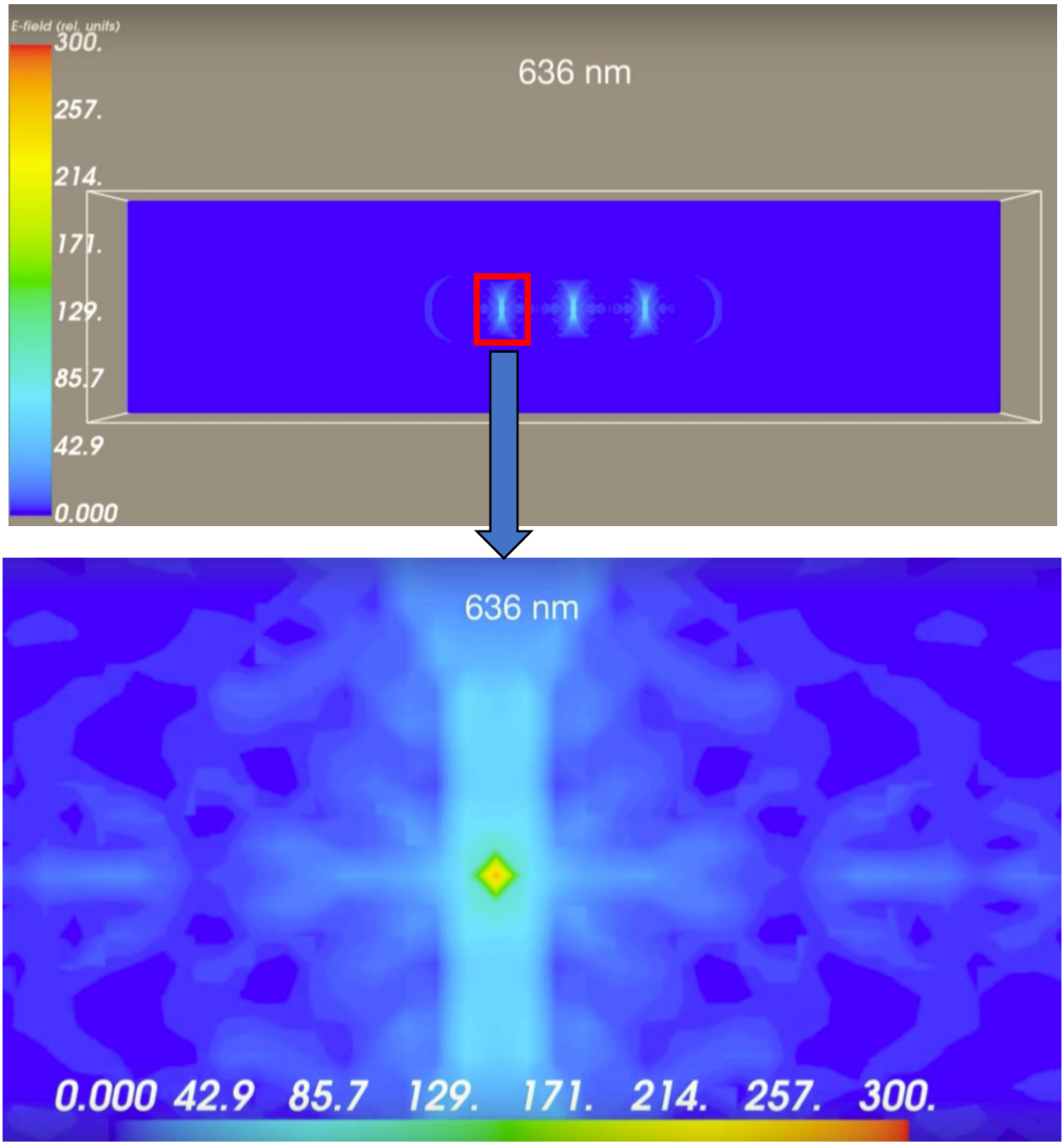

Figure 3.14 Electric field distribution of gold nanochain tetramer (4-mer) with 1 nm gap, determined via DDSCAT simulation at 636 nm excitation (maximum of tetramer optical extinction from DDA simulation), where light travels along the y-axis. The E-field intensity axis is scaled to relative units between 0-300 (units are in V/cm assuming excitation field with 1 V/cm). The figure shows that between the nanochain

gaps, intense electric field hotspots exist. For longer chains, electric field intensity will increase in the gap regions.

Furthermore, biocompatibility was tested for the nanosnake sample on 3 different cancer cell types (breast cancer, cervical cancer, brain cancer), up to a mass concentration as high as 0.25 mg/mL, via MTT assay. Overall, no statistically significant cell toxicity from the gold nanosnakes was observed (Figure 3.15).

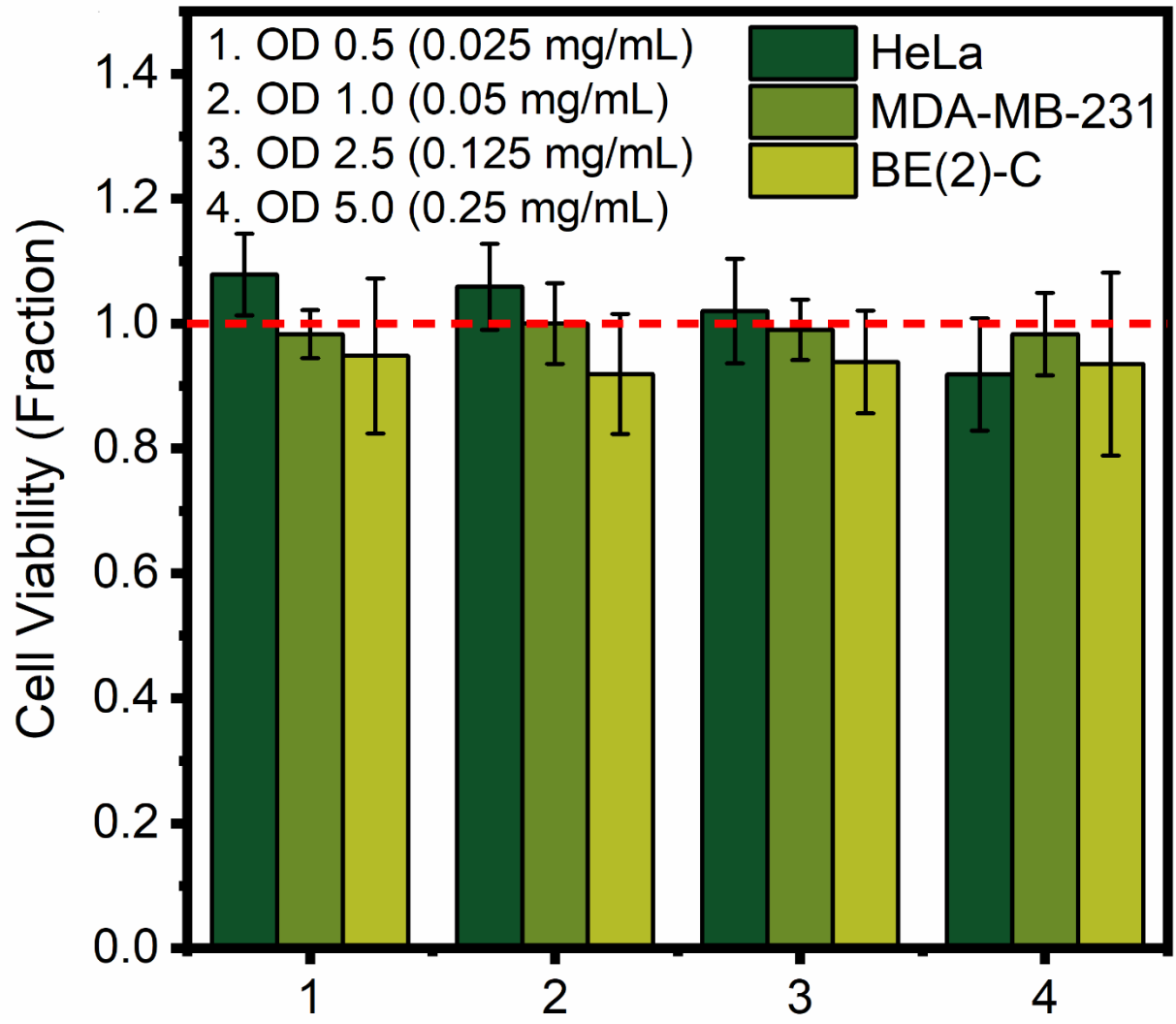

Figure 3.15 MTT assay under gold nanosnake (LSPR at 640 nm) incubation for HeLa (cervical cancer), MDA-MB-231 (breast cancer), and BE(2)-C (neuroblastoma) cells, for ODs between 0.5 – 5.0 (0.025 mg/mL –

0.25 mg/mL NP mass concentration), revealing that the gold nanosnakes are biocompatible, i.e., show no statistically significant cell toxicity effects.

The MTT result reveals that the nanosnake system is well-suited for a variety of bio-imaging applications, as across a variety of cell lines there are no significant toxicity effects. In addition, these cancer cell targeted gold nanosnakes could potentially serve as carriers of photosensitizers for photodynamic therapy and as agents for plasmonic photothermal therapy.[11,12,85]

3.5 Conclusion

We describe a facile and novel method for a well-controlled and selective synthesis, accompanied by careful characterization, of a highly-linear, spectrally tunable, and biocompatible gold nanosnakes system, made of nanospheres separated by gap distances less than 2 nm. Utilizing ensemble statistics of the nanosnake lengths, determined by a TEM image analysis, DDA calculations reproduced well the experimental optical absorption spectra for all the fabricated nanosnake samples. Monte-Carlo simulations provide an interesting insight into the selectivity of the specialized chemical synthesis, revealing that the *chain-end* units of these linear clusters of Au NPs are about 3-4 times more reactive than their *center* units; thus gold nanosnakes (highly linear gold nanochains), rather than globular assemblies, are formed. It is this linear assembly that enables the spectral tunability property of the gold nanosnakes, and this tunability is of high potential for various biomedical applications. Furthermore, these nanosnakes show no cytotoxicity, and they can also be easily conjugated with targeting moieties, such as the RGD peptide, for targeted therapy applications. Future research on these nanosnake systems may proceed along three directions: 1.) Batch synthesizing and characterizing longer nanosnakes with LSPR up to 750 nm (small scale synthesis has been successful but the method is currently being optimized); 2.) Exploring how the molar ratio between the CALNN peptides and the cysteamine molecules attached onto the surfaces of the Au NPs affects the growth of the nanosnakes, the nanochain gap distance (smaller gaps are more desirable as the nanosnake will have redder spectral shifts), and the chain-branch

formation; 3.) Utilizing these nanosnakes for additional *in vitro* and *in vivo* studies. Overall, our results demonstrate that the Au NP nanosnake system exhibits many novel properties, including spectral tunability and intense scattering cross-sections; we thus expect them to be utilizable for a variety of photonic and biomedical applications, such as dark-field and X-ray imaging, as well as targeted theranostic modalities.

3.6 References

(1) Boisselier, E.; Astruc, D. Gold Nanoparticles in Nanomedicine: Preparations, Imaging, Diagnostics, Therapies and Toxicity. *Chem. Soc. Rev.* **2009**, *38* (6), 1759–1782. https://doi.org/10.1039/b806051g.

(2) Chemla, Y.; Betzer, O.; Markus, A.; Farah, N.; Motiei, M.; Popovtzer, R.; Mandel, Y. Gold Nanoparticles for Multimodal High-Resolution Imaging of Transplanted Cells for Retinal Replacement Therapy. *Nanomedicine* **2019**, *14* (14), 1857–1871. https://doi.org/10.2217/nnm-2018-0299.

(3) Song, J.; Qu, J.; Swihart, M. T.; Prasad, P. N. Near-IR Responsive Nanostructures for Nanobiophotonics: Emerging Impacts on Nanomedicine. *Nanomedicine Nanotechnology, Biol. Med.* **2016**, *12* (3), 771–788. https://doi.org/10.1016/j.nano.2015.11.009.

(4) Qian, W.; Curry, T.; Che, Y.; Kopelman, R. Targeted Delivery of Peptide-Conjugated Biocompatible Gold Nanoparticles into Cancer Cell Nucleus. *Colloid. Nanocrystals Biomed. Appl. VIII* **2013**, *8595*, 85951D. https://doi.org/10.1117/12.2005328.

(5) Zhao, Y.; Huang, Y.; Zhu, H.; Zhu, Q.; Xia, Y. Three-in-One: Sensing, Self-Assembly, and Cascade Catalysis of Cyclodextrin Modified Gold Nanoparticles. *J. Am. Chem. Soc.* **2016**, *138* (51), 16645–16654. https://doi.org/10.1021/jacs.6b07590.

(6) Qin, L.; Zeng, G.; Lai, C.; Huang, D.; Xu, P.; Zhang, C.; Cheng, M.; Liu, X.; Liu, S.; Li, B.; et al. “Gold Rush” in Modern Science: Fabrication Strategies and Typical Advanced Applications of Gold Nanoparticles in Sensing. *Coord. Chem. Rev.* **2018**, *359*, 1–31. https://doi.org/10.1016/j.ccr.2018.01.006.

(7) Alim, S.; Vejayan, J.; Yusoff, M. M.; Kafi, A. K. M. Recent Uses of Carbon Nanotubes & Gold Nanoparticles in Electrochemistry with Application in Biosensing: A Review. *Biosens. Bioelectron.* **2018**, *121* (August), 125–136. https://doi.org/10.1016/j.bios.2018.08.051.

(8) Singh, P.; Pandit, S.; Mokkapati, V. R. S. S.; Garg, A.; Ravikumar, V.; Mijakovic, I. Gold Nanoparticles in Diagnostics and Therapeutics for Human Cancer. *Int. J. Mol. Sci.* **2018**, *19* (7). https://doi.org/10.3390/ijms19071979.

(9) Lohse, S. E.; Murphy, C. J. Applications of Colloidal Inorganic Nanoparticles: From Medicine to Energy. *Journal of the American Chemical Society*. **2012**, 134 (38), 15607–15620. https://doi.org/10.1021/ja307589n.

(10) Lopes, T. S.; Alves, G. G.; Pereira, M. R.; Granjeiro, J. M.; Leite, P. E. C. Advances and Potential Application of Gold Nanoparticles in Nanomedicine. *J. Cell. Biochem.* **2019**, *120* (10), 16370–16378. https://doi.org/10.1002/jcb.29044.

(11) Giljohann, D. A.; Seferos, D. S.; Daniel, W. L.; Massich, M. D.; Patel, P. C.; Mirkin, C. A. Gold Nanoparticles for Biology and Medicine. *Angew. Chemie - Int. Ed.* **2010**, *49* (19), 3280–3294. https://doi.org/10.1002/anie.200904359.

(12) Wang, J.; Zhu, G.; You, M.; Song, E.; Shukoor, M. I.; Zhang, K.; Altman, M. B.; Chen, Y.; Zhu, Z.; Huang, C. Z.; Tan W. Assembly of Aptamer Switch Probes and Photosensitizer on Gold Nanorods for Targeted Photothermal and Photodynamic Cancer Therapy. *ACS Nano* **2012**, *6* (6), 5070–5077. https://doi.org/10.1021/nn300694v.

(13) Dreaden, E. C.; Alkilany, A. M.; Huang, X.; Murphy, C. J.; El-Sayed, M. A. The Golden Age: Gold

Nanoparticles for Biomedicine. *Chemical Society Reviews*. **2012**, 7, 2740–2779. https://doi.org/10.1039/c1cs15237h.

(14) McLean, A.; Wang, R.; Huo, Y.; Cooke, A.; Hopkins, T.; Potter, N.; Li, Q.; Isaac, J.; Haidar, J.; Jin, R.; Kopelman R. Synthesis and Optical Properties of Two-Photon-Absorbing Au25(Captopril)18-Embedded Polyacrylamide Nanoparticles for Cancer Therapy. *ACS Appl. Nano Mater.* **2020**, *3* (2), 1420–1430. https://doi.org/10.1021/acsanm.9b02272.

(15) Gharib, M.; Khalaf, M.; Afroz, S.; Feliu, N.; Parak, W. J.; Chakraborty, I. Sustainable Synthesis and Improved Colloidal Stability of Popcorn-Shaped Gold Nanoparticles. *ACS Sustain. Chem. Eng.* **2019**, *7* (11), 9834–9841. https://doi.org/10.1021/acssuschemeng.9b00295.

(16) Jimenez De Aberasturi, D.; Serrano-Montes, A. B.; Langer, J.; Henriksen-Lacey, M.; Parak, W. J.; Liz-Marzán, L. M. Surface Enhanced Raman Scattering Encoded Gold Nanostars for Multiplexed Cell Discrimination. *Chem. Mater.* **2016**, *28* (18), 6779–6790. https://doi.org/10.1021/acs.chemmater.6b03349.

(17) Chen, Y.; Wu, H.; Li, Z.; Wang, P.; Yang, L.; Fang, Y. The Study of Surface Plasmon in Au/Ag Core/Shell Compound Nanoparticles. *Plasmonics* **2012**, *7* (3), 509–513. https://doi.org/10.1007/s11468-012-9336-6.

(18) Bai, X.; Wang, Y.; Song, Z.; Feng, Y.; Chen, Y.; Zhang, D.; Feng, L. The Basic Properties of Gold Nanoparticles and Their Applications in Tumor Diagnosis and Treatment. *International Journal of Molecular Sciencies* **2020**, 21 (7), 2480.

(19) Zhao, P.; Li, N.; Astruc, D. State of the Art in Gold Nanoparticle Synthesis. *Coord. Chem. Rev.* **2013**, *257* (3–4), 638–665. https://doi.org/10.1016/j.ccr.2012.09.002.

(20) Zhang, D.; Gökce, B.; Barcikowski, S. Laser Synthesis and Processing of Colloids: Fundamentals and Applications. *Chem. Rev.* **2017**, *117* (5), 3990–4103. https://doi.org/10.1021/acs.chemrev.6b00468.

(21) Taylor, R. W.; Lee, T. C.; Scherman, O. A.; Esteban, R.; Aizpurua, J.; Huang, F. M.; Baumberg, J. J.; Mahajan, S. Precise Subnanometer Plasmonic Junctions for SERS within Gold Nanoparticle Assemblies Using Cucurbit[n]Uril "Glue." *ACS Nano* **2011**, *5* (5), 3878–3887. https://doi.org/10.1021/nn200250v.

(22) Ghosh, S. K.; Pal, T. Interparticle Coupling Effect on the Surface Plasmon Resonance of Gold Nanoparticles: From Theory to Applications. **2007**, 107 (11), 4797-4862. https://doi.org/10.1021/cr0680282.

(23) Ashley, M. J.; Bourgeois, M. R.; Murthy, R. R.; Laramy, C. R.; Ross, M. B.; Naik, R. R.; Schatz, G. C.; Mirkin, C. A. Shape and Size Control of Substrate-Grown Gold Nanoparticles for Surface-Enhanced Raman Spectroscopy Detection of Chemical Analytes. *J. Phys. Chem. C* **2018**, *122* (4), 2307–2314. https://doi.org/10.1021/acs.jpcc.7b11440.

(24) Glotzer, S. C.; Solomon, M. J. Anisotropy of Building Blocks and Their Assembly into Complex Structures. *Nat. Mater.* **2007**, *6* (8), 557–562. https://doi.org/10.1038/nmat1949.

(25) Liu, K.; Nie, Z.; Zhao, N.; Li, W.; Rubinstein, M.; Kumacheva, E. Step-Growth Polymerization of Inorganic Nanoparticles. *Science.* **2010**, *329* (5988), 197–200. https://doi.org/10.1126/science.1189457.

(26) Yang, M.; Chen, G.; Zhao, Y.; Silber, G.; Wang, Y.; Xing, S.; Han, Y.; Chen, H. Mechanistic Investigation into the Spontaneous Linear Assembly of Gold Nanospheres. *Phys. Chem. Chem. Phys.* **2010**, *12* (38), 11850–11860. https://doi.org/10.1039/c0cp00127a.

(27) Ou, F. S.; Hu, M.; Naumov, I.; Kim, A.; Wu, W.; Bratkovsky, A. M.; Li, X.; Williams, R. S.; Li, Z. Hot-Spot Engineering in Polygonal Nanofinger Assemblies for Surface Enhanced Raman Spectroscopy. *Nano Lett.* **2011**, *11* (6), 2538–2542. https://doi.org/10.1021/nl201212n.

(28) Steiner, A. M.; Mayer, M.; Seuss, M.; Nikolov, S.; Harris, K. D.; Alexeev, A.; Kuttner, C.; König, T. A. F.; Fery, A. Macroscopic Strain-Induced Transition from Quasi-Infinite Gold Nanoparticle Chains

to Defined Plasmonic Oligomers. *ACS Nano* **2017**, *11* (9), 8871–8880. https://doi.org/10.1021/acsnano.7b03087.

(29) Matricardi, C.; Hanske, C.; Garcia-Pomar, J. L.; Langer, J.; Mihi, A.; Liz-Marzán, L. M. Gold Nanoparticle Plasmonic Superlattices as Surface-Enhanced Raman Spectroscopy Substrates. *ACS Nano* **2018**, *12* (8), 8531–8539. https://doi.org/10.1021/acsnano.8b04073.

(30) Sebastian, E. M.; Jain, S. K.; Purohit, R.; Dhakad, S. K.; Rana, R. S. Nanolithography and Its Current Advancements. *Mater. Today Proc.* **2019**, *26*, 2351–2356. https://doi.org/10.1016/j.matpr.2020.02.505.

(31) Wustholz, K. L.; Henry, A. I.; McMahon, J. M.; Freeman, R. G.; Valley, N.; Piotti, M. E.; Natan, M. J.; Schatz, G. C.; Duyne, R. P. V. Structure-Activity Relationships in Gold Nanoparticle Dimers and Trimers for Surface-Enhanced Raman Spectroscopy. *J. Am. Chem. Soc.* **2010**, *132* (31), 10903–10910. https://doi.org/10.1021/ja104174m.

(32) Wang, X.; Li, G.; Chen, T.; Yang, M.; Zhang, Z.; Wu, T.; Chen, H. Polymer-Encapsulated Gold-Nanoparticle Dimers: Facile Preparation and Catalytical Application in Guided Growth of Dimeric ZnO-Nanowires. *Nano Lett.* **2008**, *8* (9), 2643–2647. https://doi.org/10.1021/nl080820q.

(33) Lu, J.; Chang, Y. X.; Zhang, N. N.; Wei, Y.; Li, A. J.; Tai, J.; Xue, Y.; Wang, Z. Y.; Yang, Y.; Zhao, L.; Lu, ZY; Liu, K. Chiral Plasmonic Nanochains via the Self-Assembly of Gold Nanorods and Helical Glutathione Oligomers Facilitated by Cetyltrimethylammonium Bromide Micelles. *ACS Nano* **2017**, *11* (4), 3463–3475. https://doi.org/10.1021/acsnano.6b07697.

(34) Hussain, I.; Brust, M.; Barauskas, J.; Cooper, A. I. Controlled Step Growth of Molecularly Linked Gold Nanoparticles: From Metallic Monomers to Dimers to Polymeric Nanoparticle Chains. *Langmuir* **2009**, *25* (4), 1934–1939. https://doi.org/10.1021/la804207y.

(35) Polavarapu, L.; Xu, Q. H. A Single-Step Synthesis of Gold Nanochains Using an Amino Acid as a Capping Agent and Characterization of Their Optical Properties. *Nanotechnology* **2008**, *19* (7).

https://doi.org/10.1088/0957-4484/19/7/075601.

(36) Liao, J.; Zhang, Y.; Yu, W.; Xu, L.; Ge, C.; Liu, J.; Gu, N. Linear Aggregation of Gold Nanoparticles in Ethanol. *Colloids Surfaces A Physicochem. Eng. Asp.* **2003**, *223* (1–3), 177–183. https://doi.org/10.1016/S0927-7757(03)00156-0.

(37) Huang, C. C.; Huang, Y. F.; Cao, Z.; Tan, W.; Chang, H. T. Aptamer-Modified Gold Nanoparticles for Colorimetric Determination of Platelet-Derived Growth Factors and Their Receptors. *Anal. Chem.* **2005**, *77* (17), 5735–5741. https://doi.org/10.1021/ac050957q.

(38) Yong, K. T.; Swihart, M. T.; Ding, H.; Prasad, P. N. Preparation of Gold Nanoparticles and Their Applications in Anisotropic Nanoparticle Synthesis and Bioimaging. *Plasmonics* **2009**, *4* (2), 79–93. https://doi.org/10.1007/s11468-009-9078-2.

(39) Li, N.; Zhao, P.; Astruc, D. Anisotropic Gold Nanoparticles: Synthesis, Properties, Applications, and Toxicity. *Angew. Chemie - Int. Ed.* **2014**, *53* (7), 1756–1789. https://doi.org/10.1002/anie.201300441.

(40) Alkilany, A. M.; Nagaria, P. K.; Hexel, C. R.; Shaw, T. J.; Murphy, C. J.; Wyatt, M. D. Cellular Uptake and Cytotoxicity of Gold Nanorods: Molecular Origin of Cytotoxicity and Surface Effects. *Small* **2009**, *5* (6), 701–708. https://doi.org/10.1002/smll.200801546.

(41) Alkilany, A. M.; Shatanawi, A.; Kurtz, T.; Caldwell, R. B.; Caldwell, R. W. Toxicity and Cellular Uptake of Gold Nanorods in Vascular Endothelium and Smooth Muscles of Isolated Rat Blood Vessel: Importance of Surface Modification. *Small* **2012**, *8* (8), 1270–1278. https://doi.org/10.1002/smll.201101948.

(42) Wan, J.; Wang, J. H.; Liu, T.; Xie, Z.; Yu, X. F.; Li, W. Surface Chemistry but Not Aspect Ratio Mediates the Biological Toxicity of Gold Nanorods in Vitro and in Vivo. *Sci. Rep.* **2015**, *5*, 1–16. https://doi.org/10.1038/srep11398.

(43) Tserkezis, C.; Herrmann, L. O.; Valev, V. K.; Baumberg, J. J.; Aizpurua, J. Optical Response of

Threaded Chain Plasmons: From Capacitive Chains to Continuous Nanorods. *Opt. Express* **2014**, *22* (20), 23851. https://doi.org/10.1364/oe.22.023851.

(44) Lei, Y.; Yuan, M.; Yang, D.; Li, D. Unidirectional Light Scattering by up–down Janus Dimers Composed of Gold Nanospheres and Silicon Nanorods. *Opt. Commun.* **2019**, *435*, 362–366. https://doi.org/10.1016/j.optcom.2018.11.055.

(45) Ganjali, M.; Ganjali, M.; Vahdatkhah, P.; Marashi, S. M. B. Synthesis of Ni Nanoparticles by Pulsed Laser Ablation Method in Liquid Phase. *Procedia Mater. Sci.* **2015**, *11*, 359–363. https://doi.org/10.1016/j.mspro.2015.11.127.

(46) Amendola, V.; Meneghetti, M. What Controls the Composition and the Structure of Nanomaterials Generated by Laser Ablation in Liquid Solution? *Phys. Chem. Chem. Phys.* **2013**, *15* (9), 3027–3046. https://doi.org/10.1039/c2cp42895d.

(47) Qian, W.; Murakami, M.; Ichikawa, Y.; Che, Y. Highly Efficient and Controllable PEGylation of Gold Nanoparticles Prepared by Femtosecond Laser Ablation in Water. *J. Phys. Chem. C* **2011**, *115* (47), 23293–23298. https://doi.org/10.1021/jp2079567.

(48) Shao, X.; Schnau, P.; Qian, W.; Wang, X. Quantitatively Understanding Cellular Uptake of Gold Nanoparticles via Radioactivity Analysis. *J. Nanosci. Nanotechnol.* **2015**, *15* (5), 3834–3838. https://doi.org/10.1166/jnn.2015.9486.

(49) Wu, P. H.; Onodera, Y.; Ichikawa, Y.; Rankin, E. B.; Giaccia, A. J.; Watanabe, Y.; Qian, W.; Hashimoto, T.; Shirato, H.; Nam, J. M. Targeting Integrins with RGD-Conjugated Gold Nanoparticles in Radiotherapy Decreases the Invasive Activity of Breast Cancer Cells. *Int. J. Nanomedicine* **2017**, *12*, 5069–5085. https://doi.org/10.2147/IJN.S137833.

(50) Tian, C.; Qian, W.; Shao, X.; Xie, Z.; Cheng, X.; Liu, S.; Cheng, Q.; Liu, B.; Wang, X. Plasmonic Nanoparticles with Quantitatively Controlled Bioconjugation for Photoacoustic Imaging of Live Cancer Cells. *Adv. Sci.* **2016**, *3* (12), 1–9. https://doi.org/10.1002/advs.201600237.

(51) Lévy, R.; Thanh, N. T. K.; Christopher Doty, R.; Hussain, I.; Nichols, R. J.; Schiffrin, D. J.; Brust, M.; Fernig, D. G. Rational and Combinatorial Design of Peptide Capping Ligands for Gold Nanoparticles. *J. Am. Chem. Soc.* **2004**, *126* (32), 10076–10084. https://doi.org/10.1021/ja0487269.

(52) Nel, A. E.; Mädler, L.; Velegol, D.; Xia, T.; Hoek, E. M. V.; Somasundaran, P.; Klaessig, F.; Castranova, V.; Thompson, M. Understanding Biophysicochemical Interactions at the Nano-Bio Interface. *Nat. Mater.* **2009**, *8* (7), 543–557. https://doi.org/10.1038/nmat2442.

(53) Sylvestre, J. P.; Poulin, S.; Kabashin, A. V.; Sacher, E.; Meunier, M.; Luong, J. H. T. Surface Chemistry of Gold Nanoparticles Produced by Laser Ablation in Aqueous Media. *J. Phys. Chem. B* **2004**, *108* (43), 16864–16869. https://doi.org/10.1021/jp047134.

(54) Kozlowski, R.; Ragupathi, A.; Dyer, R. B. Characterizing the Surface Coverage of Protein-Gold Nanoparticle Bioconjugates. *Bioconjug. Chem.* **2018**, *29* (8), 2691–2700. https://doi.org/10.1021/acs.bioconjchem.8b00366.

(55) James, A. E.; Driskell, J. D. Monitoring Gold Nanoparticle Conjugation and Analysis of Biomolecular Binding with Nanoparticle Tracking Analysis (NTA) and Dynamic Light Scattering (DLS). *Analyst* **2013**, *138* (4), 1212–1218. https://doi.org/10.1039/c2an36467k.

(56) Scott, A. W.; Garimella, V.; Calabrese, C. M.; Mirkin, C. A. Universal Biotin-PEG-Linked Gold Nanoparticle Probes for the Simultaneous Detection of Nucleic Acids and Proteins. *Bioconjug. Chem.* **2017**, *28* (1), 203–211. https://doi.org/10.1021/acs.bioconjchem.6b00529.

(57) Jia, Y.; Yan, X.; Guo, X.; Zhou, G.; Liu, P.; Li, Z. One Step Preparation of Peptide-Coated Gold Nanoparticles with Tunable Size. *Materials (Basel).* **2019**, *12* (13), 1–12. https://doi.org/10.3390/ma12132107.

(58) Gukowsky, J. C.; Tan, C.; Han, Z.; He, L. Cysteamine-Modified Gold Nanoparticles as a Colorimetric Sensor for the Rapid Detection of Gentamicin. *J. Food Sci.* **2018**, *83* (6), 1631–1638.

https://doi.org/10.1111/1750-3841.14179.

(59) Sharma, A. K.; Pandey, S.; Nerthigan, Y.; Swaminathan, N.; Wu, H. F. Aggregation of Cysteamine-Capped Gold Nanoparticles in Presence of ATP as an Analytical Tool for Rapid Detection of Creatine Kinase (CK-MM). *Anal. Chim. Acta* **2018**, *1024*, 161–168. https://doi.org/10.1016/j.aca.2018.03.027.

(60) Kamentsky, L.; Jones, T. R.; Fraser, A.; Bray, M. A.; Logan, D. J.; Madden, K. L.; Ljosa, V.; Rueden, C.; Eliceiri, K. W.; Carpenter, A. E. Improved Structure, Function and Compatibility for Cellprofiler: Modular High-Throughput Image Analysis Software. *Bioinformatics* **2011**, *27* (8), 1179–1180. https://doi.org/10.1093/bioinformatics/btr095.

(61) Ribeiro, G. P.; Valotto, R. S.; de Oliveira, J. P.; Guimarães, M. C. C.; Lenz, D. An Inexpensive, Automated and Reproducible Method to Conduct Quality Control in Nanoparticles. *Chem. Pap.* **2020**, *74* (9), 2821–2824. https://doi.org/10.1007/s11696-020-01123-3.

(62) Kanetidis, M.; Tsouchnika, M.; Argyrakis, P.; Kopelman, R. A Simple Model for Charged Particle Aggregation and Polarization. *Phys. A Stat. Mech. its Appl.* **2019**, *528*. https://doi.org/10.1016/j.physa.2019.121433.

(63) Vicsek, T. *Fractal Growth Phenomena*; 1992. https://doi.org/10.1142/1407.

(64) Meakin, P. Formation of Fractal Clusters and Networks by Irreversible Diffusion-Limited Aggregation. *Phys. Rev. Lett.* **1983**, *51* (13), 1119–1122. https://doi.org/10.1103/PhysRevLett.51.1119.

(65) Meakin, P. Aggregation Kinetics. *Phys. Scr.* **1992**, *46* (4), 295–331. https://doi.org/10.1088/0031-8949/46/4/002.

(66) Bunde, A.; Havlin, S.; Nossal, R.; Stanley, H. E.; Weiss, G. H. On Controlled Diffusion-Limited Drug Release from a Leaky Matrix. *J. Chem. Phys.* **1985**, *83* (11), 5909–5913. https://doi.org/10.1063/1.449622.

(67) Kosmidis, K.; Argyrakis, P.; Macheras, P. A Reappraisal of Drug Release Laws Using Monte Carlo Simulations: The Prevalence of the Weibull Function. *Pharm. Res.* **2003**, *20* (7), 988–995. https://doi.org/10.1023/A:1024497920145.

(68) Draine, B. T.; Flatau, P. J. Discrete-Dipole Approximation For Scattering Calculations. *J. Opt. Soc. Am. A* **1994**, *11* (4), 1491. https://doi.org/10.1364/josaa.11.001491.

(69) Yurkin, M. A.; Hoekstra, A. G. The Discrete Dipole Approximation: An Overview and Recent Developments. *J. Quant. Spectrosc. Radiat. Transf.* **2007**, *106* (1–3), 558–589. https://doi.org/10.1016/j.jqsrt.2007.01.034.

(70) P. B. Johnson and R. W. Christy. Optical Constant of the Nobel Metals. *Phys. L Re View B* **1972**, *6* (12), 4370–4379.

(71) Amendola, V.; Bakr, O. M.; Stellacci, F. A Study of the Surface Plasmon Resonance of Silver Nanoparticles by the Discrete Dipole Approximation Method: Effect of Shape, Size, Structure, and Assembly. *Plasmonics* **2010**, *5* (1), 85–97. https://doi.org/10.1007/s11468-009-9120-4.

(72) Kealley, C. S.; Cortie, M. B. A Computational Exploration of the Color Gamut of Nanoscale Hollow Scalene Ellipsoids of Ag and Au. *Plasmonics* **2010**, *5* (1), 37–43. https://doi.org/10.1007/s11468-009-9112-4.

(73) Ramachandran, P.; Varoquaux, G. Mayavi: 3D Visualization of Scientific Data. *Comput. Sci. Eng.* **2011**, *13* (2), 40–51. https://doi.org/10.1109/MCSE.2011.35.

(74) Muhamad, N.; Plengsuriyakarn, T.; Na-Bangchang, K. Application of Active Targeting Nanoparticle Delivery System for Chemotherapeutic Drugs and Traditional/Herbal Medicines in Cancer Therapy: A Systematic Review. *Int. J. Nanomedicine* **2018**, *13*, 3921–3935. https://doi.org/10.2147/IJN.S165210.

(75) Gao, M. R.; Zhang, S. R.; Xu, Y. F.; Zheng, Y. R.; Jiang, J.; Yu, S. H. Self-Assembled Platinum Nanochain Networks Driven by Induced Magnetic Dipoles. *Adv. Funct. Mater.* **2014**, *24* (7), 916–

924. https://doi.org/10.1002/adfm.201302262.

(76) Jia, H.; Bai, X.; Zheng, L. One-Step Synthesis and Assembly of Gold Nanochains Using the Langmuir Monolayer of Long-Chain Ionic Liquids and Their Applications to SERS. *CrystEngComm* **2012**, *14* (8), 2920–2925. https://doi.org/10.1039/c2ce06375a.

(77) Xing, S.; Tan, L. H.; Yang, M.; Pan, M.; Lv, Y.; Tang, Q.; Yang, Y.; Chen, H. Highly Controlled Core/Shell Structures: Tunable Conductive Polymer Shells on Gold Nanoparticles and Nanochains. *J. Mater. Chem.* **2009**, *19* (20), 3286–3291. https://doi.org/10.1039/b900993k.

(78) Albanese, A.; Chan, W. C. W. Effect of Gold Nanoparticle Aggregation on Cell Uptake and Toxicity. *ACS Nano* **2011**, *5* (7), 5478–5489. https://doi.org/10.1021/nn2007496.

(79) Jacques, S. L. Optical Properties of Biological Tissues: A Review; Corrigendum. *Phys. Med. Biol.* **2013**, *58* (14), R37–R61, 5007–5008. https://doi.org/10.1088/0031-9155/58/14/5007.

(80) Hooshmand, N.; Mousavi, H. S.; Panikkanvalappil, S. R.; Adibi, A.; El-Sayed, M. A. High-Sensitivity Molecular Sensing Using Plasmonic Nanocube Chains in Classical and Quantum Coupling Regimes. *Nano Today* **2017**, *17*, 14–22. https://doi.org/10.1016/j.nantod.2017.10.009.

(81) Zuo, T.; Goldwyn, H. J.; Isaacoff, B. P.; Masiello, D. J.; Biteen, J. S. Rotation of Single-Molecule Emission Polarization by Plasmonic Nanorods. *J. Phys. Chem. Lett.* **2019**, *10* (17), 5047–5054. https://doi.org/10.1021/acs.jpclett.9b02270.

(82) Lee, S. A.; Biteen, J. S. Spectral Reshaping of Single Dye Molecules Coupled to Single Plasmonic Nanoparticles. *J. Phys. Chem. Lett.* **2019**, *10* (19), 5764–5769. https://doi.org/10.1021/acs.jpclett.9b02480.

(83) Dinish, U. S.; Song, Z.; Ho, C. J. H.; Balasundaram, G.; Attia, A. B. E.; Lu, X.; Tang, B. Z.; Liu, B.; Olivo, M. Single Molecule with Dual Function on Nanogold: Biofunctionalized Construct for in Vivo Photoacoustic Imaging and SERS Biosensing. *Adv. Funct. Mater.* **2015**, *25* (15), 2316–2325. https://doi.org/10.1002/adfm.201404341.

(84) Zhang, W.; Liu, J.; Niu, W.; Yan, H.; Lu, X.; Liu, B. Tip-Selective Growth of Silver on Gold Nanostars for Surface-Enhanced Raman Scattering. *ACS Appl. Mater. Interfaces* **2018**, *10* (17), 14850–14856. https://doi.org/10.1021/acsami.7b19328.

(85) Huang, X.; Jain, P. K.; El-Sayed, I. H.; El-Sayed, M. A. Plasmonic Photothermal Therapy (PPTT) Using Gold Nanoparticles. *Lasers Med. Sci.* **2008**, *23* (3), 217–228. https://doi.org/10.1007/s10103-007-0470-x.

Chapter 4: Development of Targeted 8-arm PEG Nanosystems for Choroidal Neovascular Macular Degeneration Diagnosis and Therapy

4.1 Abstract

Wet macular degeneration, also known as choroidal neovascularization (CNV), affects nearly 10% of people over 75 in developed countries and is the most aggressive and deleterious form of age-related macular degeneration (AMD). Typical treatment includes intravitreal injection of VEGF inhibitors that block angiogenesis and slow AMD progression, but these injections must be performed regularly (typically monthly) and have associated risks due to their invasiveness. Using a readily conjugatable, 8-arm polyethylene glycol (PEG)-fluorescein (FITC) nanosystem, we evaluate its targeting effectiveness when conjugated with a high molar concentration of RGD peptide, one of the most commonly used peptides for active targeting, for uptake into endothelial cells that make up the invasive AMD vessels. FITC and RGD attachment to the PEG nanoparticle, and nanoparticle size distribution were verified using 1D 1H and 2D PGSE DOSY NMR spectroscopy. Furthermore, RGD active targeting effectiveness was tested in vitro via TIRF microscopy, revealing enhanced localization of PEG-FITC-RGD nanoparticles. Laser-induced choroidal neovascularization was performed in vivo in a mouse model to measure RGD uptake effectiveness. It was determined that while in vitro targeting was improved by RGD peptide as much as 2-fold, in vivo experiments showed more modest NP uptake enhancement of 15-20%. Overall, 8-arm PEG NPs represent a new, readily conjugatable nanosystem for potential AMD diagnosis and therapy, wherein new targeting moieties or a combined approach of RGD peptide with secondary moieties should be explored in for future PEG-based models to achieve greater in vivo AMD targeting.

4.2 Introduction

Macular degeneration is the leading cause of progressive vision loss among people in developed countries when older than 60, and affects 10% of people over 75.[1] While there are several different types of age-related macular degeneration (AMD) based on their pathology and molecular drivers, the type of AMD known as choroidal neovascularization is a result of angiogenesis that invades the subretinal space, which in turn causes photoreceptor loss and vision degeneration.[2] This type of AMD is clinically referred to as "wet" macular degeneration, due to the increased leakage of fluid or blood into the macula. The presence of extracellular deposits known as *drusen* are common in the early stages of AMD, and the disease can progress in later stages to the wet variety.[3] While not a lethal diagnosis, macular degeneration leads to vision impairment significant enough to prevent an individual from driving, reading, living independently, and even recognizing faces.[4,5] The exact pathogenesis of wet AMD is not entirely clear, but it is hypothesized to be related to a variety of genetic, metabolic, and environmental factors.[6] The heritability of AMD has been estimated to be between 46-71%, depending on the severity of the disease.[7] There have been 52 genetic variants identified, at 34 different loci that are associated with AMD, many of which are related to lipid metabolism, the immune complement system, and the extracellular matrix (collagen, glycoproteins, etc.).[8] Associations have also been found between AMD progression and genes that are typically associated with chronic inflammation, specifically HRF and RPD; these are used as biomarkers for inflammation, and likely contribute to the formation of the *drusen* that induce disease progression.[9] Other, more broad genetic risk factors include race and eye color, with Caucasians and individuals with light colored eyes showing significantly higher rates of wet AMD.[10] Obesity has been associated with a two-fold increase in risk for AMD, but it is not considered a causative factor in the development of the disease.[11] Hypertension, both treated and untreated, can lead to a three-fold increase in AMD progression.[12]

The treatment of macular degeneration has two choices: 1.) Anti-vascular endothelial growth factor (VEGF) inhibitor-based therapy, which involves a direct intravitreal injection of VEGF drugs into the diseased eye; 2.) Small molecule photodynamic therapy (PDT), where photosensitizing dyes that produce reactive oxygen species (ROS) are injected and taken up by the neovascular cells; following uptake, excitation of the dye by a low power red laser produces the toxic ROS species, killing the cells. The anti-vascular endothelial growth factor (VEGF) treatments are most common, as they inhibit an important factor in the induction of angiogenesis that leads to vision loss, and are highly effective.[6] However, anti-VEGF treatments must be performed frequently (at least monthly) to show effectiveness. Furthermore, while the anti-VEGF treatments do show promising therapeutic outcomes, they still carry significant risks. Endophthalamitis, typically caused by bacterial infection post-intravitreal injection, has been reported to occur in 0.019-1.6% of patients, and is likely a cause of improper sterilization or poor aseptic technique.[13] The anti-VEGF antibody itself can also induce intraocular inflammation that can damage the eye, with significant cases at 2.9-14%.[13] Lastly, and of immense importance, anti-VEGF therapy prevents the worsening of AMD progression, as it prevents growth factors from binding to the VEGF receptor; however, it cannot cure AMD. This means that patients must receive anti-VEGF therapy indefinitely, and the physician must work to find a balance between the frequency of administering anti-VEGF therapy and disease progression so as to prevent worsening of the symptoms. For the reasons listed above, physicians and researchers have been pushing for better AMD therapies, especially in the last 20 years. In 2000, Verteporfin (pharmaceutical name Visudyne), a small molecule photosensitizer, was approved by the FDA for photodynamic therapy of AMD. Photodynamic therapy is the process of exciting a small molecule (called a photosensitizer), leading to the production of reactive oxygen species (ROS), which are cytotoxic and thus causing cell death. Verteporfin-based photodynamic therapy first targets and then kills the endothelial neovasculature that forms in macular degenerative disorders. However, while PDT provides some spatial selectivity for the AMD neovasculature, Verteporfin is not designed to localize specifically to

the eye, nor is it designed to target cell surface receptors. Current forms of photodynamic therapy are achieved using a red laser (693 nm) which excites the photosensitizer. Contrasted with the anti-VEGF therapies, which target neovasculature growth factors to prevent endothelial formation, the AMD photodynamic therapies destroy the neovasculature itself. Hence, because both therapies have different acting mechanisms, it is widely reported that a combined anti-VEGF/PDT approach yields better clinical outcomes than either therapy alone.[14] Overall, however, current AMD photodynamic therapies have several limitations: 1.) Drug localization is not by active targeting, as it accumulates in the retinal neovasculature passively; 2.) The Verteporfin-based therapies destroy the neo-endothelilal vasculature, but do not 'cure' AMD , thus the treatment requires progressive visits to the physician, on average 4 times per year; 3.) The presence of submacular hemorrhage and of widely distributed lesions do render the PDT less effective.[15] An ideal treatment system would localize the photosensitizers in all areas that require treatment, while leaving the rest of the eye unaffected.

Nanoparticles (NPs) have an advantage over currently available 'small molecule' therapeutics, in that a single NP can carry multiple functional moieties with *active*, not passive, targeting. Here, we report on a FITC-conjugated, fluorescent 8-arm-peg nanoparticle modality that is designed to target the endothelial cells of the invasive AMD blood vessels without being injected into the eye. The 8-arm PEG is a polyethylene glycol NP that has eight stretched arms, all attached to a hexaglycerol core. These 8-arm PEG-based nanoparticles have a small size (5-10 nm), have high biocompatibility, and have multiple reactive points for addition of imaging and therapeutic moieties.[16,17] Specifically, an amine group at the end of each arm allows for functionalization to other molecules. To create a fluorescent nanosystem so as to perform fluorescence imaging, fluorescein isothiocyanate isomer I (FITC) is conjugated onto the 8-arm PEG NP. The thiocyanate group of the FITC molecule is responsible for covalently binding the amine onto the PEG particle.[18]

To achieve the 8-arm-peg targeting selectivity, an RGD peptide was loaded onto the PEG particle at high molar concentrations. The RGD peptide has 15 amino acids (RGDRGDRGDRGDPGC), including a cysteine on the carboxy-terminal end that is used in the particle conjugation process. RGD has been shown to bind to integrins, a diverse class of proteins that make up part of the extracellular matrix.[19,20] Specifically, the integrin $\alpha v\beta 3$ has been implicated in the angiogenic process, with a significant increase in expression on highly proliferative cells such as the ones driving the choroidal neovascularization in ocular diseases.[21] Additionally, the RGD motif has been shown to bind to this specific integrin with high affinity.[22] This combination of binding specificity and cellular expression makes the RGD motif a natural choice for targeting choroidal neovascularization. While previous groups have used RGD "small molecule" targeting paradigms to achieve AMD localization,[23,24] actively targeted RGD nanoparticle-based platforms for treating AMD studied primarily in tandem with other peptides,[25] and no studies on any kind of 8-arm-peg NP have been performed for AMD diagnosis or therapy.

Figure 4.1 outlines the biomedical framework for the 8-arm-peg system: In CNV-based angiogenesis, nanoparticle injection results in localized peg particles in the retinal endothelial cells, which can be detected via fluorescence imaging. Such a system can be used to aid in the localization of important therapeutic modalities, such as pharmaceuticals and PDT dyes. It should be noted that 40 kDa 8-arm-peg-based nanosystems, as reported from our group, showed good specificity of localization (using targeting peptides like CTP, cardiac targeting peptide) as well as high contrast for bioimaging.[16,17] Due to the enhanced permeability and retention (EPR) effect, 40 kDa particles tend to accumulate and remain in the body for longer periods of time than smaller NPs.[26] For cardiac-based therapies, using larger PEG NPs is most desirable because myocyte targeting specificity is better thus achieved.[16] However, for retinal therapy, it is desirable for the NPs to have a short half-life, ideally within 24 hours after injection. Furthermore, it is hypothesized that EPR effects could mask the selectivity of the RGD targeting peptide

in bigger NPs, leading to reduced targeting specificity.[27] For these reasons, we have utilized a 10 kDa PEG, as it is the smallest size 8-arm-peg commercially available.

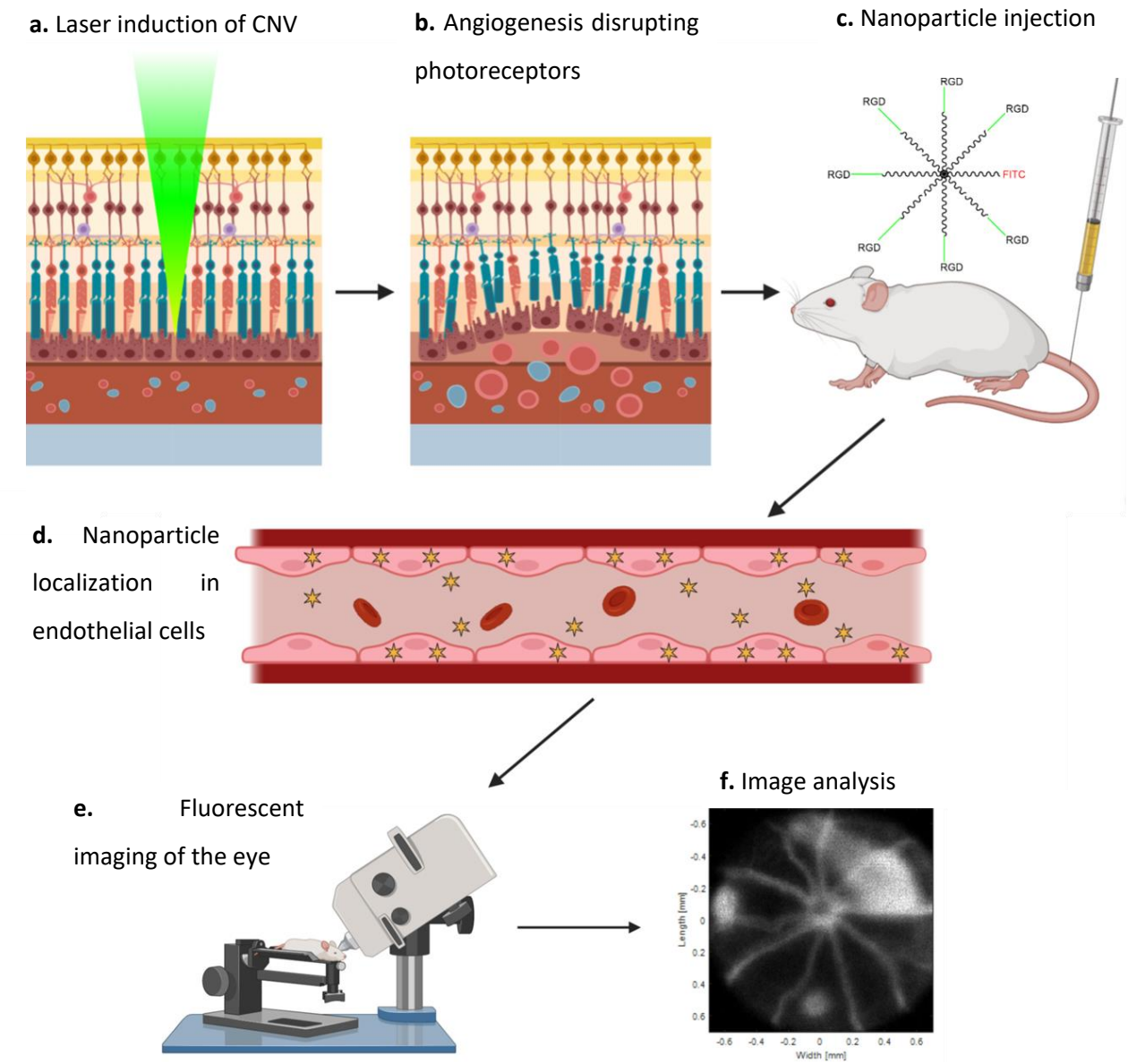

Figure 4.1 An overview of the goal of a targeted particle. a. A photocoagulator is used to irradiate the retina. b. CNV disrupts the membrane as a result of angiogenesis in the region, thus negatively affecting photoreceptors. c. Tail vein nanoparticle injection allows for less pain and smaller chance of infection compared to an intravitreal injection. d. The particles localize specifically to the endothelial cells in the new blood vessels. e-f. Fluorescent molecule imaging shows the eye and the areas of high signal, indicating particle targeting.

Overall, we have succeeded in developing a novel 8-arm PEG fluorescent nanoparticle system that showed a nearly 100% improvement the RGD-assisted targeting to mouse aortic endothelial cells compared to non-RGD conjugated controls. In vivo experiments showed a more modest improvement, of 15-20%. Overall, these experiments present a promising new nanosystem for nanoparticle-assisted AMD theranostics (therapy and diagnostics) for individuals with wet AMD pathologies, with the potential for additional enhancement given the development of new AMD targeting molecules.

4.3 Experimental Procedures

4.3.1 Synthesis of the 8-arm PEG particle Derivatives

The 8-arm PEG FITC RGD particle system consists of four components: the core 8-arm PEG amine particle, FITC fluorescent dye, a MAL-PEG-SCM linker, and the RGD targeting molecule. Synthesis proceeds the same for both the 10 kDa and 40 kDa particle, as published in previous literature.[16,17] A summary of the 8-arm-peg conjugation is provided in Figure 4.2.

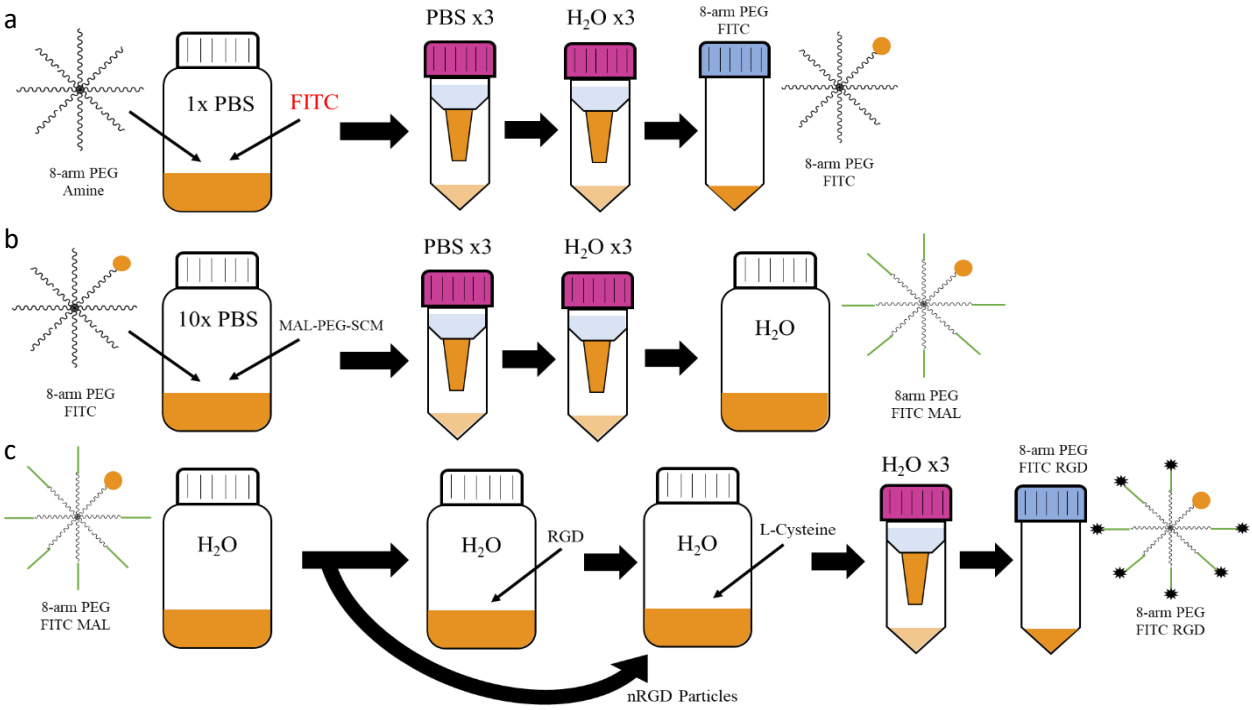

Figure 4.2 An overview of the nanoparticle synthesis. a. The conjugation of FITC to the 8-arm PEG Amine core. b. The addition of the MAL-PEG-SCM linker. c. The addition of RGD and the capping of any exposed maleimide groups. This step separates RGD from nRGD control particles.

The core 10 kDa 8-arm PEG amine particle (Creative PEGworks) was prepared at a concentration of 50 mg/mL in PBS (pH = 7.4), to which a 1.5 molar ratio of fluorescein isothiocyanate isomer I (Sigma Aldrich) in DMSO was added and incubated overnight. The addition of FITC to the 10 kDa core particle is the most straightforward and insensitive to solvent conditions, and therefore can be accomplished using standard phosphate buffered saline (PBS) at a pH of 7.4. As indicated by Figure 4.3a, the amine on the core PEG particle acts as a nucleophile, attacking the central carbon in the isothiocyanate group. The resulting electron shift and proton loss leaves a stable isothiourea bond.[18] The conjugated particle was then washed three times each in PBS and ultrapure water in a 50 mL, 3 kDa centrifuge filter (Sigma Millipore). The washed and concentrated 8-arm PEG FITC particle was then freeze-dried in a lyophilizer.

Thiolated compounds (RGD peptide) cannot be conjugated to the amine on the terminus of the PEG arms due to incompatibility between the peptide's sulfur terminus and 8-arm PEG's amine terminus, and a linker must therefore be added to bridge these functional groups. Maleimide-PEG-Succinimidyl NHS ester (MAL-PEG-SCM) is a heterobifunctional PEG product that allows for the unidirectional addition of the linker, ensuring that the proper functional groups are available for RGD addition.[17] The succinimidyl ester end covalently binds the amine of the PEG particle, while the maleimide on the opposite side is able to bind the thiol of the terminal cysteine in the RGD peptide. To conjugate the MAL-PEG-SCM linker, the 8-arm PEG FITC particle was prepared at a concentration of 20mg/mL in 10x PBS at a pH of 7.2. A 12:1 molar ratio of MAL-PEG-SCM (Creative PEGworks) was prepared separately at 100 mg/mL in 10x PBS pH 7.2, and the two were combined for 1 hour. The amine again acts as a nucleophile, this time on the carbonyl of the succinimidyl NHS ester. The electron movement from the charged oxygen then kicks off the NHS leaving group, completing the substitution reaction, as shown in Figure 4.3b.[18] The maleimide/succinimidyl NHS ester linker is sensitive to pH and time. PBS must be adjusted to pH=7.2 and increased to 10x concentration to optimize the bond formation between the core particle and the linker. This decrease in pH also favors the formation of the bond between maleimide and its eventual target (RDB) and reduces the rate of ring opening, which would render the linker nonfunctional.[18] The newly linker-conjugated particles were then washed in fresh centrifuge filters three times each in 10x PBS pH 7.2 and pure water. At this point, 8-arm PEG FITC MAL particles that were used as controls, lacking the RGD targeting group, were capped with 15 molar equivalents of cysteine in pure water for 1 hour. This binds the reactive maleimide group and prevents the particles from cross linking. These were referred to as nRGD particles. For the particles that were to be conjugated to RGD, 15 molar equivalents of the peptide (MW: 1588 g/mol) were added to the 8-arm PEG FITC MAL in pure water and incubated overnight. It should be noted that RGD is susceptible to degradation. The aspartate residue (the D in RGD) is capable of inducing autolysis through the nucleophilic addition of its side group carboxylate to the adjacent

backbone carbonyl or amide nitrogen. This creates a 5 or 6 membered ring and a charged oxygen that kicks off the rest of the peptide.[28] For this reason, the washes after RGD conjugation must be done immediately after synthesis, and the particle must then be lyophilized. These were then capped with the same 15x molar equivalent ratio of cysteine as nRGD and incubated for an hour. Maleimide reacts with thiols in both RGD and cysteine, where the thiolate anion acts as a nucleophile for one of the carbons involved in the double bond. Electron shift results in an increase in electron density at the other carbon, which then gains a proton from the bulk solvent, as indicated by Figure 4.3c.[18] All particles were washed vigorously with pure water in centrifuge filters before being freeze dried and stored.

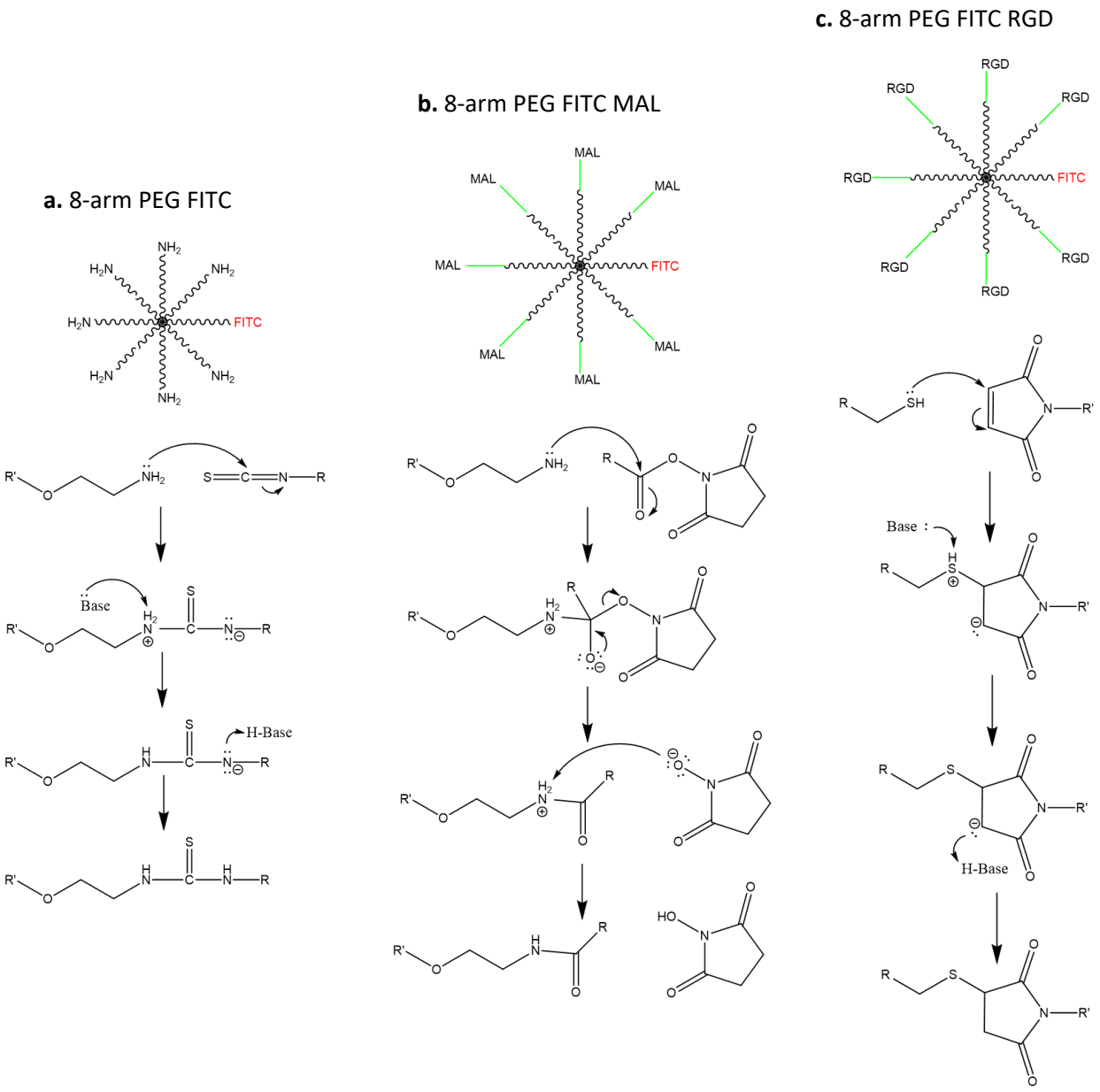

Figure 4.3 An overview of the mechanistic steps of nanoparticle synthesis. The designation R' indicates the side of the growing nanoparticle, while R is the molecule being added. a. The conjugation of FITC to the 8-arm-PEG amine core through the formation of an isothiourea bond. b. The addition of the MAL-PEG-SCM linker through the substitution of the succinimidyl NHS ester. c. The addition of RGD via addition to the maleimide group on the linker.

4.3.2 Verification of Nanoparticle Synthesis and Measurement of Nanoparticle Size

To verify that the 8-arm-peg functional conjugations (FITC, RGD) were successful, ^{1}H NMR spectroscopy was utilized to identify presence of relevant attached functional groups. Spectra were taken of each individual component of the system separately to determine baselines for the respective components of the particle synthesis. Then spectra were taken at each step when possible so that the structure of the synthesized intermediate could be determined, i.e. if the two parts had joined properly.

The size of the core 8-arm PEG particle was determined using NMR diffusion ordered spectroscopy, or DOSY. Approximately 5 mg of PEG NP was dissolved in 600 µL D_2O, and a pulsed gradient spin echo (PGSE) experiment was performed. The fundamental basis of the PGSE experiment is in a sequence that starts with a 90° magnetic pulse followed by a 180° pulse. Between these pulses a magnetic gradient is applied that dephases the precession induced by the first pulse. The 180° pulse flips the direction of precession, and another, identical gradient is applied. In a hypothetical scenario, if there is no diffusion, this second pulse would reverse the initial dephasing done by the first pulse and all spins would be realigned. However, due to particle diffusion, the signal is not fully refocused, and signal attenuation occurs. The rate of this attenuation can be used to calculate the diffusion coefficient.[29–31] Pairing this experiment with a processing technique known as diffusion ordered spectroscopy (DOSY) allows for the calculation of the diffusion coefficient from the spectra created by the PGSE procedure.[32] This technique creates a 2-dimensional plot with chemical shift on the x-axis and the diffusion coefficient on the y-axis. Because the nanoparticle has a distribution of size, a weighted average was taken by the software to determine the average diffusion coefficient. This calculated value (D_{trans}) could then be substituted into the Stokes-Einstein equation (Equation 4.1), along with the viscosity (η) of D_2O (1.2467) and temperature (35 C), and the radius of the particle was determined.[17]

$$r = kT/6\pi\eta D_{trans} \tag{4.1}$$

4.3.3 Maintenance of Cell Culture

Before beginning *in vivo* experiments, cell culture was first utilized to verify the effectiveness of the targeting moieties. To approximate the neovascular cells present in wet macular degeneration, mouse primary aortic endothelial cells (MAEC) were used (Cell Biologics). These cells have been used to emulate vascular endothelial cells in obesity, diabetes, and wet macular degeneration.[23,33,34] As MAECs are somatic cells, they are not immortal and cell passage must be tracked. Cells were maintained in DMEM with 5% FBS, 1% penicillin/streptomycin, and 1% antibiotic-antimycotic (Gibco). Cultures were maintained and split every 48-72 hours, and passage number was recorded. Splitting began with aspirating the spent media off the cells and washing twice with sterile DPBS (Gibco). Clean cells were then incubated with trypsin 0.25% (Gibco) for 5-8 minutes, or until cells were released from the surface of the culture dish. Using pre-warmed media, cells and trypsin were transferred to 15 mL centrifuge tubes and spun at 500 g for 5 minutes. The media-trypsin mixture was aspirated off the cell pellet, which was then combined with fresh media and aliquoted into clean T75 culture flasks. Each flask was typically plated with $5x10^5$ to $1x10^6$ cells. Cells that were to be frozen were combined with freezing media, consisting of 50% FBS, 40% normal cell media, and 10% DMSO, after the centrifugation step. They were kept at -20° C for 15 minutes before being transferred to liquid nitrogen.

4.3.4 Cell Loading Experiments: TIRF Imaging and Analysis

Loading experiments were conducted on small, glass-bottom cell culture plates. The plates were incubated with $1x10^5$ cells each and allowed to grow for 24 hours. Cells were treated with varying concentrations of control (nRGD) and RGD particles and incubated for 24 hours. The following day, after washing 5 times with DPBS, fresh media was added to keep cells viable. Total Internal Reflection Fluorescence (TIRF) microscopy was used to image and quantify the loading of the particles in the MAEC cells. In TIRF imaging, a laser is directed at the glass bottom of the culture plate at the critical angle where

light is reflected back into the microscope. This technique allows for resolution of a very thin horizontal plane in the cell (also known as the optical section), and the near total elimination of background fluorescence means images can easily be quantified.[35] ImageJ was used to determine the intensity of light fluorescing off the cells, which correlates to the success of the targeting peptide RGD. Using the software, representative images had background light eliminated, and the pixel intensity along a line was measured. The maximum intensity was averaged with that of 5 other images and this average was used for comparison with the other concentrations.

4.3.5 In vivo experiments using a C57BL/6 mouse model

C57BL/6 mice were used as the in vivo model. To induce neovascularization in the eye in a carefully controlled way, a photocoagulator is used to disrupt Bruch's membrane. The protocol used is based on previously published studies.[36] This method is the most reliable way to induce neovascularization, whereas injections of viral vectors overexpressing VEGF are much less effective.[36] Imaging of the eye was performed through a combination of two techniques. First, images of the eye itself were captured using a method known as optical coherence tomography or OCT. This process is non-invasive and allows for resolution of around 5-10 µm. Where standard spectroscopy suffers from high background due to random scattering of light, OCT uses this background light to measure interference with a reference beam. This allows for a computational process that eliminates background from the final image, giving high resolution.[37] The second method was fluorescent molecule spectroscopy, and specifically was meant for measuring the fluorescence of the nanoparticle in the eye. Used in tandem, it is possible to get a clear picture of the area of neovascularization and particle localization in the same image.

Adult, 6-8-week-old C57BL/6 mice weighing 19-21 g were utilized for *in vivo* studies. For CNV induction, mice were first anesthetized with a mixture of ketamine (100 mg/kg) and xylazine (10 mg/kg)

via intraperitoneal (IP) injection. Before the experiment, the pupils were dilated with a topical application of phenylephrine hydrochloride 2.5% and tropicamide 1%. Topical tetracaine drops were applied prior to the experiment for additional anesthesia. A home-made, small table allowed for the movement of the mouse to align with the laser properly and was also equipped to maintain mouse body temperature through resistor-based heating. Balanced Salt Solution (BSS, Altaire Pharmaceuticals, Inc., Aquebogue, NY) was used to wash the cornea and keep it moist. Baseline OCT and fluorescent molecule images were taken using free fluorescein sodium (10%, 0.1 ml/kg, Akorn Inc, Lake Forest, IL) injected intraperitoneally. After imaging, oculentum was applied to the cornea to protect it and minimize inflammation.

To reduce laser scattering, the cornea was covered by a glass slide coupling with gel. CNV was induced through irradiation using an argon green laser to burn Bruch's membrane. The laser was focused on the eye through a slit lamp with 75 µm spot size, 100 mW power, and 100 ms duration. Because of the inherent variability of the system, four burns were induced around the optic nerve in each mouse to ensure at least one success. Oculentum was applied after treatment. Mice were then housed for 7 days to allow the CNV to manifest. Imaging using free dye was then done again to determine the success of the laser treatment prior to nanoparticle injection. An additional day of waiting allowed for free dye to naturally leave the system. After evaluation of the success of the CNV, nanoparticles were injected through the orbital venous varix in the tail (20 mg/mL, 10 mL/kg). Images were taken again immediately following nanoparticle injection and after 8 and 24 hours.

All mice were treated in accordance with the ARVO (The Association for Research in Vision and Ophthalmology) Statement for the Use of Animals in Ophthalmic and Vision Research. All experimental procedures were approved by the Institutional Animal Care & Use Committee (IACUC) at The University of Michigan (Protocol PRO00006486, Photoacoustic & Molecular Imaging of the Eye, PI: Paulus).

4.4 Results and Discussion

4.4.1 8-arm PEG Synthesis and Characterization via NMR Spectroscopy

8-arm-peg NPs were synthesized with attached fluorescent fluorescein (FITC; 1.5x molar ratio) and attached RGD peptide (6x molar ratio) or using a non-RGD control ('nRGD'; 6x molar ratio). To characterize each sample, ^{1}H NMR spectroscopy was utilized, with 2D DOSY NMR spectroscopy used to determine the NP size. For the ^{1}H NMR spectroscopy, the elongated polymeric nature of the 8-arm PEG particle means that the NMR spectra have very intense peaks at the chemical shifts associated with ethylene glycol. Of the peaks seen on Figure 4.4a, that which is centered around 3.73 ppm is the peak associated with the ethylene glycol functional group. The peak at 4.8 ppm is due to residual water from the solvent, while that at 3.02 ppm is the primary amine at the end of the polymer chain. The amine peak is an important indicator for the success of the linker conjugation, as it changes from a primary to a secondary amine as the new bond is formed. Additionally, due to the high intensity of the PEG peak, any peaks from other substituent groups, such as FITC, RGD, or the linker, must be verified at chemical shifts outside of 3-4 ppm. The characteristic peaks used to verify FITC conjugation were the cluster at roughly 6.5-6.7 ppm as shown on Figure 4.4b. These peaks correspond to the hydrogen atoms on the aromatic rings, and are a unique feature not shared by any other particle components. From Figure 4.4e, these peaks can be clearly seen from 6-7 ppm. Being an oligopeptide consisting of five distinct amino acids, RGD has a complex NMR spectrum shown in Figure 4.4d, with several peaks in the same area as PEG. For this reason, the peaks used to verify RGD addition were those from 7.5-8.5 ppm. The presence of peaks in this range can be seen in Figure 4.4e, indicating that all necessary components were successfully conjugated to the 8-arm PEG core particle. The MAL-PEG-SCM linker, being primarily made up of PEG like the core particle, has peaks in the same location as do the other components, based on Figure 4c. Since RGD cannot

bind the amine of the core particle, its presence in the completed particle shows that the MAL-PEG-SCM linker was conjugated properly.

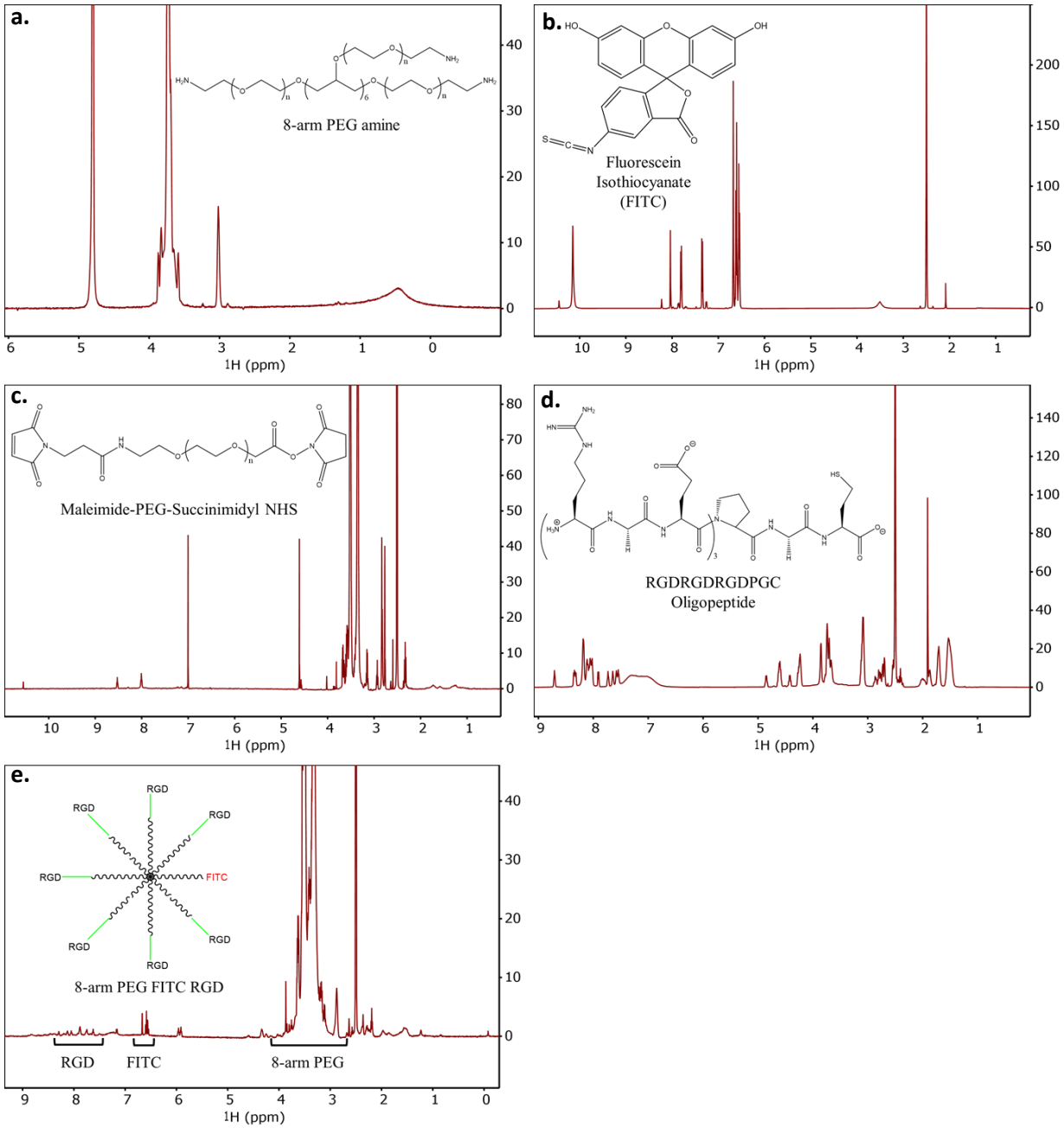

Figure 4.4 a-d. 1H NMR spectra for each component of the nanoparticle synthesis. a. 10 kDa 8-arm-peg base NP b. fluorescein isothiocyanate (FITC) c. 2kDa maleimide-PEG-succinimidyl N-hydrosuccinimide (NHS) d. RGD Peptide (RGDRGDRGDRGDPGC) e. The completed 8-arm PEG FITC RGD particle.

The 2D DOSY spectra are shown for the core 10 kDa and 40 kDa particles in Figure 4.5. Because the PEG NP is a polymer with a distribution of lengths, there are modest variations (±10%) in NP size, and therefore 4 major 2D NMR peaks are observed, instead of 1 peak for a NP of single size.

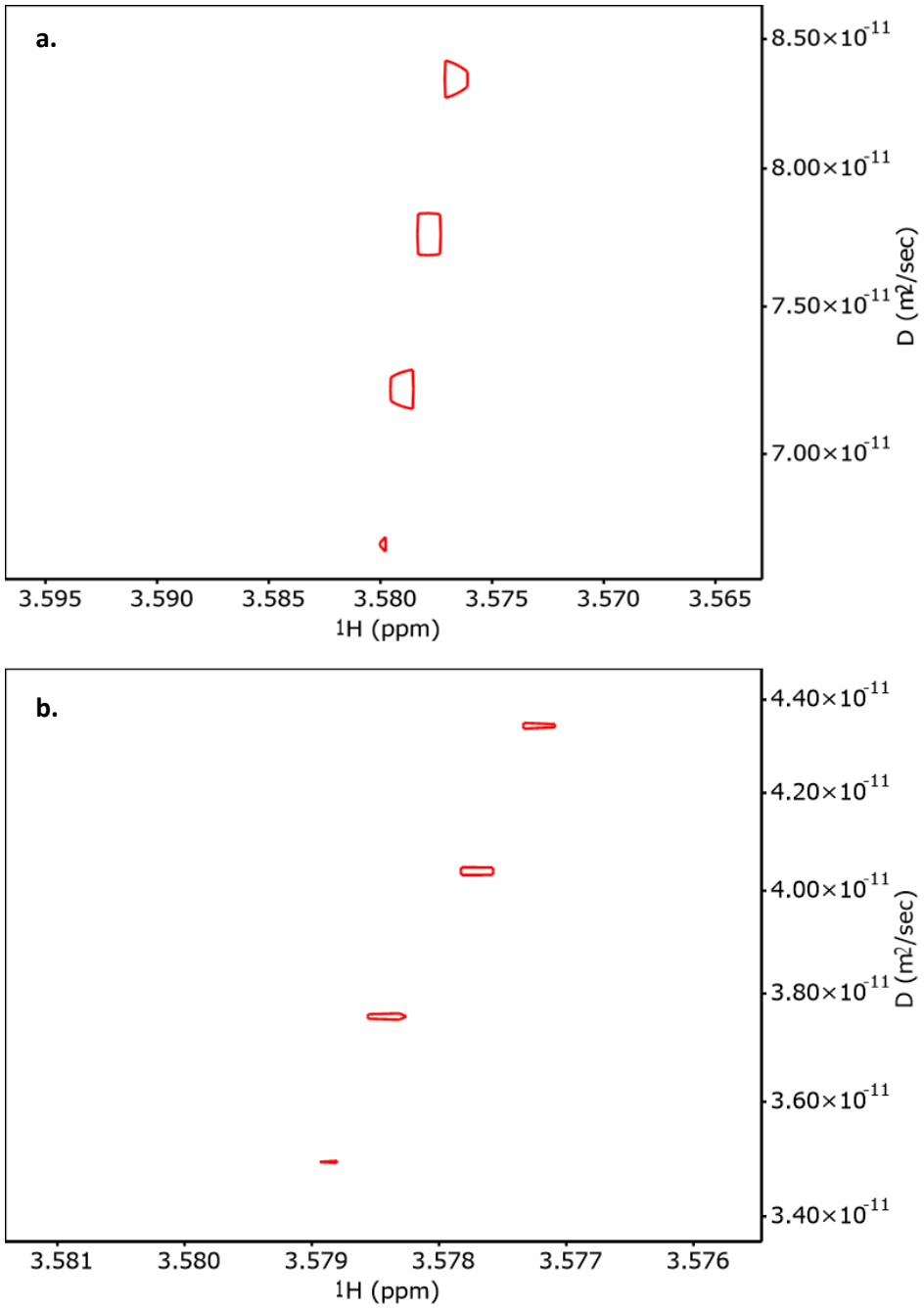

Figure 4.5 2D DOSY NMR spectra for the core 8-arm PEG amine particle. The axis range is narrow (±10%), wherein peak differences represent variations in total particle mass. a. The 10 kDa 8-arm-peg NP utilized in this study b. The 40 kDa 8-arm-peg NP.

Figure 4.5a and 4.5b show the four most intense peaks measured in the 10 kDa and 40 kDa particles, respectively. Averaging these 4 peaks, the 10 kDa particle had an average diffusion coefficient of 7.619×10^{-11} m^2/sec, and substitution into the Stokes-Einstein equation (Equation 4.1 in Methods) yields a diameter of 5.178 nm. The 40 kDa particle had an average diffusion coefficient of 3.891×10^{-11} m^2/sec, which corresponds to a computed diameter of 10.14 nm, in agreement with published literature of the 40 kDa particle.[17]

4.4.2 *In-vitro* TIRF Imaging of RGD-Conjugated 8-arm-peg NPs

In vitro total internal reflectance fluorescence (TIRF) cell imaging was performed using 8-arm-peg nanoparticles when conjugated to RGD peptide and without RGD peptide ('nRGD') to study the RGD-assisted NP uptake, as shown in Figure 4.6. Quantifying the NP uptake, the highest concentration of 8-arm-peg-RGD incubated sample, at 3 mg/mL, produced the largest contrast between RGD and nRGD-loaded PEG NPs (Figure 4.6a). Based on the pixel intensity of the analyzed images produced by the TIRF system, there was a 104% increase in particle loading attributable to the RGD peptide. This separation gradually decreased with incubated PEG NP concentration, with the 1 mg/mL condition increasing intensity 64%, the 0.5 mg/mL increasing 41%, and the 0.3 mg/mL increasing 31%. Qualitatively, it can be seen in Figure 4.6b that each RGD image appears noticeably brighter than the corresponding nRGD image, wherein the brightness also appears to attenuate at lower concentrations. Interestingly, while the size of the 10 kDa PEG NPs (5 nm) is small enough to enter the nucleus, the particles form a crescent or hollow circle, which is a clear indicator of NP uptake only in cytoplasmic regions.[38]

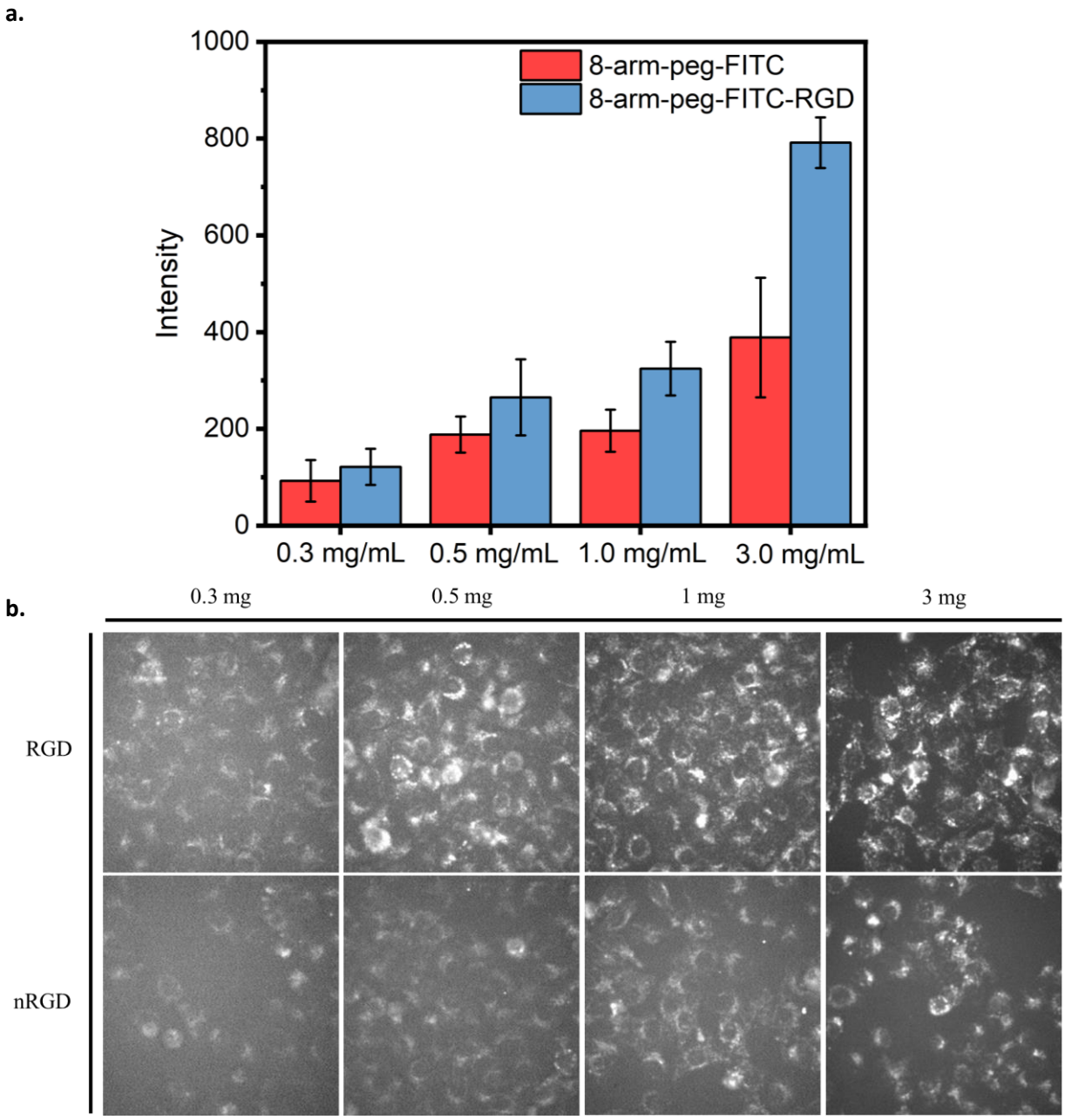

Figure 4.6 Summary of results from the cell loading experiments and TIRF microscopy imaging. a. Quantitative analysis of the four concentrations with standard deviation used for error bars. Intensity refers to the calculated value of pixel brightness from the image analysis. b. Representative images from each concentration and condition. Note that background appears to increase slightly as concentration decreases; this is simply indicative of the decreasing fluorescence of the cells.

Overall, because both RGD and nRGD loaded cells were incubated for the same amount of time and at the same concentration, factors other than EPR effects or concentration gradients across the membrane must account for the improvement due to RGD. Hence, the *in vitro* 8-arm-peg imaging results give strong support to the notion that RGD improves the NP-assisted cell binding and uptake at relevant biological concentrations, most likely due the binding affinity of the RGD peptide to the integrin protein $\alpha_v\beta_3$, which leads to a greater rate of cellular uptake.[19–21]

4.4.3 *In vivo* Imaging of RGD-Conjugated 8-arm-peg NPs

The success of the cell loading experiments *in vitro* prompted translational *in vivo* testing, preliminarily with two mice that had induced retinal neovascularization, one mouse receiving RGD and the second mouse receiving nRGD PEG NP injection. The results, seen in Figure 4.7, reveal increased RGD signal intensity relative to the nRGD control. Small spots around the periphery of the spider-like neovasculature vessels in the retina represent particle fluorescence in the CNV lesions induced by photocoagulation.

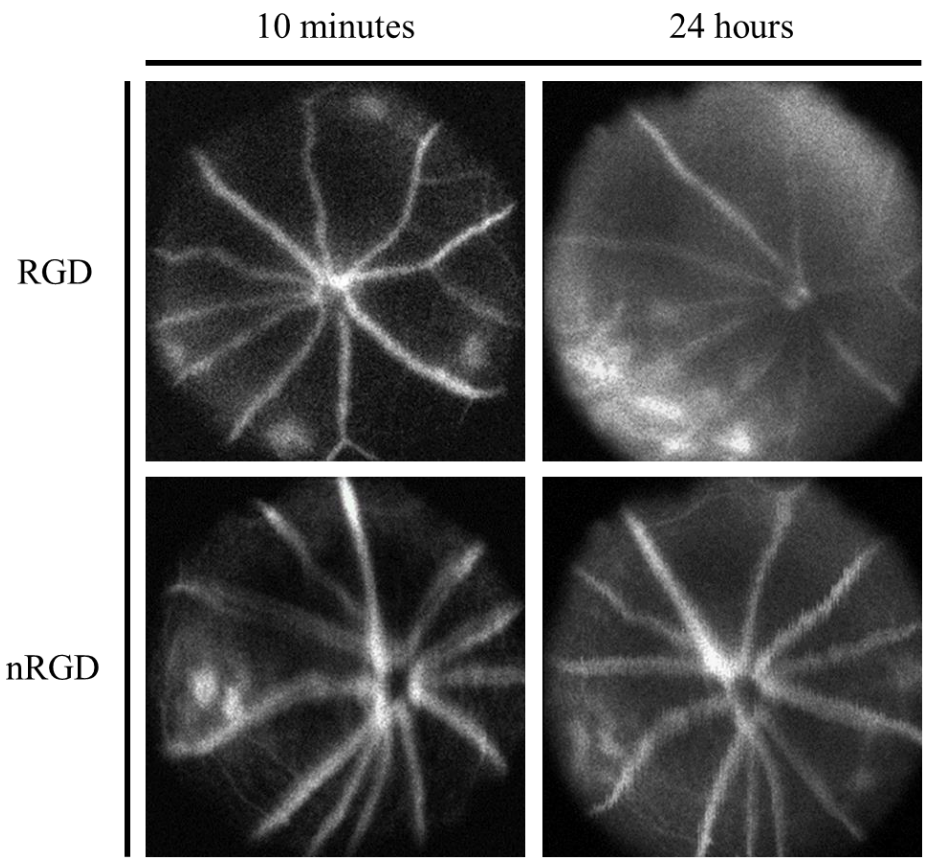

Figure 4.7 Images of the retina in RGD and nRGD treated mice. The large blood vessels indicated by high fluorescence are normal in the eye, whereas the fluorescence near the edges represents CNV lesions being illuminated by nanoparticles.

In both RGD and nRGD conditions, there is visible fluorescence in these spots 10 minutes after incubation, indicating some particle uptake. After 24 hours, the neovasculature of the RGD treated mouse is substantially brighter than that of the nRGD treated mouse vessels. This indicates that in these mice, the RGD peptide was able to enhance particle binding and uptake to the CNV endothelial cells to such a degree that there was clear visibility 24 hours after injection.

To improve statistical significance, the experiment was repeated with more mice, four in each condition. Representative images for two mice in each condition are shown in Figure 4.8.

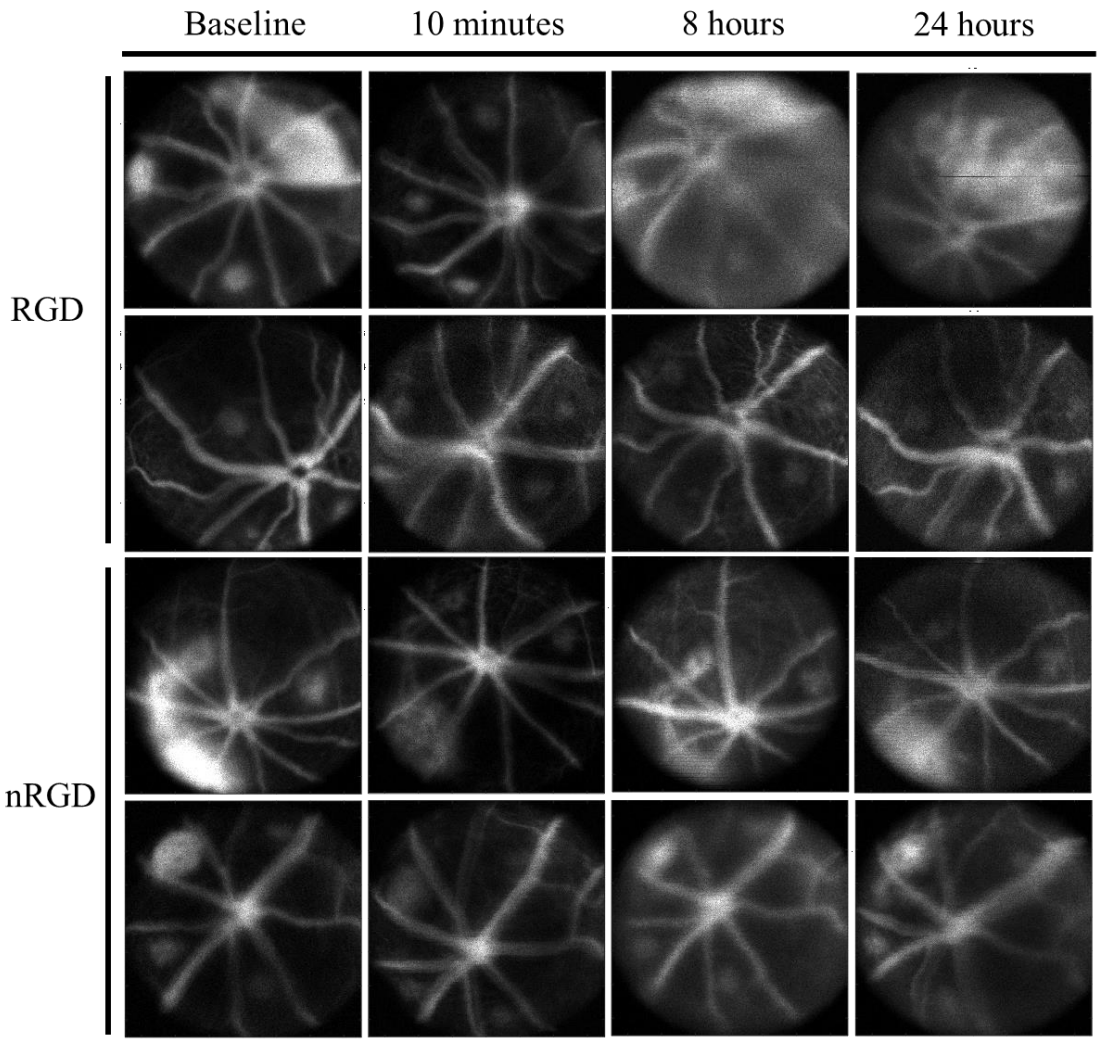

Figure 4.8 Representative images from the second mouse experiment with a higher number of mice used. Baseline refers to the injection of free dye used prior to particle injection, meant to show the success of the CNV induction. Clouding of the eye can be seen in the 8- and 24-hour images of some mice.

Mice treated with nRGD showed little increase in fluorescence over time, similar to the mouse experiment in Figure 4.7. Spots along the edge of the eye at the start looked dull and only slightly increased in intensity in contrast. In contrast, the mice treated with RGD targeting NPs show modest fluorescence upon *in vivo* excitation, on average 15-20% brighter than the nRGD controls.

4.5 Conclusion

This study evaluated fluorescent 8-arm-peg NPs for RGD-assisted targeting to the age-related macular degeneration (AMD) neovasculature. *In vitro* experiments reveal a strong, measurable difference between nRGD (no RGD) and RGD targeting, with RGD providing up to approximately a 100% increase in NP uptake. Furthermore, cell uptake of NPs with RGD targeting shows concentration dependence, with the highest incubated NP concentration providing the greatest *in vitro* contrast. *In vivo* experiments at high incubated PEG concentrations (20 mg/mL injections) showed approximately 15-20% in targeting signal enhancement due to NP targeting. To improve PEG NP *in vivo* targeting, several future directions are being explored. Previous studies have indicated that RGD works better when used together with other targeting agents ('dual targeting') to treat AMD.[25] Therefore, iobenguane (MIBG) derivatives are being synthesized to be used as an alternative, or to be used in tandem, with the commonly utilized RGD peptide.[39] New studies have indicated that in CNV endothelial cells, the β-adrenergic pathways are upregulated, providing a target that is relatively specific for a hypothetical MIBG-bound nanoparticle, as this small molecule targets norepinephrine receptors and transporters (NET).[40,41] Current work in our group has led to the successful synthesis of a form of MIBG that contains the requisite thiol functional group necessary to be conjugated directly to the MAL-PEG-SCM linker. Additional studies are planned to evaluate PEG NP theranostic effects when conjugated with photosensitizers, namely Verteporfin and Ce6. Overall, 8-arm PEG NPs represent a new, readily conjugatable nanosystem for potential AMD diagnosis and therapy, with potential benefits for *in vivo* therapeutic enhancement.

4.6 References

(1) Klein, R.; Klein, B. E. K.; Knudtson, M. D.; Meuer, S. M.; Swift, M.; Gangnon, R. E. Fifteen-Year Cumulative Incidence of Age-Related Macular Degeneration: The Beaver Dam Eye Study. *Ophthalmology* **2007**, *114* (2), 253–262. https://doi.org/10.1016/j.ophtha.2006.10.040.

(2) Ahmad, I.; Balasubramanian, S.; Del Debbio, C. B.; Parameswaran, S.; Katz, A. R.; Toris, C.; Fariss, R. N. Regulation of Ocular Angiogenesis by Notch Signaling: Implications in Neovascular Age-Related Macular Degeneration. *Invest. Ophthalmol. Vis. Sci.* **2011**, *52* (6), 2868–2878. https://doi.org/10.1167/iovs.10-6608.

(3) Sarks, S. H. Drusen and Their Relationship to Senile Macular Degeneration. *Aust. N. Z. J. Ophthalmol.* **1980**, *8* (2), 117–130. https://doi.org/10.1111/j.1442-9071.1980.tb01670.x.

(4) Tran, T. H. C.; Rambaud, C.; Despretz, P.; Boucart, M. Scene Perception in Age-Related Macular Degeneration. *Investig. Opthalmology Vis. Sci.* **2010**, *51* (12), 6868. https://doi.org/10.1167/iovs.10-5517.

(5) Mazzoli, L. S.; Urata, C. N.; Kasahara, N. Face Memory Deficits in Subjects with Eye Diseases: A Comparative Analysis between Glaucoma and Age-Related Macular Degeneration Patients from a Developing Country. *Graefes Arch. Clin. Exp. Ophthalmol.* **2019**, *257* (9), 1941–1946. https://doi.org/10.1007/s00417-019-04380-5.

(6) Al-Zamil, W. M.; Yassin, S. A. Recent Developments in Age-Related Macular Degeneration: A Review. *Clin. Interv. Aging* **2017**, *12*, 1313–1330. https://doi.org/10.2147/CIA.S143508.

(7) Seddon, J. M.; Cote, J.; Page, W. F.; Aggen, S. H.; Neale, M. C. The US Twin Study of Age-Related Macular Degeneration: Relative Roles of Genetic and Environmental Influences. *Arch. Ophthalmol. Chic. Ill 1960* **2005**, *123* (3), 321–327. https://doi.org/10.1001/archopht.123.3.321.

(8) Fritsche, L. G.; Igl, W.; Cooke Bailey, J. N.; Grassmann, F.; Sengupta, S.; Bragg-Gresham, J. L.; Burdon, K. P.; Hebbring, S. J.; Wen, C.; Gorski, M.; Kim, I. K.; Cho, D.; Zack, D.; Souied, E.; Scholl, H. P. N.; Bala, E.; Lee, K. E.; Hunter, D. J.; Sardell, R. J.; Mitchell, P.; Merriam, J. E.; Cipriani, V.; Hoffman, J. D.; Schick, T.; Lechanteur, Y. T. E.; Guymer, R. H.; Johnson, M. P.; Jiang, Y.; Stanton, C. M.; Buitendijk, G. H. S.; Zhan, X.; Kwong, A. M.; Boleda, A.; Brooks, M.; Gieser, L.; Ratnapriya, R.; Branham, K. E.; Foerster, J. R.; Heckenlively, J. R.; Othman, M. I.; Vote, B. J.; Liang, H. H.; Souzeau, E.; McAllister, I. L.; Isaacs, T.; Hall, J.; Lake, S.; Mackey, D. A.; Constable, I. J.; Craig, J. E.; Kitchner, T. E.; Yang, Z.; Su, Z.; Luo, H.; Chen, D.; Ouyang, H.; Flagg, K.; Lin, D.; Mao, G.; Ferreyra, H.; Stark, K.; von Strachwitz, C. N.; Wolf, A.; Brandl, C.; Rudolph, G.; Olden, M.; Morrison, M. A.; Morgan, D. J.; Schu, M.; Ahn, J.; Silvestri, G.; Tsironi, E. E.; Park, K. H.; Farrer, L. A.; Orlin, A.; Brucker, A.; Li, M.; Curcio, C.; Mohand-Saïd, S.; Sahel, J.-A.; Audo, I.; Benchaboune, M.; Cree, A. J.; Rennie, C. A.; Goverdhan, S. V.; Grunin, M.; Hagbi-Levi, S.; Campochiaro, P.; Katsanis, N.; Holz, F. G.; Blond, F.; Blanché, H.; Deleuze, J.-F.; Igo, R. P.; Truitt, B.; Peachey, N. S.; Meuer, S. M.; Myers, C. E.; Moore, E. L.; Klein, R.; Hauser, M. A.; Postel, E. A.; Courtenay, M. D.; Schwartz, S. G.; Kovach, J. L.; Scott, W. K.; Liew, G.; Tʃan, A. G.; Gopinath, B.; Merriam, J. C.; Smith, R. T.; Khan, J. C.; Shahid, H.; Moore, A. T.; McGrath, J. A.; Laux, R.; Brantley, M. A.; Agarwal, A.; Ersoy, L.; Caramoy, A.; Langmann, T.; Saksens, N. T. M.; de Jong, E. K.; Hoyng, C. B.; Cain, M. S.; Richardson, A. J.; Martin, T. M.; Blangero, J.; Weeks, D. E.; Dhillon, B.; van Duijn, C. M.; Doheny, K. F.; Romm, J.; Klaver, C. C. W.; Hayward, C.; Gorin, M. B.; Klein, M. L.; Baird, P. N.; den Hollander, A. I.; Fauser, S.; Yates, J. R. W.; Allikmets, R.; Wang, J. J.; Schaumberg, D. A.; Klein, B. E. K.; Hagstrom, S. A.; Chowers, I.; Lotery, A. J.; Léveillard, T.; Zhang, K.; Brilliant, M. H.; Hewitt, A. W.; Swaroop, A.; Chew, E. Y.; Pericak-Vance, M. A.; DeAngelis, M.; Stambolian, D.; Haines, J. L.; Iyengar, S. K.; Weber, B. H. F.; Abecasis, G. R.; Heid, I. M. A Large Genome-Wide Association Study of Age-Related Macular Degeneration Highlights Contributions of Rare and Common Variants. *Nat. Genet.* **2016**, *48* (2), 134–143. https://doi.org/10.1038/ng.3448.

(9) Sitnilska, V.; Kersten, E.; Altay, L.; Schick, T.; Enders, P.; Jong, E. K. de; Langmann, T.; Hoyng, C. B.; Hollander, A. I. den; Fauser, S. Major Predictive Factors for Progression of Early to Late Age-Related Macular Degeneration. *Ophthalmologica* **2020**. https://doi.org/10.1159/000507196.

(10) Lambert, N. G.; Singh, M. K.; ElShelmani, H.; Mansergh, F. C.; Wride, M. A.; Padilla, M.; Keegan, D.; Hogg, R. E.; Ambati, B. K. Risk Factors and Biomarkers of Age-Related Macular Degeneration. *Prog. Retin. Eye Res.* **2016**, *54*, 64–102. https://doi.org/10.1016/j.preteyeres.2016.04.003.

(11) Seddon, J. M.; Cote, J.; Davis, N.; Rosner, B. Progression of Age-Related Macular Degeneration: Association with Body Mass Index, Waist Circumference, and Waist-Hip Ratio. *Arch. Ophthalmol. Chic. Ill 1960* **2003**, *121* (6), 785–792. https://doi.org/10.1001/archopht.121.6.785.

(12) Klein, R.; Klein, B. E. K.; Tomany, S. C.; Cruickshanks, K. J. The Association of Cardiovascular Disease with the Long-Term Incidence of Age-Related Maculopathy: The Beaver Dam Eye Study. *Ophthalmology* **2003**, *110* (6), 1273–1280. https://doi.org/10.1016/S0161-6420(03)00599-2.

(13) Ghasemi Falavarjani, K.; Nguyen, Q. D. Adverse Events and Complications Associated with Intravitreal Injection of Anti-VEGF Agents: A Review of Literature. *Eye* **2013**, *27* (7), 787–794. https://doi.org/10.1038/eye.2013.107.

(14) Kaiser, P. K. Combination Therapy with Verteporfin and Anti-VEGF Agents in Neovascular Age-Related Macular Degeneration: Where Do We Stand? *Br. J. Ophthalmol.* **2010**, *94* (2), 143–145. https://doi.org/10.1136/bjo.2009.159863.

(15) Chhablani, J. K. Disadvantages of Photodynamic Therapy for Polypoidal Choroidal Vasculopathy. *Indian J. Ophthalmol.* **2010**, *58* (6), 552–553. https://doi.org/10.4103/0301-4738.71691.

(16) Avula, U. M. R.; Yoon, H. K.; Lee, C. H.; Kaur, K.; Ramirez, R. J.; Takemoto, Y.; Ennis, S. R.; Morady, F.; Herron, T.; Berenfeld, O.; Kopelman, R.; Kalifa, J. Cell-Selective Arrhythmia Ablation for

Photomodulation of Heart Rhythm. *Sci. Transl. Med.* **2015**, *7* (311), 311ra172-311ra172. https://doi.org/10.1126/scitranslmed.aab3665.

(17) Hopkins, T.; Swanson, S. D.; Hoff, J. D.; Potter, N.; Ukani, R.; Kopelman, R. Ultracompact Nanotheranostic PEG Platform for Cancer Applications. *ACS Appl. Bio Mater.* **2018**, *1* (4), 1094–1101. https://doi.org/10.1021/acsabm.8b00315.

(18) Hermanson, G. T. *Bioconjugate Techniques*. *Elsevier.* **2003**, 183-184.

(19) Ruoslahti, E. Rgd and Other Recognition Sequences for Integrins. *Annu. Rev. Cell Dev. Biol.* **1996**, *12* (1), 697–715. https://doi.org/10.1146/annurev.cellbio.12.1.697.

(20) Kapp, T. G.; Rechenmacher, F.; Neubauer, S.; Maltsev, O. V.; Cavalcanti-Adam, E. A.; Zarka, R.; Reuning, U.; Notni, J.; Wester, H.-J.; Mas-Moruno, C.; Spatz, J.; Geiger, B.; Kessler, H. A Comprehensive Evaluation of the Activity and Selectivity Profile of Ligands for RGD-Binding Integrins. *Sci. Rep.* **2017**, *7* (1), 1–13. https://doi.org/10.1038/srep39805.

(21) Friedlander, M.; Theesfeld, C. L.; Sugita, M.; Fruttiger, M.; Thomas, M. A.; Chang, S.; Cheresh, D. A. Involvement of Integrins Alpha v Beta 3 and Alpha v Beta 5 in Ocular Neovascular Diseases. *Proc. Natl. Acad. Sci. U. S. A.* **1996**, *93* (18), 9764–9769. https://doi.org/10.1073/pnas.93.18.9764.

(22) Plow, E. F.; Haas, T. A.; Zhang, L.; Loftus, J.; Smith, J. W. Ligand Binding to Integrins. *J. Biol. Chem.* **2000**, *275* (29), 21785–21788. https://doi.org/10.1074/jbc.R000003200.

(23) Uehara, H.; Muddana, S. K.; Zhang, X.; Das, S. K.; Bhuvanagiri, S.; Liu, J.; Wu, Y.; Choi, S.; Carroll, L. S.; Archer, B.; Ambati, B. K. Targeted Delivery of FLT-Morpholino Using Cyclic RGD Peptide. *Transl. Vis. Sci. Technol.* **2017**, *6* (3). https://doi.org/10.1167/tvst.6.3.9.

(24) Zhang, X.; Bohner, A.; Bhuvanagiri, S.; Uehara, H.; Upadhyay, A. K.; Emerson, L. L.; Bondalapati, S.; Muddana, S. K.; Fang, D.; Li, M.; Sandhu, Z.; Hussain, A.; Carroll, L. S.; Tiem, M.; Archer, B.; Kompella,

U.; Patil, R.; Ambati, B. K. Targeted Intraceptor Nanoparticle for Neovascular Macular Degeneration: Preclinical Dose Optimization and Toxicology Assessment. *Mol. Ther.* **2017**, *25* (7), 1606–1615. https://doi.org/10.1016/j.ymthe.2017.01.014.

(25) Singh, S. R.; Grossniklaus, H. E.; Kang, S. J.; Edelhauser, H. F.; Ambati, B. K.; Kompella, U. B. Intravenous Transferrin, RGD Peptide and Dual-Targeted Nanoparticles Enhance Anti-VEGF Intraceptor Gene Delivery to Laser-Induced CNV. *Gene Ther.* **2009**, *16* (5), 645–659. https://doi.org/10.1038/gt.2008.185.

(26) Nakamura, H.; Jun, F.; Maeda, H. Development of Next-Generation Macromolecular Drugs Based on the EPR Effect: Challenges and Pitfalls. *Expert Opin. Drug Deliv.* **2015**, *12* (1), 53–64. https://doi.org/10.1517/17425247.2014.955011.

(27) Xu, Y.; Wu, H.; Huang, J.; Qian, W.; Martinson, D. E.; Ji, B.; Li, Y.; Wang, Y. A.; Yang, L.; Mao, H. Probing and Enhancing Ligand-Mediated Active Targeting of Tumors Using Sub-5 Nm Ultrafine Iron Oxide Nanoparticles. *Theranostics* **2020**, *10* (6), 2479–2494. https://doi.org/10.7150/thno.39560.

(28) Bogdanowich-Knipp, S. J.; Chakrabarti, S.; Siahaan, T. J.; Williams, T. D.; Dillman, R. K. Solution Stability of Linear vs. Cyclic RGD Peptides. *J. Pept. Res.* **1999**, *53* (5), 530–541. https://doi.org/10.1034/j.1399-3011.1999.00052.x.

(29) Stejskal, E. O.; Tanner, J. E. Spin Diffusion Measurements: Spin Echoes in the Presence of a Time-Dependent Field Gradient. *J. Chem. Phys.* **1965**, *42* (1), 288–292. https://doi.org/10.1063/1.1695690.

(30) Alvarado, E. Diffusion Experiments with Vnmrj 2.2C and 2.2D. *The University of Michigan Department of Chemistry*, **2010**.

(31) Pagès, G.; Gilard, V.; Martino, R.; Malet-Martino, M. Pulsed-Field Gradient Nuclear Magnetic Resonance Measurements (PFG NMR) for Diffusion Ordered Spectroscopy (DOSY) Mapping. *Analyst* **2017**, *142* (20), 3771–3796. https://doi.org/10.1039/C7AN01031A.

(32) Morris, K. F.; Johnson, C. S. Diffusion-Ordered Two-Dimensional Nuclear Magnetic Resonance Spectroscopy. *J. Am. Chem. Soc.* **1992**, *114* (8), 3139–3141. https://doi.org/10.1021/ja00034a071.

(33) Lu, Y.; Qian, L.; Zhang, Q.; Chen, B.; Gui, L.; Huang, D.; Chen, G.; Chen, L. Palmitate Induces Apoptosis in Mouse Aortic Endothelial Cells and Endothelial Dysfunction in Mice Fed High-Calorie and High-Cholesterol Diets. *Life Sci.* **2013**, *92* (24), 1165–1173. https://doi.org/10.1016/j.lfs.2013.05.002.

(34) Srinivasan, S.; Hatley, M. E.; Bolick, D. T.; Palmer, L. A.; Edelstein, D.; Brownlee, M.; Hedrick, C. C. Hyperglycaemia-Induced Superoxide Production Decreases ENOS Expression via AP-1 Activation in Aortic Endothelial Cells. *Diabetologia* **2004**, *47* (10), 1727–1734. https://doi.org/10.1007/s00125-004-1525-1.

(35) Fish, K. N. Total Internal Reflection Fluorescence (TIRF) Microscopy. *Curr. Protoc. Cytom. Editor. Board J Paul Robinson Manag. Ed. Al* **2009**, 50 (1), 12.18.1-12.18.13. https://doi.org/10.1002/0471142956.cy1218s50.

(36) Shah, R. S.; Soetikno, B. T.; Lajko, M.; Fawzi, A. A. A Mouse Model for Laser-Induced Choroidal Neovascularization. *J. Vis. Exp. JoVE* **2015**, No. 106. https://doi.org/10.3791/53502.

(37) Adhi, M.; Duker, J. S. Optical Coherence Tomography – Current and Future Applications. *Curr. Opin. Ophthalmol.* **2013**, *24* (3), 213–221. https://doi.org/10.1097/ICU.0b013e32835f8bf8.

(38) Hoshyar, N.; Gray, S.; Han, H.; Bao, G. The Effect of Nanoparticle Size on in Vivo Pharmacokinetics and Cellular Interaction. *Nanomed.* **2016**, *11* (6), 673–692. https://doi.org/10.2217/nnm.16.5.

(39) Kayano, D.; Kinuya, S. Current Consensus on I-131 MIBG Therapy. *Nucl. Med. Mol. Imaging* **2018**, *52* (4), 254–265. https://doi.org/10.1007/s13139-018-0523-z.

(40) Lavine, J. A.; Sang, Y.; Wang, S.; Ip, M. S.; Sheibani, N. Attenuation of Choroidal Neovascularization by B2-Adrenergic Receptor Antagonism. *JAMA Ophthalmol.* **2013**, *131* (3), 376–382. https://doi.org/10.1001/jamaophthalmol.2013.1476.

(41) Casini, G.; Dal Monte, M.; Fornaciari, I.; Filippi, L.; Bagnoli, P. The β-Adrenergic System as a Possible New Target for Pharmacologic Treatment of Neovascular Retinal Diseases. *Prog. Retin. Eye Res.* **2014**, *42*, 103–129. https://doi.org/10.1016/j.preteyeres.2014.06.001.

Chapter 5: Summary and Future Directions

5.1 Summary

This dissertation has evaluated new nanobiophotonic platforms for nanotherapy and nanoimaging applications, including polyacrylamide (PAAm)-encapsulated metal clusters, plasmonic nanosnakes, and RGD-targeted fluorescent 8-arm-peg NPs. Overall, synthesizing and characterizing new nanobiophotonic systems remains one of the most important active fields of research in the 21st century. At the present, nanoparticles have reached a threshold where biocompatible NPs with controllable size, morphologies, and functionality are becoming not only more widely fabricated and utilized, but also more highly specialized. Following this trend, each nanobiophotonic platform evaluated in this dissertation has rather specialized utility, with clear advantages as a new nanomaterial for specific applications in cancer therapy, plasmonic imaging, and disease targeting.

Chapter 2 of this dissertation examined polyacrylamide (PAAm)-encapsulated metal clusters for applications in two-photon photodynamic therapy. These PAAm-Au_{25} NPs show (1) highly enhanced cell biocompatibility and (2) greater cell uptake, compared to the non-embedded gold cluster. Furthermore, we demonstrate highly efficacious *in vitro* two-photon PDT for these PAAm-$Au_{25}Capt_{18}$ NPs, exhibiting a tremendous enhancement in 2p-PDT-mediated cell death over one-photon PDT-mediated cell death. This enhancement is associated with the high non-linear optical absorbance cross-section of the Au_{25} cluster. We show that as a new two-photon photodynamic agent, the $Au_{25}Capt_{18}$cluster, (a) has a two-photon cross-section 8x bigger compared to TMPYP, the most highly currently used two-photon photosensitizer, (b) has modest reactive oxygen species (ROS) production (1%) under two-photon

excitation, with the potential for this efficiency to be improved, and (c) when embedded in hydrogel NPs, its optical properties are maintained while achieving better biocompatibility and tumor uptake.

Chapter 3 of the dissertation examined highly linear plasmonic nanochains of gold nanospheres, which we call “nanosnakes”. These nanosnakes are self-assembled from bare Au nanosphere monomers, produced by laser ablation (green and chemical-free synthesis), where the monomers are surface conjugated with small, biocompatible molecules so as to induce their assembly. These nanosnakes have several highly desirable properties for biological imaging:

1.) Two plasmonic modes are present in each nanosnake sample, one fixed mode at 525 nm (monomer mode) and a second tunable mode. The secondary tunable mode varies from 590 nm to 640 nm, with tunability within 1-2 nm. Such tunability towards the infrared is a highly desirable property in plasmonic imaging due to these photons’ deeper tissue penetration as well as due to the much reduced background cell fluorescence.
2.) The nanosnakes possess scattering cross-sections up to 40x higher than Au nanosphere monomers (approximately 3x higher per chain monomer nanosphere), thus making them better contrast agents for imaging applications, since gold NPs are utilized for both dark-field and X-ray imaging.
3.) The nanosnakes can be easily conjugated with active targeting moieties for applications such as targeted cancer and heart disease phototherapy and they are also non-toxic to cells, even at very high concentrations, where concentrations as high as 0.25 mg/mL NP mass concentration (OD:5) were tested, thus adding to their biomedical promise.

To rigorously characterize these Au nanosnakes and demonstrate the biomedical potential of this new nanomaterial, several important experimental and theoretical studies were performed:

1.) Collecting thousands of TEM images for accurate statistical averaging of the nanosnake samples.
2.) Monte Carlo simulations to better understand the nanosnakes’ linear aggregation dynamics.

3.) Plasmonic computations (discrete dipole approximation, DDA) to reveal the nanosnakes' spectral properties (extinction, absorption, scattering, electric field) and to correlate the UV-Vis spectra directly with the TEM data.
4.) Biocompatibility (MTT) tests regarding the cell toxicity of the nanosnakes.
5.) Dark-field imaging experiments that show the *in vitro* imaging benefits of the Au nanosnakes, compared to Au monomer nanospheres.

Chapter 4 of the dissertation evaluated fluorescent 8-arm-peg NPs for their RGD-assisted targeting to the age-related macular degeneration (AMD) neovasculature. *In vitro* experiments revealed a strong, measurable difference between non-targeted and RGD targeted NPs, with the RGD targeted ones showing nearly a 100 % increase in NP uptake. Specifically, the 8-arm-peg-based RGD targeting exhibits a concentration dependence, with the highest incubated NP concentration (3 mg/mL) providing the greatest *in vitro* contrast. *In vivo* experiments at high incubated PEG-RGD concentrations (20 mg/mL injections) showed approximately 15-20% enhancement in targeting signal when compared to non-RGD controls. Overall, we show that 8-arm PEG NPs are a new, readily conjugatable and targetable nanosystem for future optimized AMD diagnosis and therapy, with potential benefits for *in vivo* theranostic enhancement.

5.2 Future Directions for PAAm-$Au_{25}Capt_{18}$ Embedded Clusters and 2-p Photodynamic Therapy

5.2.1 Enhancing the Reactive Oxygen Species (ROS) Production Efficiency of $Au_{25}(Capt)_{18}$ Clusters

As discussed in, "Synthesis and Optical Properties of Two-Photon Absorbing $Au_{25}(Captopril)_{18}$-Embedded Polyacrylamide Nanoparticles for Cancer Therapy" (Ch. 2), $Au_{25}Capt_{18}$ clusters have a high two-photon absorption cross-section (830 GM), but their reactive oxygen species production efficiency is low (approximately 1%), most probably due to the relatively short excited-state lifetime of the $Au_{25}Capt_{15}$ cluster.[1] Notably, Au_{25} clusters have excited state lifetimes from hundreds of nanoseconds to a few

microseconds, depending on the exact Au_{25} variant utilized.[2,3] Well-known photosensitizers like Rose Bengal (RB), Methylene Blue (MB), and the two-photon photosensitizer Meso-tetrakis(N-methyl-4-pyridyl)porphine tetrakis(p-toluenesulfonate) (TMPYP) have much longer excited state lifetimes (>100 μs),[4,5] and therefore have ROS production efficiencies of 75%, 50%, and 18.2%, respectively.[1]

To improve the excited state lifetime of the $Au_{25}(Captopril)_{18}$, synthetic approaches should be considered so as to modify the cluster. Several groups have shown that the ligands of the Au_{25} cluster influence the lifetime of its excited-state.[2,8] Stamplecoskie et. al. has even developed a charge-transfer system, utilizing an Au_{25} cluster variant, with quantum transfer efficiencies exceeding 10%.[2] It is imaginable that such a charge-transfer system could be used to pass the excited state photon to a long-lived excited state chromophore. Overall, ligand modification or adding a charge-acceptor moiety are both reasonable possibilities to lengthen the excited state lifetime of the cluster. To modify the $Au_{25}Capt_{18}$ cluster, we first must consider the chemical structure and morphology of $Au_{25}Capt_{18}$, as shown in Figure 5.1.

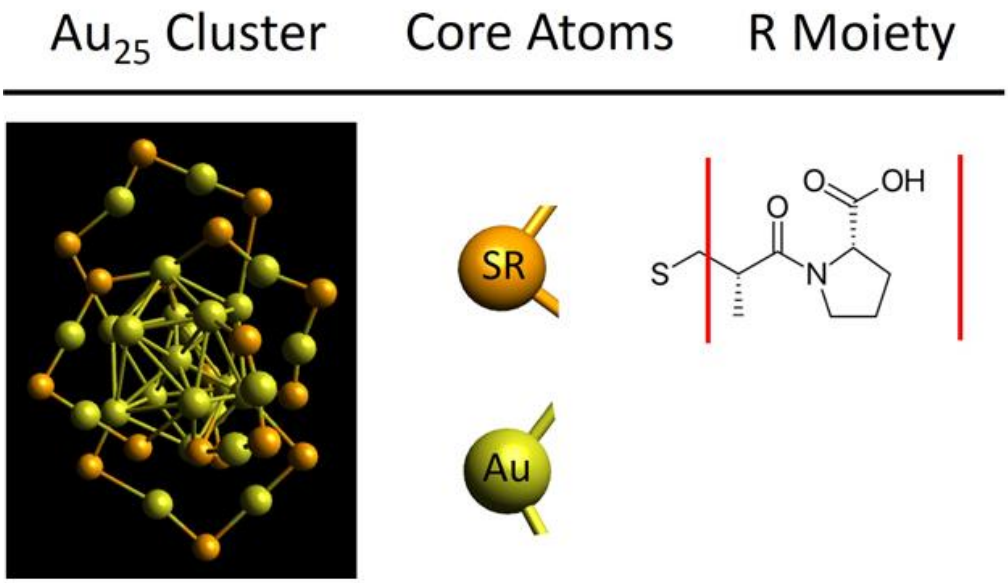

Figure 5.1 Structure of the $Au_{25}Capt_{18}$ cluster. The 'R' moiety (captopril ligand) has a carboxylic acid group which could be modified to improve the singlet oxygen efficiency of the cluster.

For Au clusters with terminal carboxylic acid groups, like that of the $Au_{25}Capt_{18}$ cluster, 1-Ethyl-3-(3-dimethylaminopropyl)carbodiimide (EDC) and NHS-derivatives can be used to activate the carboxylic acid for reactive chemistry.[9] Upon activation, the captopril ligands of the Au_{25} cluster would have an NHS-ester terminus for conjugation onto primary amines. Overall, ligand modification strategies following this activation paradigm should be considered for improving the Au_{25} ROS production efficiency.

It should be noted that Abbas et. al. propose an alternative way of modifying the optical properties and excited state lifetime of the Au_{25} cluster, namely via chemically doping the cluster with other metals.[8] While this suggestion is very reasonable for photovoltaic applications, for biological applications, and especially two-photon photodynamic therapy, chemical doping should be considered carefully. Foremost, while dopants like silver (Ag) and platinum (Pt) have been tested for Au_{25} clusters, only mercury (Mg) and cadmium (Cd)-doped clusters have been discovered to preserve the long excited-state lifetime of the Au_{25} cluster, yet both metals are notable for their extreme biotoxicity.[8,10] Additionally, iridium-doped Au clusters are a promising Au_{25} variant, yet their excited state lifetimes have not been investigated to date.[11] Secondly, as Abbas notes, the stability of doped clusters is significantly lower of pure clusters.[8] For two-photon photodynamic therapy, due to the intense power of the beam, stable clusters should be utilized whenever possible. Thirdly, while cadmium doping extends the $Au_{24}Cd$ excited state lifetime by 100% (100 ns to 200 ns),[10] this change in lifetime is not likely to raise the ROS production efficiency from 1% to >10%, but rather by more marginal increases. Still, improving the ROS production efficiency of Au_{25} by >10% could be a major goal for future research, so that gold nanoclusters can compete with other classes of photosensitizers. However, research into doped nanoclusters is one of the most active, and rapidly moving, fields of nanocluster research, and attention should be paid to new findings.

5.2.2 Extended Research into Two-Photon Reactive Oxygen Species (ROS) Sensing

In doing research on PAAm-encapsulated $Au_{25}Capt_{18}$ clusters, it has become obvious that analytically evaluating two-photon photodynamic therapy (2p-PDT)-based reactive oxygen production, and even two-photon absorption (especially for molecules with small quantum yields like the Au_{25} cluster), should be further developed. For example, anthracene-9,10-dipropionic acid (ADPA) and singlet oxygen sensing green (SOSG), both standard probes for measuring reactive oxygen species (ROS) production, do exhibit substantial fluorescent changes under TPA excitation (800 nm), even without the presence of a photosensitizer. This change in fluorescence in the absence of photosensitizer renders both ADPA and SOSG unusable probes for the direct measurement of the production of two-photon ROS species. In "Synthesis and Optical Properties of Two-Photon Absorbing $Au_{25}(Captopril)_{18}$-Embedded Polyacrylamide Nanoparticles for Cancer Therapy" (Ch. 2), to solve this problem, we instead measure the one-photon reactive oxygen species (ROS) production of $Au_{25}Capt_{18}$ and PAAm-$Au_{25}Capt_{18}$ encapsulated clusters (400 nm excitation).[1] It is well-known that excited state lifetimes, when compared between one-photon excitation and the equivalent energy of two-photon excitation, show little change, as the excited state transition is equivalent.[12] However, directly measuring two-photon reactive oxygen species (ROS) production would be more desirable than via an indirect one-photon measurement. Additionally, by directly measuring two-photon ROS efficacy, the power dependence of the ROS generation can be evaluated, which may also serve as a tool to determine the two-photon absorption cross-section if the ROS efficiency were known *a priori*.

For the reasons discussed above, research in the Kopelman laboratory has also extended to developing two-photon reactive oxygen species (ROS) sensing dyes. Namely, dichlorofluorescein (DCF) derivatives have been synthesized and are being evaluated for their ROS species production under one-photon and two-photon illumination. Additionally, we are working on encapsulating these DCF derivatives inside biocompatible nanoparticles for reliable ROS sensing *in vitro*, and potentially *in vivo*.

5.3 Future Directions for Highly Linear, Tunable, Strongly Scattering Plasmonic Nanosnakes

5.3.1 Synthesis and Characterization of Higher Linear, Spectrally Scattering Plasmonic Nanosnakes with Extended Longitudinal Surface Plasmon Resonances

Within "Gold Nanosnakes: Controlled Synthesis of Linear Nanochains with Tunable Plasmon Resonance for Nano-Biophotonics" (Ch.3), we successfully synthesized and characterized plasmonic nanosnakes with longitudinal surface plasmon resonances (LSPRs) up to 640 nm. While this plasmonic shift is large (>100 nm) when compared to the 20 nm Au monomers (520 nm), we are now able to fabricate highly tunable nanosnakes with LSPRs up to 750 nm. We note that the further the shift into the IR spectral range, the higher the biomedical benefits. We are working on characterizing these ultralong nanosnakes in a follow-up publication, with similar TEM analysis used to determine the mass lengths and branching ratios of each sample.

It should be noted that in such future work, studying longer nanosnakes opens new avenues for Monte Carlo simulations. Namely, for long nanoparticle chains, the fractal dimensions of the chains can be experimentally determined and compared to the Monte Carlo simulations. The Fractal Dimension is a measure of an object's topological dimension,[13] which would lie between 1 (1D) and 2 (2D) for the Au nanosnakes deposited on a TEM grid. By changing ligand ratios on the surface of the nanosnake, we predict that it may be possible to 'tune' the fractal dimension of the Au nanosnakes.

Also of importance is the diffusion coefficient used for the Monte Carlo simulations. The diffusion coefficient most closely relates to the assembly time (kinetics) of the cluster. In "Gold Nanosnakes: Controlled Synthesis of Linear Nanochains with Tunable Plasmon Resonance for Nano-Biophotonics" (Ch. 3), we assumed that the diffusion coefficient was proportional to 1/m, where m is the mass of the cluster. However, when measuring the experimental assembly time for each LSPR sample, we discovered that the diffusion coefficient of the nanosnakes is instead proportional to $1/m^2$. Running Monte Carlo simulations with varying diffusion coefficients has been shown not to substantially change particle morphology

(nanochain morphology in our case), but using the correct diffusion coefficient is necessary to correlate experimental assembly kinetics to theoretical (Monte Carlo) assembly kinetics.[14] Hence, we also plan to further explore Monte Carlo simulations with $1/m^2$ and $1/m^3$ like diffusion coefficients, and possibly fractional diffusion coefficients, to better understand the nanosnake assembly kinetics.

Lastly, unlike in "Gold Nanosnakes: Controlled Synthesis of Linear Nanochains with Tunable Plasmon Resonance for Nano-Biophotonics" (Ch.3), discrete dipole approximations (DDA) computations for longer plasmonic nanosnakes are substantially more difficult. Foremost, with longer nanosnakes, longer chains will need to be computed to correlate TEM distributions to extinction spectra. Running longer samples (therefore containing higher number of point dipoles) increases computational time by a factor of 6-8 as the radius doubles. However, of more concern, the 1 dipole-per-nanometer (dpnm) simulations reach an asymptote at 650-660 nm LSPR with increasing numbers of monomers. In most plasmonic studies, using 1 dpnm to build plasmonic morphologies is more than sufficient for simulation accuracy.[15] However, as the chain length grows longer, the electron density between the monomer gaps becomes more sensitive to dpnm increases. For example, running a 30-mer with 2 dpnm density yields a LSPR maximum of 750-800 nm, whereas the 1 dpnm density has an LSPR near the 650 nm asymptote. Hence, to solve this problem, higher dipole-per-nanometer densities need to be run for long nanosnake samples. However, 2 dpnm simulations are very costly and time prohibitive – a single 30-mer computation could take > 1 week utilizing 30 cores. To solve this problem, adopting an approach similar to Tserkezis et. al., in running simulations with higher dipole counts along boundary regions (i.e. gap interface), should be considered.[16] This may solve the dpnm issue caused by the nanosnake gaps, and allow the simulations to be more cost-effective.

5.4 Future Directions for Fluorescent 8-arm-peg NPs for the Treatment of Macular Degeneration

5.4.1 Synthesis of Thiolated Iogenguane (MIBG) Derivatives for Targeted Macular Degeneration Imaging

In "Development of Targeted 8-arm PEG Nanosystems for Choroidal Neovascular Macular Degeneration Diagnosis and Therapy" (Ch. 4), we studied RGD-targeted 8-arm-peg nanosystems for

imaging of the macular degeneration vasculature. Overall, the *in vitro* RGD-targeting NP uptake showed approximately 100% (3 mg/mL incubation) uptake when compared to non-RGD NP controls, and *in vivo* targeting showed 15-20% increased uptake. Previous studies have indicated that RGD works better when combined with other targeting agents ('dual targeting') for nanoparticle-assisted AMD localization.[17] To improve the targeting efficiency, we are synthesizing a secondary moiety that can work in tandem with RGD, a thiolated iobenguane ('MIBG') derivative. MIBG binds to the norepinephrine transporter (NET) in cells that have adrenergic activity.[18] While retinal cells typically do not have high levels of adrenergic receptors, upregulation of the β-adrenergic pathway has been associated with CNV disorders.[19,20]

Designed by the Kopelman group in collaboration with the laboratory of Dr. John Wolfe, the thiolated MIBG-derivative ('dMIBG') involves a 6-step synthesis. Following our protocol, the synthetic yield of the derived MIBG moiety is 100 mg – 200 mg, and the cost is at least 5x lower then the price of an equivalent molarity of the RGD peptide. Conjugated dMIBG-8-arm-PEG NPs have been successfully synthesized, with the dMIBG attachment confirmed via NMR spectroscopy. We are currently performing *in vitro* studies on the MIBG-PEG NP uptake, with plans to test MIBG-RGD-PEG NP uptakes in future experiments. Finally, *in vivo* experiments will proceed when the optimal *in vitro* ratios of MIBG and RGD peptide are determined, with 'mono targeted' MIBG and RGD PEG NPs used as controls, in addition to non-targeted controls.

5.5 References

(1) McLean, A.; Wang, R.; Huo, Y.; Cooke, A.; Hopkins, T.; Potter, N.; Li, Q.; Isaac, J.; Haidar, J.; Jin, R.; Kopemlan, R. Synthesis and Optical Properties of Two-Photon-Absorbing Au25(Captopril)18-Embedded Polyacrylamide Nanoparticles for Cancer Therapy. *ACS Appl. Nano Mater.* **2020**, *3* (2), 1420–1430. https://doi.org/10.1021/acsanm.9b02272.

(2) Stamplecoskie, K. G.; Chen, Y. S.; Kamat, P. V. Excited-State Behavior of Luminescent Glutathione-Protected Gold Clusters. *J. Phys. Chem. C* **2014**, *118* (2), 1370–1376. https://doi.org/10.1021/jp410856h.

(3) Wen, X.; Yu, P.; Toh, Y. R.; Hsu, A. C.; Lee, Y. C.; Tang, J. Fluorescence Dynamics in BSA-Protected Au 25 Nanoclusters. *J. Phys. Chem. C* **2012**, *116* (35), 19032–19038. https://doi.org/10.1021/jp305902w.

(4) Stiel, H.; Teuchner, K.; Paul, A.; Leupold, D.; Kochevar, I. E. Quantitative Comparison of Excited State Properties and Intensity-Dependent Photosensitization by Rose Bengal. *J. Photochem. Photobiol. B Biol.* **1996**, *33* (3), 245–254. https://doi.org/10.1016/1011-1344(95)07248-9.

(5) Gonalves, P. J.; Franzen, P. L.; Correa, D. S.; Almeida, L. M.; Takara, M.; Ito, A. S.; Zílio, S. C.; Borissevitch, I. E. Effects of Environment on the Photophysical Characteristics of Mesotetrakis Methylpyridiniumyl Porphyrin (TMPyP). *Spectrochim. Acta - Part A Mol. Biomol. Spectrosc.* **2011**, *79* (5), 1532–1539. https://doi.org/10.1016/j.saa.2011.05.012.

(6) Gottfried, V.; Peled, D.; Winkelman, J. W.; Kimel, S. Photosensitizers in Organized Media: Singlet Oxygen Production and Spectral Properties. *Photochem. Photobiol.* **1988**, *48* (2), 157–163. https://doi.org/10.1111/j.1751-1097.1988.tb02801.x.

(7) Redmond, R. W.; Gamlin, J. N. A Compilation of Singlet Oxygen Yields from Biologically Relevant Molecules. *Photochem. Photobiol.* **1999**, *70* (4), 391–475. https://doi.org/10.1111/j.1751-1097.1999.tb08240.x.

(8) Abbas, M. A.; Kamat, P. V.; Bang, J. H. Thiolated Gold Nanoclusters for Light Energy Conversion. *ACS Energy Lett.* **2018**, *3* (4), 840–854. https://doi.org/10.1021/acsenergylett.8b00070.

(9) Vankayala, R.; Kuo, C. L.; Nuthalapati, K.; Chiang, C. S.; Hwang, K. C. Nucleus-Targeting Gold Nanoclusters for Simultaneous in Vivo Fluorescence Imaging, Gene Delivery, and NIR-Light Activated Photodynamic Therapy. *Adv. Funct. Mater.* **2015**, *25* (37), 5934–5945.

https://doi.org/10.1002/adfm.201502650.

(10) Zhou, M.; Yao, C.; Sfeir, M. Y.; Higaki, T.; Wu, Z.; Jin, R. Excited-State Behaviors of M1Au24(SR)18 Nanoclusters: The Number of Valence Electrons Matters. *J. Phys. Chem. C* **2018**, *122* (25), 13435–13442. https://doi.org/10.1021/acs.jpcc.7b11057.

(11) Bhat, S.; Baksi, A.; Mudedla, S. K.; Natarajan, G.; Subramanian, V.; Pradeep, T. Au22Ir3(PET)18: An Unusual Alloy Cluster through Intercluster Reaction. *J. Phys. Chem. Lett.* **2017**, *8* (13), 2787–2793. https://doi.org/10.1021/acs.jpclett.7b01052.

(12) Lakowicz, J. R. *Principles of Fluorescence Spectroscopy*; **2011**.

(13) Barnsley, M. *Fractals Everywhere*; **2014**.

(14) Meakin, P. Diffusion-Controlled Aggregation on Two-Dimensional Square Lattices: Results from a New Cluster-Cluster Aggregation Model. *Phys. Rev. B* **1984**, *29* (6), 2930–2942. https://doi.org/10.1103/PhysRevB.29.2930.

(15) Kealley, C. S.; Cortie, M. B. A Computational Exploration of the Color Gamut of Nanoscale Hollow Scalene Ellipsoids of Ag and Au. *Plasmonics* **2010**, *5* (1), 37–43. https://doi.org/10.1007/s11468-009-9112-4.

(16) Tserkezis, C.; Herrmann, L. O.; Valev, V. K.; Baumberg, J. J.; Aizpurua, J. Optical Response of Threaded Chain Plasmons: From Capacitive Chains to Continuous Nanorods. *Opt. Express* **2014**, *22* (20), 23851. https://doi.org/10.1364/oe.22.023851.

(17) Singh, S. R.; Grossniklaus, H. E.; Kang, S. J.; Edelhauser, H. F.; Ambati, B. K.; Kompella, U. B. Intravenous Transferrin, RGD Peptide and Dual-Targeted Nanoparticles Enhance Anti-VEGF Intraceptor Gene Delivery to Laser-Induced CNV. *Gene Ther.* **2009**, *16* (5), 645–659. https://doi.org/10.1038/gt.2008.185.

(18) Streby, K. A.; Shah, N.; Ranalli, M. A.; Kunkler, A.; Cripe, T. P. Nothing but NET: A Review of Norepinephrine Transporter Expression and Efficacy of 131I-MIBG Therapy. *Pediatric Blood and*

Cancer. **2015**, 62 (1), 5–11. https://doi.org/10.1002/pbc.25200.

(19) Casini, G.; Dal Monte, M.; Fornaciari, I.; Filippi, L.; Bagnoli, P. The β-Adrenergic System as a Possible New Target for Pharmacologic Treatment of Neovascular Retinal Diseases. *Prog. Retin. Eye Res.* **2014**, *42*, 103–129. https://doi.org/10.1016/j.preteyeres.2014.06.001.

(20) Lavine, J.; Sang, Y.; Wang, S.; Ip, M; Sheibani, N. Attenuation of Choroidal Neovascularization by B2-Adrenoreceptor Antagonism. *JAMA opthalmology.* **2013***,* 131 (3), 376-382.